CARL VON OSSIETZKY universität OLDENBURG

Preparation and Characterization of Cuprous Oxide Thin Films using Low-Temperature Scanning Tunneling Microscopy

Von der Fakultät für Mathematik und Naturwissenschaften
der Carl von Ossietzky Universität Oldenburg
zur Erlangung des Grades und Titels eines
Doktors der Naturwissenschaften
(Dr. rer. nat.)
angenommene Dissertation

von

Hanna Fedderwitz
geboren am 23.12.1983 in Hannover

Gutachter:	Prof. Dr. Niklas Nilius
Zweitgutachter:	apl. Prof. Dr. Achim Kittel
Mitglied der Prüfungskommission:	Prof. Dr. Alexander Hartmann
Tag der Disputation:	22.12.2016

List of Publications

- H. Sträter, H. Fedderwitz, B. Groß and N. Nilius. **Growth and surface properties of cuprous oxide films on Au(111)**. *J. Phys. Chem. C*, 119, 5975–5981, (2015).
- N. Nilius, H. Fedderwitz, B. Groß, C. Noguera and J. Goniakowski. **Incorrect DFT-GGA predictions of the stability of non-stoichiometric / polar dielectric surfaces: the case of Cu_2O(111)**. *Phys. Chem. Chem. Phys.*, 18, 6729–6733, (2016).
- H. Fedderwitz, B. Groß, H. Sträter and N. Nilius. **Reactive copper deposition on Au(111) and Mo(001): Role of the support in the oxidation process**. *J. Phys. Chem. C*, 120, 7591–7596, (2016).

Abstract

Serving the rising demand for electric energy is one of the key challenges of the 21st century. As fossile fuels are limited, renewable energies are in constant developement. Solar cells, devices that turn light into electric energy, have developed from thick, heavy, brittle constructions into thin, light-weight, flexible materials easily integrated into buildings, cars or electronic devices. This is due to the development of thin-film absorbers which can be fabricated on flexible substrates.
Unfortunately most materials used in thin-film solar cells are either very rare (and therefore expensive), difficult to process and handle, toxic, environmentally unfriendly or a combination thereof. A material suitable for photovoltaic applications but also earth abundant, non-toxic and easy to process as a thin film is cuprous oxide (Cu_2O).

Cu_2O solar cells have been investigated since the 1970's but with little success as the conversion efficiencies reached approximately 2% staying well below the theoretical maximum of 20% for a single junction Cu_2O solar cell. The culprit has been identified as a reaction of the Cu_2O layer with an adjacent metal or semiconductor layer [1]. One of the presently best cuprous oxide solar cell has 5.38% efficiency [2] using a Ga_2O_3 n-type layer and an Al-doped ZnO layer as window electrode. According to Minami and co-workers the improved performance was due to a decrease of defect concentration at the Ga_2O_3/Cu_2O interface rather than by a different working principle of the thin film. This shows that a detailed understanding of the structure as well as the electrical and chemical properties of the Cu_2O film is paramount to improve the performance of thin film Cu_2O solar cells. Thin films differ from bulk materials in that their properties depend greatly on electron confinement and interface effects. In the case of copper oxide, the band gap, which determines the maximum theoretical absorption in a solar cell, can be tuned by changing the oxidation level from Cu_2O to CuO.

In this Thesis Cu_2O thin films of up to 5nm thickness were prepared by evaporating copper in an oxygen atmosphere of 10^{-6} mbar. Gold and Molybdenum were used as chemically inert and reactive substrates respectively. The samples were analysed in a Scanning Tunneling Microscope (STM) showing the structure of the $Cu_2O(111)$ surface at an atomic level. Scanning Tunneling Spectroscopy (STS) has been used to explore the electronic structure. The findings have been compared to calculations from Density Functional Theory (DFT) rationalizing the electronic and stoichiometric results found with STM and STS. Additionally X-ray Photoelectron Spectroscopy was used to determine the chemical composition of the films.

For $Cu_2O(111)/Au(111)$ flat and homogeneous films have been obtained. A variety of surface structures were found. The most common one, being obtained after annealing

the films at 650 K or higher is the so-called hexagonal phase which resembles the bulk $Cu_2O(111)$ termination. It is characterized by a hexagonal atomic pattern with 6Å periodicity. The band gap measured with STS is slightly smaller than that of bulk Cu_2O at 2.1 eV. The presence of a surface states in the band gap, close to the conduction band makes the determination of the exact gap size difficult.
Comparing ST-spectra and topographic images to improved DFT calculations revealed that the observed contrast in STM as well as the surface states belong to unsaturated copper ions only present in the stoichiometric $Cu_2O(111)$ surface. The previously suggested Cu-deficient termination [3–5] could thus not be confirmed for films of a few mono-layers thickness. Frequently observed protrusions at fixed lattice positions represent building blocks for the following Cu_2O layer, indicating a layer by layer growth of cuprous oxide on the Au(111) support. This opens up the possibility of a controlled layer-by-layer growth with further research.
Under varying preparation conditions a number of different surface structures were observed. They all show the band gap of cuprous oxide ($\leq$ 2 eV) but not all of them showed the surface states observed for the hexagonal phase. Wherever possible surface structures were compared to DFT calculations and clarified by structural models.
When the same reactive copper deposition was repeated on a Mo(001) substrate well ordered nano-particles emerged instead of the flat films observed on the gold substrate. XP-spectra showed that the Mo support instead of the copper was oxidized. In this case the decrease in surface energy from Mo(001) to MoO_x was found to be responsible for Cu particle growth according to the Wulff-Theorem.

This work provides atomic scale insight into the nature of Cu_2O surfaces, which have not been presented in other works so far. By deepening the understanding of the structural, electronical and chemical properties of cuprous oxide thin films, as well as the role of growth conditions and choice of substrate this work helps to develop copper oxides based devices and technologies such as photovoltaics. For the prepared films a stoichiometric termination was found and confirmed by improved DFT calculations in contrast to earlier studies suggesting a Cu-deficient surface. As the observed stoichiometric $Cu_2O(111)$ grows in a layer-by-layer fashion, tuning of the film thickness is feasible. The observed Cu ad-particles as well as Cu vacancies are a good starting point to explore the mechanism of film growth and defect structures (responsible for p-type conductivity) in the future. Also research on thicker Cu_2O films would be beneficial to close the gap to bulk properties.
Additionally, the well-ordered and uniform Cu nano-particles found on the molybdenum support can probably be used in nano-catalysis or optics. For this, research on how to tune the density, size and shape (hence surface termination) of the particles as well as the chemical reactivity and optical properties will be required in the future.

Zusammenfassung

Der wachsenden Nachfrage nach elektrischer Energie nachzukommen, ist eine der größten Herausforderungen des 21. Jahrhunderts. Da fossile Brennstoffe begrenzt sind, rücken erneuerbare Energien in den Mittelpunkt. Solarzellen, Geräte, die Sonnenlicht in elektrische Energie umwandeln, entwickeln sich von dicken, schweren und empfindlichen Konstruktionen zu dünnen, leichten und flexiblen Materialien, die leicht in Gebäude, Fahrzeuge oder elektronische Geräte integriert werden können. Dies ist nur möglich durch die Entwicklung von Dünnschichtabsorbern, die auf flexiblen Substraten aufgebracht werden können.
Unglücklicherweise sind die meisten Materialien, die für Dünnschichtsolarzellen genutzt werden können, sehr selten (und dadurch teuer), schwierig zu handhaben, giftig, umweltgefährdend oder eine Kombination daraus. Ein Material, dass für photovoltaische Anwendungen genutzt werden kann und gleichzeitig reichlich vorhanden, ungiftig und einfach zu verarbeiten ist, ist Kupfer(I)oxid (Cu_2O).

Cu_2O Solarzellen werden bereits seit den 1970er Jahren erforscht, allerdings mit wenig Erfolg, da die Wirkungsgrade nur ungefähr 2% erreichten und damit weit unter dem theoretischen Maximum von 20% für eine Solarzelle mit nur einem Halbleiterübergang zurückblieben. Die Ursache des schlechten Wirkungsgrades wurde in einer Reaktion der Cu_2O-Lage mit angrenzenden Metall- oder Halbleiterschichten gefunden [1]. Eine der zur Zeit besten Kupferoxid-Solarzellen zeigt einen Wirkungsgrad von 5.38% [2], der durch die Nutzung einer n-dotierten Ga_2O_3-Lage und einer Al-dotierten ZnO-Schicht als Fensterschicht erreicht wurde. Minami und Mitarbeitern zufolge wurde die verbesserte Leistung der Solarzelle durch eine verringerte Defektdichte an der Ga_2O_3/Cu_2O Grenzfläche, nicht durch ein anderes Funktionsprinzip der Schicht erreicht.
Dies zeigt, das ein detailliertes Verständniss der Struktur, sowie der elektronischen und chemischen Eigenschaften der Cu_2O Schicht überragend ist, um die Leistung Cu_2O basierter Solarzellen zu erhöhen. Dünschichtmaterialien unterschieden sich von Volumenmaterialien dadurch, dass ihre Eigenschaften stark von begrenzten Elektronenzuständen und Effekten an den Grenzflächen abhängen. Im Fall von Kupferoxid kann die Größe der Bandlücke, welche das theoretische Maximum der Absorption in einer Solarzelle bestimmt, durch einen Wechsel des Oxidationsniveaus von Cu_2O zu CuO eingestellt werden.

In dieser Arbeit wurden Cu_2O Dünnschichten mit einer Dicke von bis zu 5nm durch das Verdampfen von Kupfer in einer 10^{-6} mbar Sauerstoffatmosphere hergestellt. Gold und Molybdän wurden als chemisch inertes und reaktives Substrat benutzt. Die Proben wurden mit Hilfe eines Rastertunnelmikroskops (engl. Scanning Tunneling Microscope - STM), welches die Struktur der $Cu_2O(111)$ Oberfläche mit atomarer Auflösung zeigt,

analysiert. Tunnelspektroskopie (engl. Scanning Tunneling Spectroscopy - STS) wurde genutzt, um die elektronische Struktur zu untersuchen. Die Resultate wurden mit Rechnungen der Dichtefunktionaltheorie (engl. Density Functional Theory - DFT) verglichen um die elektronischen und stoichiometrischen Resultate zu erklären. Zusätzlich wurde Röntgensprektroskopie (engl. X-ray Photoelectron Spectroscopy - XPS) genutzt, um die chemische Zusammensetzung der Schicht zu bestimmen.

Im Fall von $Cu_2O(111)/Au(111)$ wurden flache und homogene Schichten gefunden. Mehrere unterschiedliche Oberflächenstrukturen wurden dabei beobachtet. Die am häufigsten vertretene, welche nach Ausheizen der Probe bei 650K oder mehr beobachtet wurde, ist die sogenannte hexagonale Phase, die der Volumentermination von $Cu_2O(111)$ ähnelt. Die hexagonale Phase zeichnet sich durch ein hexagonales atomares Muster mit einer Periodizität von 6Å aus. Die mit STS gemessene Bandlücke ist etwas kleiner als die von Volumen-Cu_2O, welche 2.1eV beträgt. Ein in der Bandlücke gefundener Oberflächenzustand in der Nähe des Leitungsbandes, erschwert die genaue Bestimmung der Bandlücke.
Ein Vergleich von ST-Spektren und topografischen Bildern mit verbesserten DFT Berechnungen zeigte, dass sowohl der beobachtbare Kontrast im STM als auch der Oberflächenzustand durch nicht abgesättigte Bindungen der Kupferionen entstehen, welche nur in der stoichiometrischen $Cu_2O(111)$-Oberfläche auftreten. Die vormals vorgeschlagene, kupferarme Oberfläche [3–5] konnte somit für Schichtdicken von einigen Monolagen nicht bestätigt werden. Wiederholt beobachtete Erhebungen an festen Gitterplätzen stellen die ersten Bausteine der folgenden Cu_2O-Lage dar, welches ein Lagenwachstum des Kupferoxids auf Au(111) anzeigt. Dies eröffnet die Möglichkeit eines kontrollierten Lagenwachstums durch weitere Forschungstätigkeit.
Unter verschiedenen Preparationsbedingungen wurden eine Vielzahl verschiedener Oberflächenstrukturen beobachtet. Alle zeigten dabei die Bandlücke von Kupferoxid ($\leq 2\,\mathrm{eV}$), doch nicht alle zeigten den für die hexagonale Phase beobachteten Oberflächenzustand. Soweit wie möglich wurden die Oberflächenstrukturen mit DFT Berechnungen verglichen und durch Strukturmodelle verdeutlicht.
Eine Wiederholung der selben, reaktiven Kupferverdampfung auf einen Mo(001) Kristall führte zu wohlgeordneten Nanopartikeln an Stelle der flachen Schichten, die auf Gold beobachtet wurden. Die Absenkung der Oberflächenenergie von Mo(001) zu MoO_x ist hier gemäß des Wulff-Theorems verantwortlich für das Partikelwachstum.

Diese Arbeit liefert Einsichten in die Natur der Cu_2O Oberflächen auf atomarer Ebene, die bisher nicht in anderen Arbeiten präsentiert wurden. Durch das tiefere Verständniss der strukturellen, elektronischen und chemischen Eigenschaften von Kupferoxiddünnschichten, sowie die Rolle der Wachstumsbedingungen und der Wahl des Substrats trägt diese Arbeit dazu bei, kupferoxidbasierte Technologien wie z.B. Photovoltaik zu

verbessern. Für die hergestellten Schichten wurde eine stoichiometrische Oberfläche gefunden und mit Hilfe von verbesserten DFT Berechungen bestätigt, im Gegensatz zu früheren Arbeiten, die eine kupferarme Oberfläche vorschlugen. Da das beobachtete stoichiometrische Cu_2O lagenweise wächst, ist eine gezielte Schichtdicke denkbar. Die beobachteten Kupferadpartikel genauso wie die Kupferdefektstellen sind ein guter Ausgangspunkt für weitere Arbeiten, um das Schichtwachstum sowie die Defektstrukturen (welche für die p-Leitung verantwortlich sind) in Zukunft weiter zu erforschen. Ebenfalls wären Untersuchungen an dickeren Cu_2O Schichten nützlich, um den Übergang zu Volumeneigenschaften herzustellen.

Zusätzlich könnten die gut geordneten und einheitlichen Nanopartikel, die auf dem Molybdänsubstrat gefunden wurden, in der Nanokatalyse oder der Optik zum Einsatz kommen. Um dies zu erreichen, wären weitere Untersuchungen zur Kontrolle von Dichte, Größe und Form (folglich also Oberfläche) der Partikel sowie deren chemischen und optischen Eigenschaften nötig.

Table of Contents

List of Publications iii

Abstract vii

Zusammenfassung ix

Table of Contents xi

List of Figures xvii

List of Tables xxv

Abbreviations xxvii

I Introduction and Setup 1

1 Introduction 3

2 Thin Film Solar Cells 7
- 2.1 Introduction . . . 7
- 2.2 Theory . . . 8
  - 2.2.1 Junction . . . 9
  - 2.2.2 Energy Conversion Efficiency . . . 10
- 2.3 Design of a Solar Cell . . . 12
  - 2.3.1 Absorber . . . 13
- 2.4 Cu_2O in Photovoltaic Devices . . . 15

3 Experimental Techniques 17
- 3.1 Scanning Tunneling Microscopy . . . 17
  - 3.1.1 Introduction . . . 17
  - 3.1.2 STM Setup . . . 18
  - 3.1.3 Calculating the Tunnel Current . . . 19
  - 3.1.4 STM on thin insulating films . . . 21
  - 3.1.5 Scanning Tunneling Spectroscopy . . . 22
  - 3.1.6 Surface States . . . 26

3.2 X-Ray Photoelectron Spectroscopy 28
3.2.1 Introduction 28
3.2.2 Theory 31
3.2.3 Applications 37
3.3 Low Energy Electron Diffraction 40
3.3.1 Introduction 40
3.3.2 Theory 41
3.4 Gibbs-Curie-Wulff Theorem 42

4 Experimental setup **45**
4.1 The Preparation and XPS Chambers 45
4.2 The STM Chamber 47
4.3 The High Pressure Chamber 48

II Scientific Results **51**

5 Introduction to Cu_2O **53**
5.1 Structural Properties 53
5.2 Electronic Properties 55
5.3 P-type Conductivity 58
5.4 The Cu_2O Surface 60

6 Preparation of Cu_2O Thin Films **67**
6.1 Temperature of the Heating Stage 68
6.2 XPS Energy Reference 69
6.3 Copper Evaporation Rate 70
6.4 Thin Film Annealing 72

7 XP Spectroscopy of Cu_2O **75**
7.1 Copper and Oxygen XP-Spectra 76
7.2 Changes of the support during reactive Cu deposition 83

8 Cu_2O-films on Au(111) **85**
8.1 Gold substrate 85
8.2 Structure and Morphology of the Cu_2O adlayer 87
8.2.1 As-Grown Films 87
8.2.2 Post-Annealed Films 89
8.3 Hexagonal Phase 92
8.3.1 Theoretical Stability Calculations 92
8.3.2 Electronic Properties 96
8.3.3 Structure Models 98
8.4 Stripe Phase along Au[110] 100
8.5 Stripe Phase along Au[112] and Donut phase 103
8.6 Smooth Areas and Herringbone Areas 106
8.7 Phase Diagram 108
8.8 Ad-Particles 111

9 Cu_2O-films on Mo(001) - Role of the support **115**
9.1 Introduction 115
9.2 Structure and Morphology 116
9.3 Comparison of Cu+O deposition onto Au and Mo support 118

III Summary and Outlook **123**

10 Summary **125**

11 Outlook **127**

Bibliography **130**

Acknowledgements **147**

Curriculum Vitae **149**

Erklärung gemäß Promotionsordnung **151**

List of Figures

2.1 I-V-curve of an illuminated solar cell. Maximum power point and fill factor are indicated. [36] 8
2.2 Left: Space charge area in a p-n-junction, according charge distribution, electric field and voltage gradients. right: Band bending in different junctions. [38–40] 10
2.3 Maximum conversion efficiency for a single junction solar cell depending on the band gap of the semi-conducting absorber material. [45] 12
2.4 Possible composition of a hetero-junction solar cell using CIGS as absorber and ZnO as transparent conducting oxide. [9] 13

3.1 STM Setup with atomically sharp metal tip, sample and feedback loop. [60] 18
3.2 Sketch of a tunneling process through a one-dimensional barrier. The tunnel current depends exponentially on the tip sample distance. [64] . . 19
3.3 Tip trajectory with an s-orbital (left) and a p-orbital (right). Because of the directed shape of the p orbital the atomic corrugation of the sample is imaged at a higher resolution. 21
3.4 Schematic view of a tunnel junction consisting of the vacuum gap and the oxide layer on top of the metal substrate. The bias voltage is not large enough for electrons to reach the conduction band. CB and VB are bend due to the electric field across the tunnel junction. [64] 22
3.5 Tip DOS (left) and Sample DOS (right). Because of the applied bias voltage E_F (Sample) is offset with respect to E_F (Tip) electrons above E_F (Tip) are tunneling from occupied states in the sample into unoccupied states in the tip. The tunnel current depends on the number of available states in the tip and the sample. [74] 23
3.6 Topographic image and conductance map of an Au island on 25 ML CaO(001) [75] 24
3.7 Field Emission Resonances caused by reflected electrons between tip and sample. [74] 25
3.8 Inelastic tunneling electrons give a small contribution to the overall tunneling current. d^2I/dV^2 shows the Energy of the inelastic process. [74] . . 26
3.9 Periodic potential created by atomic cores with a step function at the surface. The dashed line is a more realistic form of the potential than the step function. [84] 27
3.10 Electronic states are Bloch waves within the crystal that exponentially decay into the vacuum at the surface. [84] 27
3.11 Bragg reflection at the brillouin zone boundary ($\pm\pi/2$) creates a band gap. [84] 28

3.12 Electronic states with energies inside the band gap can exist at the surface but decay exponentially into the bulk and the vacuum. [84] 28
3.13 XPS Setup: An X-ray beam hits the target thereby emitting electrons which are collected by electrostatic lenses. The analyser only admits electrons of a certain energy range to the detector. [91] 29
3.14 XPS survey spectrum of a gold sample showing the binding energy on the abscissa. Typical peaks are seen at ≈90 eV (Au 4f), ≈350 eV (Au 4d) and ≈550 eV (Au 4p). [92] 29
3.15 Electron escape depth for different elements depending on universal electron mean free path. [94] 30
3.16 Mo 3d XP-spectrum showing a doublet structure (3/2 and 5/2) due to spin-orbit-splitting as well as chemical shift for different oxidation states between Mo^0 at 228 eV + 231 eV and MoO_3 at 233 eV + 235 eV. [95] . . . 30
3.17 Schematic view of the basic photoelectric effect used in XPS and respective quantum numbers, electron levels, Auger and XPS notation. [104] 31
3.18 Difference in measured kinetic energy E_{kin} and initial kinetic energy E^1_{kin} due to the spectrometer work function Φ_{spec}. [91] 33
3.19 Photoelectric cross section at an incident radiation of 1.5keV for various elements and electronic sub-shells [91]. 34
3.20 Shake-up peak in CuO on the high binding energy side of Cu 2p 3/2. No shake-up peaks occur in Cu_2O. [97] 35
3.21 Different Backgrounds as compared by Repoux 35
3.22 Coster-Kronig process (left) followed by Auger process (right). In the Coster-Kronig process an electron from the L_3 shell fills the hole left by the primary electron. With the freed energy an electron from $M_{4,5}$ shell is ejected. There are now two holes in the electron configuration. In a subsequent Auger Process the L_3 hole is filled by an electron from the $M_{4,5}$ shell simultaneously emitting another electron from the $M_{4,5}$ shell, leaving the atom with three holes in the valence band. [112] 36
3.23 Gaussian (G), Lorentzian (L) and two Doniach-Sunjic (D-S) line shapes with different asymmetry factors α_{DS}. [93] 38
3.24 Wagner plot for the zinc compounds showing the $L_3M_{4,5}M_{4,5}$ kinetic energy versus the 2p 2/3 binding energy. Different chemical configurations are easily distinguished. [99] 38
3.25 Angle resolved XPS showing the change in relative intensities of thin film and substrate with changing emission angle. [117] 39
3.26 With longer deposition times, the films thickness grows and XP intensities increase. At the completion of 1 ML the 2nd layer starts to attenuate the signal from the first, resulting in a slower rise in XP intensities. [100] . . . 40
3.27 Sub mono-layer films show binding energies different than the bulk values due to the relatively higher interface and surface contributions. With increasing film thickness the surface and interface contributions get attenuated and the binding energy shifts towards the bulk value. [100] . . . 40
3.28 Schematic LEED Setup. The Diffraction pattern on the fluorescent screen can be seen through the view port. [120] 41
3.29 LEED pattern of a Si(100) reconstructed surface. [120] 41

3.30 Left: Ewald-sphere with incident wave vector k_i and diffracted wave vector k_f [123]. Centre and right: Atomic surface structures in real space and resulting LEED pattern in reziprocal space. [120] 42
3.31 Shape of an unsupported particle derived from surface free energy (Wulff construction) left [125], right [126] 43
3.32 Shapes of supported particles [126] 44

4.1 Pictures of the UHV-Setup. 1: STM chamber, 2: bath cryostat, 3: preparation chamber, 4: high pressure chamber, 5: XPS chamber 46
4.2 Left: Photo of the STM scan head hanging on springs and damped by an Eddy Current Unit. Right: Drawing of the scan head setup[74]. A: ramp with different sectors, B: sample, C: support ball, D. sapphire, E: support-piezo, F: tip, G: tip-holder, H: scan-piezo, I: base [64] 48
4.3 Setup of the new high pressure chamber. The back of the sample holder is attached to a linear transfer rod. Underneath the circular plate that holds the sample the aluminium heating block is attached. 49

5.1 Unit cell and Brioullin zone of Cu_2O. [52] 53
5.2 Specific resistance and hole carrier concentration in Cu_2O depending on oxygen flow during preparation [52] 55
5.3 Band structure of Cu_2O with a direct band gap at Γ and the resulting DOS as calculated in hybrid functional DFT. The calculated values for the indirect band gap are 0.7 (LDA), 0.99 eV (LDA+U) and 2.02 eV (HSE) and for the optical band gap 0.99 (LDA), 1.88 eV (LDA+U) and 2.5 eV (HSE). [145] 56
5.4 Band structure of Cu_2O with consideration of copper vacancies. Around Γ and along Γ-X the VBM crosses the Fermi level contributing hole states for p-type conductivity. [146] 56
5.5 left: Structure and Brillouin zone of CuO. Arrows indicating the antiferromagnetic ground state and high symmetry points are shown. right: Band structure of CuO with an indirect band gap at Γ-D and the resulting DOS as calculated in hybrid functional DFT. The calculated values for the indirect band gap are 1.39 eV (LDA+U) and 2.74 eV (HSE) and for the direct band gap at B-point 1.91 eV (LDA+U) and 3.26 eV (HSE). [145] 57
5.6 left: Structure and Brillouin zone of Cu_4O_3. Arrows indicating the antiferromagnetic ground state and high symmetry points are shown. right: Band structure of Cu_4O_3 with an indirect band gap at Γ-N and the resulting DOS as calculated in hybrid functional DFT. The calculated values for the indirect band gap are 1.2 eV (LDA+U) and 2.54 eV (HSE) and for the direct band gap at Γ-point 1.47 eV (LDA+U) and 2.71 eV (HSE). [145] 58
5.7 (a+b) local density of states of copper and zink vacancies in Cu_2O and ZnO respectively. (c+d) Schematic band diagram of Cu_2O and ZnO constructed from the interaction of the single vacancy levels (left) and the free metal ions (right). In Cu_2O holes from the vacancy can "float up" to the occupied VBM. [148] 60
5.8 Formation energies and ionization levels for intrinsic defects in Cu_2O under different preparation conditions. [148] 60
5.9 The $Cu_2O(111)$ surface top view and side view. Coordinativley saturated and unsaturated atoms are marked. [130] 61

5.10 $Cu_2O(110)$ surface top and side view. The topmost Cu atoms together with the topmost oxygen atoms form parallel zig-zag chains. [3] 62
5.11 Surface free energies of $Cu_2O(111)$ as calculated by Soon and Co-workers [3, 5]. 62
5.12 "29" (left) and "44" (right) structure of a $Cu_2O(111)$ overlayer on Cu(111) as found by Matsumoto and co-workers. Copper atoms are represented in white, (subsurface) oxygen atoms are (dark) grey. Cu_{cus} are missing from the surface. For the 29 structure also some oxygen atoms are missing. [27] 64
5.13 $(\sqrt{3} \times \sqrt{3})R30°$ as found by Önsten and co-workers. P1 maxima increase with annealing in UHV whereas P2 increase with annealing in oxygen. STM images (c,f) of $(4.4 \times 4.4)\,Å^2$ show both features P1 and P2. Two structural models are proposed: Model A (a,b) starts from the stoichiometric (1x1) surface (a) whereas Model B (d,e) starts with the (1x1)-Cu_{cus} surface (d). In both models P1 emerge upon the removal of 1/3 of surface oxygen ions (b,e). White balls indicate oxygen ions whereas dark and light grey balls symbolize Cu_{cus} and Cu_{csa} respectively. [18] 65

6.1 Hexagonal LEED pattern of the Au(111) single crystal at 100V electron energy 68
6.2 Square LEED pattern of the Mo(001) single crystal at 130V electron energy 68
6.3 Temperature as a function of heating power 69
6.4 Measurement of Au 4f with different pass energies and x-ray sources. In all cases the resulting binding energies are too small as compared to the expected value for Au 4f 7/2 at 84 eV binding energy from NIST database [96]. This results in the corrective energies shown in the right hand table. 70
6.5 Au 4f and Cu 3p Xp-spectra for different Cu evaporation times collected with Mg-Kα and Al-Kα X-ray sources. 71
6.6 Film thickness depending on evaporation time and linear fit. 72
6.7 Au 4f and Cu 2p spectra after subsequent annealing at different temperatures, each for 10min. While little Cu intensity is lost, Au intensities start to reappear at high temperatures. CuO seems to transform into Cu_2O upon annealing, as revealed by the disappearance of the characteristic Cu 2p satellite. 73

7.1 Cu 2p and O 1s spectra for three substrates after reactive copper deposition. Cu 2p shows no satellite and only little shift in binding energy between different samples. 76
7.2 O 1s peak positions for different substrates and comparison with literature references [96]. Distinction of oxygen species in Cu_2O, MoO_x and ZnO is not possible from O 1s alone. Again CuO can be ruled out. 78
7.3 Three distinct kinetic energies are found for Cu LMM representing metallic Cu, thin Cu_2O and thick Cu_2O. While the results for metallic Cu and thick Cu_2O match the expectations, the unusual thin Cu_2O LMM spectrum can be explained as a convolution of metallic Cu and Cu_2O. [160] 78
7.4 Wagner plot of own Cu-O data with references from NIST database [96]. For Au-Cu alloy no data on the Cu LMM kinetic energy could be found in literature. Samples prepared in the HPC are closest to bulk Cu_2O. Formation of CuO can be excluded at the preparation conditions. 80

7.5 Observed shift of modified Auger parameter depending on calculated nominal film thickness d showing the influence of the thin film nature on XPS measurements. Thick oxide samples (prepared in the HPC) are omitted from the plot. 80
7.6 Disregarding the preparations in the HPC, clear distinctions between the substrates can be seen in the Cu 2p binding energy. Exemption are metallic Cu films for the Au and ZnO substrates. 82
7.7 The O_2 pressure in the HPC ($\geq$0.1 mbar) leads to a shift in Cu LMM kinetic energies as opposed to 1×10^{-6} to 9×10^{-6} reached in the preparation chamber. Substrates used can be seen from Fig. 7.6. 82
7.8 Influence of the temperature on the Cu_2O thin film preparation. Generally temperatures in the HPC were higher than during reactive copper deposition. However during annealing higher temperatures are possible in the preparation chamber. 82
7.9 Distribution of O_2 chemical potential among the preparations. 82
7.10 XPS lines for Au, Mo and ZnO substrates before and after reactive copper deposition. Whereas Au and ZnO remain largely unchanged Mo develops a high energy shoulder from MoO_x formation. For the latter, the two Mo phases were fitted with an asymmetric Doniach Sunjic function, after removing a Shirley background [160]. 83

8.1 $Cu_2O(111)$ on Au(111) coincidence lattice. blue solid: Cu_{cus}, blue hollow: Cu_{csa}, red solid: O_{cus}, red hollow: O_{csa} 86
8.2 Herringbone-type surface reconstruction of Au(111). Topographic image $(40\times40)\,nm^2$ 1.15 V bias voltage, schematic top [167] and side [165] view as well as Shokley-type surface states [166]. 87
8.3 As-grown Cu_2O film (A) exhibiting the donut phase and stripes along the Au[112] direction (B) as well as corresponding LEED image (C) and atomically resolved details of both as-grown phases (D). 88
8.4 Post-annealed Cu_2O film (A) exhibiting the hexagonal phase (B) as well as respective LEED image (C) and atomically resolved detail of the hexagonal phase (D). 89
8.5 Stripe [110] phase as observed in annealed films. (A) and (B) show the first [110] stripe version, (C) shows a second version of the [110] stripes. . 90
8.6 Different surface structures on post-annealed Cu_2O film. (A) herringbone reconstruction coexisting with hexagonal Cu_2O, (B) smooth areas also coexisting with hexagonal Cu_2O, (C) stripes with complex atomic arrangement and (D) triangular domains. 91
8.7 Stability diagram for 1 ML $Cu_2O(111)$ by Goniakowski (left) and Lee (right). In the right picture p2 denotes the (1×1)-Cu_{cus} surface. In both calculations the copper deficient surface is the most stable for 1 ML in the relevant range of oxygen chemical potentials. left [163], right [177] 93

8.8 3 ML of $Cu_2O(111)$ supported on Au(111) (a) Structural model of the stoichiometric $Cu_2O(111)$ surface. In the Cu-deficient surface Cu_{cus} is missing. (b) Film formation energies as calculated in GGA and HSE with respect to bulk cuprous oxide as a function of the oxygen chemical potential. Vertical lines indicate the limit of formation of bulk Cu_2O. (c) Cu-deficient (top) and stoichiometric (bottom) surface DOS calculated in HSE. (d) Simulated STM image of the stoichiometric termination at 2 V sample bias. [179] 95
8.9 6 ML of unsupported (1×1)- $Cu_2O(111)$ (a) Film formation energies as calculated in GGA and HSE with respect to bulk cuprous oxide as a function of the oxygen chemical potential. Vertical lines indicate the limit of formation of bulk Cu_2O. (b) Cu-deficient (top) and stoichiometric (bottom) surface DOS calculated in HSE. [179] 96
8.10 Differential conductance spectra of the hexagonal phase. The band gap is ≈ 1.9 eV with a pronounced surface state below the CB edge. For different domains of the hexagonal phase, different variations of the surface state were found. See Fig. 8.11 as well. 97
8.11 dI/dV maps of an annealed film $(32\times32)\,nm^2$ Up to 0.7 V bias voltage the conductance is low, due to the band gap. Starting at 0.8 eV the conductivity rises, due to the surface state (also seen in Fig. 8.10. In the topographic image different domains can be distinguished by the apparent contrast. In the "dark" domain a larger surface state occurs, as seen by the red color in the dI/dV map. This is also visible in the differential conductance spectra Fig. 8.10. 98
8.12 Unit Cell in derivative mode (bottom), topographic image (right) and structure model (left) of the hexagonal phase. blue solid: Cu_{cus}, blue hollow: Cu_{csa}, red solid: O_{cus}, red hollow: O_{csa}. The contrast stems from the Cu_{cus} and different tunneling conditions into nearby oxygen atoms. The domain border follows a zig-zag path along Au(110) with the mean direction along Au(112). The Cu_2O unit cell is elongated in the direction of Au(112) and squeezed in the direction of Au(110). Visible spots are Cu_{cus} (dark blue) matching the marked spots from the topographic image. 99
8.13 Topographic image, ball model and simulated STM image of the stripe [110]I phase 100
8.14 Topographic images and structure model of the stripe [110]II phase encountered in the annealed films. 101
8.15 Differential conductance spectra of both instances of the stripe 110 phase. For comparison the differential conductance of the hexagonal phase (×2) is also shown. There is a certain variability in the spectra on both types, however, no surface state directly below 1 V could be found in the [110] phase. 102
8.16 Right: Topographic image and structure model by Lee et. al of the donut phase. Left: Improved model with better match of the distance between the rings. The visible contrast comes from the oxygen atoms making up the six-membered rings which are interconnected by a hexagonal arrangement with 12.5 Å spacing. Bottom right [168], top right [177] 103
8.17 Topographic images and structure models of the stripe [112] phase encountered in as-grown films. 104

8.18 Differential conductance spectra of the stripe [112] and donut phase with the hexagonal phase (scaled ×4) for comparison. The donut phase shows the same surface state below the CB (around 0.8 V) as the hexagonal phase whereas the stripe [112] phase only shows the CB onset at 1 V. . . . 105
8.19 dI/dV maps of an as-grown film showing different electronic properties of donut and stripe(112) phase. The onset of a surface state in the donut phase at 0.55 V and in the stripe [112] phase at 0.75 V can be seen. At 1.5 V the conductance is more uniform as the conduction band is reached. [168] 106
8.20 (A) Measured STS showing the surface state onset for the herringbone and smooth areas as well as the band gap of Cu_2O for comparison (not to scale). (B) and (C) references for gold and copper surface states from literature. 107
8.21 dI/dV maps $(30\times30)\,nm^2$ of a smooth area surrounded by $Cu_2O(111)$ easily distinguished by the hexagonal atomic pattern. $(30\times30)\,nm^2$ Red color corresponds to a high conductivity. At negative bias the smooth area has higher conductance than the Cu_2O although the difference is more pronounced at positive bias where the surrounding Cu_2O has the higher conductivity. 107
8.22 Topography and dI/dV image of a copper oxide film on a gold substrate $(30\times30)\,nm^2$. Red color corresponds to a high conductivity. At 0.8 V the Cu_2O identified by the hexagonal atomic pattern has higher conductivity than the gold substrate identified by the herringbone reconstruction. . . . 108
8.23 Phase diagramm of observed surface structures for Cu_2O on Au(111) . . . 110
8.24 Native defects and ad-particles on the hexagonal phase. (B) Ad-particle on top of a O_{cus} site (in the three-fold hollow Cu_{cus} place). This is a first building block of the next $Cu_2O(111)$ layer. (C) Defect structure that may possibly be assigned to a Cu_{cus} vacancy with surrounding Cu_{cus} relaxing towards the vacancy. (D) 6 Cu_{cus} in an unusually close configuration, creating a brighter contrast. (E-G) hight profile of three different particle sizes 112
8.25 Ad-particles on the [110] stripe phase appear on fixed positions on the site of the elongated feature. They could mark an isolated Cu adatom or a Cu-trimer or more likely a O-Cu_3 building block attached to the Cu_{cus}. 113
8.26 Ad-particles on the [112] stripe phase, commonly on the triangular features or in between the stripes. 114
8.27 Ad-particles on the 122 stripe phase and corresponding dI/dV image showing the difference in conductivity for the different particle sizes. . . . 114

9.1 Typical STM images ($(100\times100)\,nm^2$, derivative mode) showing the topography of samples obtained via reactive Cu deposition in oxygen atmosphere on (a) Au(111) and (b) Mo(001). (a) A homogeneous film develops on gold. The inset ($(15\times15)\,nm^2$) shows the Cu_2O-surface with atomic resolution. (b) Cu nano-particles are found on Mo(001). Typical shapes are marked by dashed polygons. [160] 116
9.2 Different particle shapes on Mo(001) after reactive copper deposition as seen in STM images (derivative mode). (a+b) large and small (100) terminated octahedron ($(10\times10)\,nm^2$) (c) Several (100)-type particles with identical orientation ($(30\times30)\,nm^2$) (d) Atomically resolved top facet ($(3.5\times3.5)\,nm^2$) with a O(2×2) superstructure as illustrated in the ball model. [160] . . . 117

9.3 Other Cu particle shapes found on Mo(001) (a) (110)-terminated Cu particle ((10×10) nm^2) (b) toppled configuration ((15×15) nm^2) [160] 118
9.4 Different growth models for Cu+O on (a) Au(111) and (b) Mo(001). [160] 120

List of Tables

5.1 Structural properties of copper oxides [52] 54
5.2 Experimentally determined band gaps of different copper oxides. 55
5.3 Structural properties of Cu_2O surfaces [52] 61

6.1 Calculated film thickness depending on evaporation time and values for linear fit. 72

7.1 Mean and standard deviation of copper and oxygen XPS lines as found in the NIST database [96]. 76
7.2 Table of preparations and XPS peak positions with T Temperature, p_{O2} oxygen partial pressure, μ oxygen chemical potential, d nominal film thickness, Cu LMM line shape and modified Auger Parameter. Most samples are as-grown, while some have been annealed in UHV or O_2 after preparation. 77

8.1 Overview of favoured $Cu_2O(111)$ surface terminations from different theoretical works. In the case of one mono-layer the copper deficient surface is the most stable. For films of more than one mono-layer the stoichiometric surface is favoured. 96
8.2 Number of as-prepared and post-annealed samples showing the respective surface structures. 108
8.3 Phase diagram of observed surface structures. d: nominal film thickness as calculated from the evaporation rate and time Annealing was done under UHV conditions or in oxygen partial pressures. The temperature was monitored via the pyrometer or calculated from the heating power. . 109
8.4 Four preparations showing the ad-particles on different surface structures. The preparations are either "as-grown" (E) or "post-annealed" (A) at the given temperature and oxygen pressure. 111

9.1 Lattice mismatch, oxidation enthalpies and surface free energies of copper, molybdenum and gold define the growths mechanisms for Cu+O on Au(111) and Mo(001). 120

Abbreviations

CB	**C**onduction **B**and
CBM	**C**onduction **B**and **M**inimum
csa	**c**oordinatively **sa**turated
cus	**c**oordinatively **uns**aturated
DOS	**D**ensity **o**f **S**tates
donut	german spelling for **doughnut**
FER	**F**ield **E**mission **R**esonances
GGA	**G**eneralized **G**radient **A**pproximation
HPC	**H**igh **P**ressure **C**ell
LCAO	**L**inear **C**ombination of **A**tomic **O**rbitals
LDA	**L**ocal **D**ensity **A**pproximation
LDOS	**L**ocal **D**ensity **o**f **S**tates
LEED	**L**ow **E**nergy **E**lectron **D**iffraction
LT	**L**ow **T**emperature
PV	**P**hoto-**V**oltaic
QMS	**Q**uadrupol **M**ass **S**pectrometry
STM	**S**canning **T**unneling **M**icroscopy
SQL	**S**hockley-**Q**ueisser-**L**imit
UHV	**U**ltra **H**igh **V**acuum
VB	**V**alence **B**and
VBM	**V**alence **B**and **M**aximum
XPS	**X**-ray **P**hotoelectron **S**pectroscopy

Part I

Introduction and Setup

Chapter 1

Introduction

As fossil fuels are finite while the demand for electric energy is rising more attention turns towards renewable energies. Solar cells are an application already widely in use today. The conversion of light intro electric energy is done by absorption of photons in a semi-conducting material, the absorber. A semi-conductor is characterized by the band-gap between the filled valence band and the empty conduction band. After absorption of a photon a hole is left in the valence band and an electron is excited to the conduction band. Both charge carriers now have to be spatially separated to become usable. This happens at the junction between the absorber and a metal or another semi-conducting layer. If a metal is used this is called a Schottky junction. In the case of a second semi-conductor a hetero- or homo-junction is formed. Semi-Conductors can be n- or p-type conductors, meaning the electric current is made up of primarily electrons ore holes, respectively. These are the majority charge carriers. However, electrons (holes) can also be transported in p- (n-) type semi-conductors, called minority charge carriers. Thus, both types of charges reach the appropriate contacts.
The conversion efficiency of photons into charge carriers (electrons and holes) is amongst other things determined by the solar spectrum and the band gap of the absorber material. According to the Shockley-Queisser-Limit a theoretical maximum of 33.2% is reached for the internal quantum efficiency in a single-junction solar cell if the absorber material has a band gap of 1.34 eV. The efficiency can be enhanced to 41% if the light is focussed on the solar cell, however the optimum band gap decreases to 1.1 eV. So far photovoltaic devices have reached conversion efficiencies of 20-30% and 30-40% for commercially available devices and lab records respectively [6–8].
Development of solar cells tries to find better absorber materials. The "classic" absorber is crystalline silicon, a semi-conductor with an indirect band gap of 1.1 eV. Although it is abundant and non-toxic it also needs to be at least 50 μm thick [9] for effective

solar absorption. Such thick films are very brittle, so they used to be fabricated on glass substrates making the solar cell heavy and difficult to handle.

In recent years development has turned towards thin film solar cells. These use absorber materials that have much higher absorption coefficients ($10^5\,\mathrm{cm}^{-1}$) and thus can be much thinner ($\leq 2\,\mu\mathrm{m}$). Because of the thinness multiple absorber layers can be stacked in double and triple cells to increase the usage of light from the solar spectrum thereby increasing the overall conversion efficiency. Another advantage of thin film absorbers is that they can be fabricated on flexible substrates making role-to-role processes feasible thus lowering the production costs. Also shipment and handling of flexible solar cells is easier as compared to silicon solar cells on glass substrates.

A thin film material is prepared by individual atomic reactions during preparation by for example evaporation or sputtering. Due to the atomistic development process their structural, stoichiometric, electrical and optical properties depend greatly on the preparation conditions. With a thorough understanding of thin films the preparation can be undergone in a way to create thin films matching specific applications like solar cells.
The most research has been done for CIS/CIGS (Cadmium-Indium-(Gallium)-Selenid) thin film solar cells reaching around 20% conversion efficiency [10]. However the elements used in these absorbers are toxic, harmful to the environment, rare and expensive. A potential absorber material that is non-toxic, environmentally friendly, earth-abundant and cheap is cuprous oxide (Cu_2O).

Cu_2O is a semi-conductor with a direct band gap of 2.1 eV which can be fabricated as a thin film. Additionally by changing the oxidation level the band gap can be tuned between 2.1 eV for Cu_2O and 1.4 eV for CuO (cupric oxide) possibly optimizing the conversion efficiency for Cu-O based solar cells.
Research on Cu_2O began in the 1920s and development of Cu_2O based solar cells started in the 1970s. Those cuprous oxide solar cells used mainly a metal-Cu_2O junction for the charge separation. However conversion efficiencies stayed as low as 2%. The main problem was identified as a copper-enriched region between the Cu_2O and adjacent metal layers for almost all metals [11] effectively rendering all Schottky-type Cu_2O solar cells Cu/Cu_2O devices.
By combination of p-type Cu_2O with an n-type layer such as ZnO [1, 12–16] heterojunction Cu_2O solar cells can be built. However these are sill hampered by reduction of Cu_2O at the interface. Recently a Cu_2O solar cell reached 5.38% conversion efficiency using Ga_2O_3 as n-type counterpart [2]. The improved performance was related to the surface condition of the Cu_2O sheet before Ga_2O_3 deposition and decreasing defect levels at the Ga_2O_3/Cu_2O interface. This shows that a better knowledge of the Cu_2O thin film down to the atomic level is required to improve Cu_2O solar cells.

Moreover Cu_2O is interesting as a p-type conductor for electronic devices, optoelectronics as well as high-temperature superconductivity [17]. The studies of Cu_2O encompass powder, bulk and thin film samples [4, 18–20]. A variety of experimental methods have been used such as optical examination (REM, SEM, optical microscope), chemical analysis (XPS, AES), diffraction techniques (XRD, LEED) and scanning probe microscopy (STM, AFM) to learn about the optical, chemical, structural, atomic and electronic properties of cuprous oxide and the other copper oxide phases [18, 19, 21–28]. In studies where no powder or bulk samples were used oxidation of copper was carried out by oxidizing bulk copper (thermally or chemically) to create thin copper oxide layers.
To sample the atomic and electronic structure, scanning probe microscopy and especially the scanning tunneling microscope (STM) has been used [18, 26–28]. By scanning a sharp metal tip over the sample the morphology and the atomic corrugation can be visualized. Additionally the distribution of electronic states can be quantified. To interpret data collected with STM usually density functional theory (DFT) is used. DFT predicts the local electron density of multi-electron systems such as a surface which can be compared to the results from STM. Most often the local density approximation (LDA) is used which is know to underestimate the band gap of semi-conductors due to the underestimation of electronic localization effects. Using the combination of STM and DFT an analysis of the surface composition can be made.

In this thesis Cu_2O thin films were prepared by reactive copper deposition in an oxygen atmosphere with and without subsequent annealing at higher temperatures (around 650 K) to drive the films closer to thermodynamic equilibrium. Gold and Molybdenum were used as chemically inert and reactive substrates respectively. The atomic and electronic structure was explored using Scanning Tunneling Microscopy and Spectroscopy. The chemical composition was revealed using X-ray Photoelectron Spectroscopy. The experimental findings were compared to improved DFT calculations and explained by structure models of the observed surface structures. The thesis starts with an introduction to the theory behind the experimental techniques and the experimental setup. Also a short overview on thin film solar cells is given. In the second part of the thesis the scientific results are shown. First, the main properties of Cu_2O are introduced and the preparation process used in this work is shown, followed by the results of the chemical analysis done with XPS. In the main chapter Cu_2O thin films on a Au(111) substrate are presented. A variety of examined surface structures are rationalized by DFT calculations and structure models. Afterwards the influence of the substrate is demonstrated by examining Cu_2O on a Mo(001) substrate. Finally, a summary of the entire work and an outlook on possible future work is given.

Chapter 2

Thin Film Solar Cells

2.1 Introduction

Development of photovoltaic (PV) devices started in 1954 with the discovery of a Silicon based p-n junction [29]. Since then the efficiency of silicon-based solar cells has improved to about 25% [9]. Generally a solar cell is a device that converts photons to charge carriers (electrons and holes) in the absorber material. After being generated the charges need to reach the electric contacts of the cell by diffusion without recombination. The best absorber material for solar cells will convert the most photons and collect the most charge carriers at the contacts.
Ideal PV materials are direct band gap semiconductors with a band gap of 1.5 eV, a high solar optical absorption (10^5/cm), a high quantum efficiency of optical excitations, long diffusion lengths, low recombination velocity and good electronic conductivity to contact materials [9]. Unfortunately there are no such semi-conductors. Silicone has an indirect band gap of 1 eV and is by no means ideal as a photovoltaic material.
There are a number of alternative absorber materials in different stages of research and development: Amorphous hydrogenated Silicone (a-Si:H) [30], various two-compound (binary) and three-compound (ternary) thin-film materials such as CIS and CIGS [31, 32] as well as a variety of other thin film materials [33] and organic semi-conductors [34, 35].

Thin film absorbers stand out from classical silicon based solar-cells by their physically distinct nature. In contrast to the indirect band-gap of silicone thin film materials like CIGS or CIS have a direct band gap making them superior absorbers. Additionally the thin layers make multi-junction solar cells feasible increasing the spectral bandwidth that can be harvested from the sun's light. Also, thin and flexible substrates make role-to-role production of large solar panels possible. Transport, handling and integration into buildings, vehicles and devices are much easier as compared to silicon based solar

cells which are usually fabricated on brittle, thick and heavy glass substrates.
The unique way of individually condensing or reacting atomic, ionic or molecular species on a substrate to produce a thin film makes their properties controllable. Band gap and lattice constant as well as electric properties and diffusion at surfaces and interfaces can be tailored [9]. In the case of copper oxide the band gap can be tuned from 2.1 eV for cuprous oxide to 1.4 eV in cupric oxide by changing the oxidation level. The tuneable band gap makes for a better absorption cross-section as compared to other thin-film absorbers. Also copper as main ingredient is abundant, low-cost, easy to handle, non-toxic and environmentally friendly.

2.2 Theory

The figure of merit of a solar cell is the overall conversion efficiency that describes the transformation of the incoming light into electric energy. The overall efficiency is put together from different aspects such as the absorption efficiency, charge carrier separation efficiency and conductive efficiency. Because these parameters are difficult to measure independently other parameters are usually substituted which can best be explained by looking at the I-V-curve of a typical solar panel.

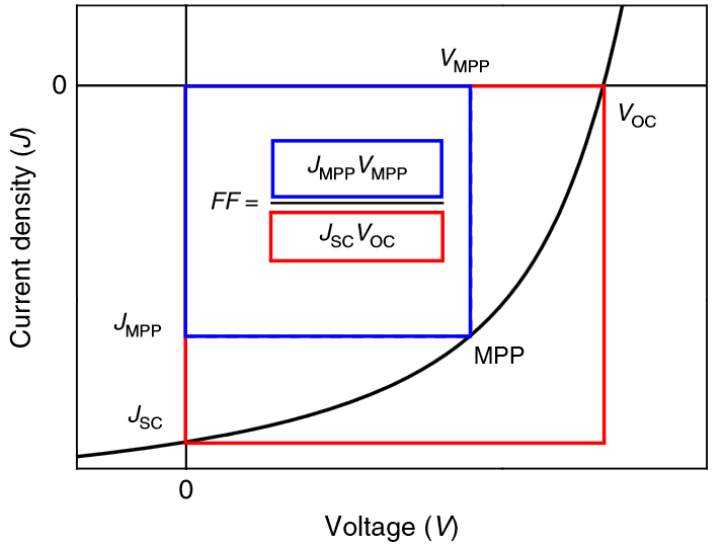


FIGURE 2.1: I-V-curve of an illuminated solar cell. Maximum power point and fill factor are indicated. [36]

The maximum power point MPP is where the solar cell in usual operating conditions (connected to the load such as batteries and inverters) outputs the most power. The maximum power is calculated by $V_{\mathrm{MPP}} \times I_{\mathrm{MPP}}$.
The open-circuit voltage V_{OC} is the maximum voltage the cell provides when not connected to a load. It is higher than the voltage at the maximum power point which relates

to the solar cell with the load connected.
The short-circuit current I_{SC} is the maximum current the photovoltaic device can provide when the output connectors are shorted together. It is higher than the normal operating current I_{MPP} for the solar cell with the load connected.
The fill factor FF gives the ratio of maximum power under normal operating conditions $V_{MPP} \times I_{MPP}$ and the theoretical power calculated by $V_{OC} \times I_{SC}$. Better solar cells achieve a higher fill factor. Typical values are between 0.7 and 0.9 [9, 37] but can also be a lot lower.
The efficiency η is the ratio of electrical output power to the incoming light energy P_{in}. It can be calculated as [37]

$$\eta = \frac{V_{MPP} \cdot I_{MPP}}{P_{in}} = \frac{V_{OC} \cdot I_{SC} \cdot FF}{P_{in}} \tag{2.1}$$

Usual conversion efficiencies are around 10-14 % for commercially available devices [9]. To obtain an optimum solar cell the best overall conversion efficiency has to be aimed for which means that some parameters might be below their individual maximum.

2.2.1 Junction

A junction is created when two semi-conductors are brought into contact. Both semi-conductors start out charge-neutral, i.e. with the same amount of electrons and holes in each semi-conductor. If however in the first semi-conductor are more free electrons than in the other, electrons will start to diffuse into the second semi-conductor. There they will occupy the hole states and produce a negatively charged area.
The same holds for holes but they diffuse from the second semi-conductor to the first. This way a space charge area (also called depletion zone) with a built-in voltage drop is created.
The difference in charge density can be created by choosing two different semi-conductors (hetero-junction) or twice the same semi-conductor but with different dopants (homo-junction). If one semi-conductor is doped n-type (additional electron donors) and the other is p-type (additional electron acceptors) the junction is called a p-n-junction. Likewise a n-n-junction or p-p-junction is possible if different charge carrier concentrations are present. A metal/semi-conductor junction is called a Schottky-junction.

In the vicinity of a junction band-bending will occur due to the built-in voltage drop and the mismatch in Fermi energies. A barrier with a height depending on the exact device configuration is created. By applying a voltage the width of the space-charge region can be changed. If a voltage is applied between the two semi-conductors, such that the positive pole is connected to the p-doped material and the negative pole to

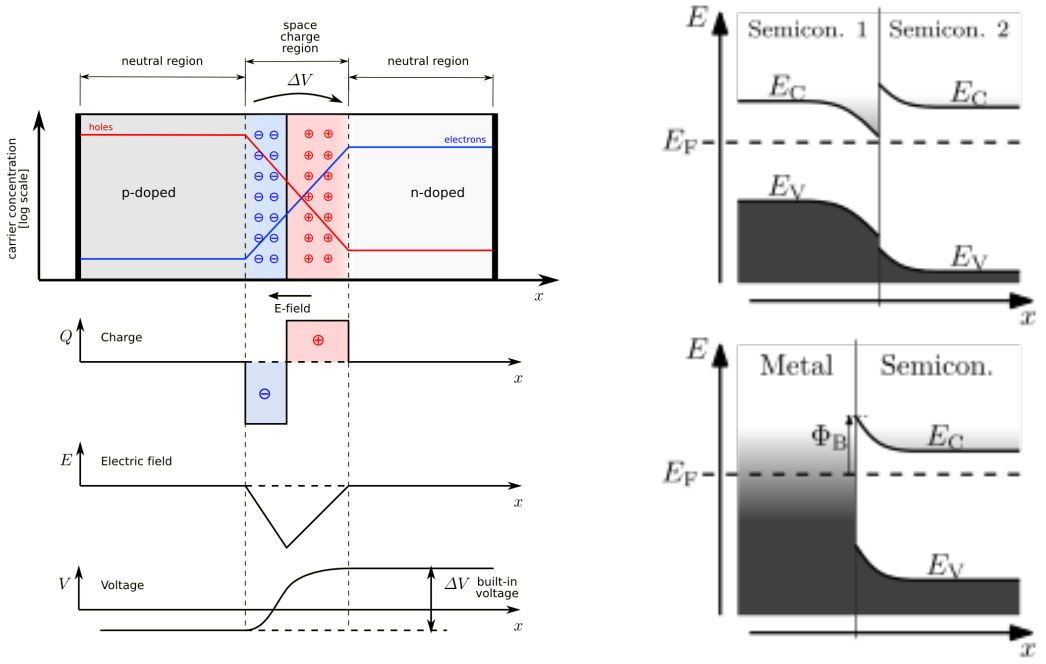


FIGURE 2.2: Left: Space charge area in a p-n-junction, according charge distribution, electric field and voltage gradients. right: Band bending in different junctions. [38–40]

the n-doped (forward bias) holes from the p-doped side are pushed towards the junction neutralizing the negative charges there while electrons from the n-doped side are pushed towards the junction neutralizing the positive charges on the other side of the depletion zone. Thus the space charge zone becomes smaller and charge carriers can pass more easily. An electric current starts to flow.

If a voltage is applied to the junction in reverse direction the depletion zone widens and no current can flow. If the potential of the barrier is low enough charges can tunnel through much like in the STM. In this case a reverse current starts to flow if a critical reverse voltage is reached. A device working like that is called a Zener diode.

In solar cells with a p-n-junction the built-in voltage drop will pull electrons to the n-type semiconductor and holes to the p-type semiconductor, thereby separating the charges. If charge mobility is sufficient both charge carriers will reach a metallic electrode at the respective sides of the absorber and thus contribute to the current generated by the photovoltaic device.

2.2.2 Energy Conversion Efficiency

The more of the incoming photons that can be converted to electric energy the better the solar cell's efficiency. If all incoming photons could be converted the energy conversion efficiency would be 100%. Unfortunately there are limits to the conversion efficiency. The

thermodynamic limit is at 85% which can be calculated by looking at a Carnot machine [37, 41]. A Carnot machine extracts power from the temperature gradient between a hot absorber and the colder environment. To model the maximum efficiency of a solar cell the absorber is heated by the sun's radiation. Both the sun and the absorber are considered as black bodies. As long as no power is extracted from the absorber it will reach the same temperature as the sun $T_S = 5800\,\mathrm{K}$. However, if power is extracted from the absorber it can be done with an efficiency according to Stefan-Boltzmann's law

$$\eta_{\mathrm{ext}} = 1 - \frac{T_A^4}{T_S^4} \tag{2.2}$$

This will of course decrease the temperature of the absorber. The extracted power will then be converted into electric energy by the Carnot machine following the Carnot-efficiency [42, 43]

$$\eta_{\mathrm{Carnot}} = 1 - \frac{T_0}{T_A} \tag{2.3}$$

Because the absorber is located on earth the temperature of the environment is $T_0 = 300\,\mathrm{K}$. Now the overall efficiency $\eta = \eta_{\mathrm{ext}} \times \eta_{\mathrm{Carnot}}$ can be calculated. By varying T_A the efficiency can be maximized. With $T_S = 5800\,\mathrm{K}$ and $T_0 = 300\,\mathrm{K}$ a maximum of $\eta = 0.85\%$ can be found for $T_A = 2478\,\mathrm{K}$.

However solar cells use semi-conductors as absorbers which in contrast to black bodies can absorb high energy radiation at low temperatures. Naturally they are still limited by the thermodynamic limit. While semi-conductors can almost reach the thermodynamic limit for the conversion of monochromatic light they are less efficient at harvesting spectrally broad radiation like the sunlight [41].
When absorbing a photon in a semi-conductor an electron is excited from the valence band to the conduction band. Only photons with energies higher than the band gap can be converted. This leads to the Shockley-Queisser-limit [44] for solar cell efficiency. Each electron carries energy equal to eU_{Gap}. Electrons with larger energies (smaller wavelengths) can still be converted but the extra energy is quickly lost because the electron will relax to the band edge by e.g. phonon excitations.
A large band gap thus means a small number of electrons however with high energy.
A small band gap means a large number of electrons, yet with little energy.
The energy stored in the sun's radiation depends on the energy of each photon $h\nu$ and the frequency dependent photon-distribution $f(\nu)$. Thus the incoming lights energy is

$$E_{\mathrm{light}} = \int_0^\infty h\nu f(\nu) d\nu \tag{2.4}$$

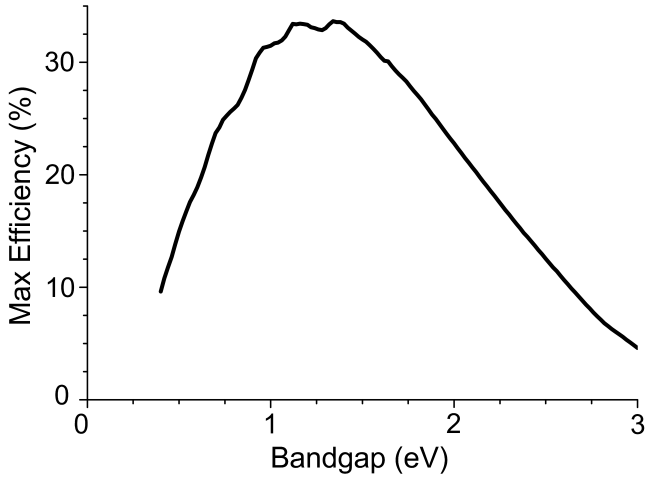


FIGURE 2.3: Maximum conversion efficiency for a single junction solar cell depending on the band gap of the semi-conducting absorber material. [45]

All photons with $\nu \geq E_{\mathrm{Gap}}/h$ can be absorbed. The resulting electrons however will relax until their energy reaches E_{Gap}. Thus the energy for all converted electrons is

$$E_{\mathrm{electrons}} = E_{\mathrm{Gap}} \cdot \int_{E_{\mathrm{Gap}}/h}^{\infty} f(\nu) d\nu \tag{2.5}$$

The efficiency $\eta = E_{\mathrm{electrons}}/E_{\mathrm{light}}$ reaches a maximum of 31% at $E_{\mathrm{Gap}} = 1.3\,eV$ for single junction devices as shown in fig.2.3. If the light is focussed onto the solar cell efficiency reaches 41% at $E_{\mathrm{Gap}} = 1.1\,eV$. Multi junction solar cells can be designed to reach better values [31].

2.3 Design of a Solar Cell

A solar cell is not only the light absorbing semi-conductor and the charge-separating junction. Before looking at potential absorber materials, the other parts of the solar cell are discussed first.

Apart from the absorber material a solar cell needs two electrodes to collect the charges (back and front contact), a substrate on which the different layers are fabricated and a window to shield the solar cell against environmental hazards. If one of the two electric contacts will be on the light-facing side of the absorbing layer, it has to be transparent. A possible solar cell setup is shown in Fig. 2.4.

As far as possible photovoltaic materials are selected the following aspects need to be considered: lattice constant, electron affinity, work-function and thermal expansion coefficient between adjacent layers [9].

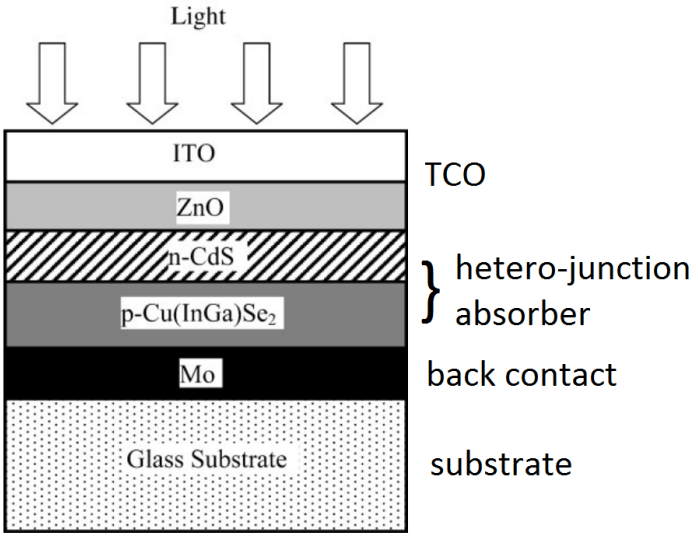


FIGURE 2.4: Possible composition of a hetero-junction solar cell using CIGS as absorber and ZnO as transparent conducting oxide. [9]

The conductivity of the TCO-layer depends on the carrier concentration and mobility. Most often n-type semiconductors with good electric conductivity and high transparency in the visible spectrum (e.g. ZnO doped with Indium) are used. A low resistance contact to the absorber and transmission of most incident light must also be ensured [46–49]. The window has to admit a maximum amount of light to the solar cell. Thus the band gap of the window material has to be as wide as possible. No photo-current generation occurs in the window itself. The back contact creates an ohmic contact to the absorber layer. To do so the work function of the metal contact has to be chosen to match the typ of charges dominating the absorber layer. Low work function metals (Al, Ca, In, Ag) are used for electron, high work function metals (Au, Mo) for hole collection [9] The substrate is the material the other layers are deposited on during device fabrication. Therefore it is required to be mechanically stable, it has to match the thermal expansion coefficients of the deposited layers and should be inert during device fabrication. Over all the substrate is a passive component. In thin film solar cells the substrate can be made of thin plastic allowing the solar cell to be flexible which makes integration into buildings and devices easier. Also a thin and flexible substrate may allow for cheaper production of large solar cells due to the reduced risk of damage.

2.3.1 Absorber

In the aforementioned example of a solar cell the absorber is made of a junction from n-doped CdS and p-doped CIGS, but that is by far not the only option. Different materials for light conversion are discussed next.

There is a plethora of absorber materials for solar cells in use or in development like silicone [30], I-III-VI chalcopyrite materials such as CIS and CIGS [31], cadmium telluride (CdTe), organic semi-conductors [34, 35] , perovskites [50] and a variety of thin-film materials [33] just to name a few.
Silicone was one of the first materials to be used for photovoltaic applications [29]. It has a number of advantages, as it is naturally abundant, non toxic, it can be processed at low temperatures and can be used on flexible and low cost substrates. Amorphous silicone also features a reasonably high absorption coefficient due to its inherent disorder, which gives rise to a large number of allowed optical transitions [9]. Unfortunately a lot of inherent recombination centres and small grain sizes are responsible for reduced carrier life-time and prevent doping of amorphous silicone. Additionally amorphous silicone based solar cells tend to degenerate during the first month of usage due to the Staebler-Wronski-effect [51] that describes formation of light-induced metastable defects which lower the efficiency.

Much research effort in recent years went into the I-III-VI chalcopyrite materials. In particular $CuInSe_2$ can tolerate a wide range of anion-to-cation off-stoichiometry and is therefore less sensitive to impurities, grain sizes and crystallographic defects. It can be doped n- and p-type to a low resistivity by introduction of native defects. $CuInSe_2$ has a band gap of 1 eV, is one of the most absorbing materials and makes for an excellent junction. Efficiency is as high as 15.4% [9]. Increasing the band gap by alloying with Ga, Al or S is a way of increasing the performance [32]. On the down side manufacturing of CIGS is quite complicated and Indium and Gallium are rather expensive elements.

Thin film solar cells, in general, enable high conversion efficiencies of photons to charge carriers and high collection efficiencies of excited charge carriers. This is because of the possibility to tailor the structural (amorphous, nano-crystalline, oriented, epitaxially grown), as well as chemical and physical (band gap, Fermi energy, electron affinity, work-function) properties of a thin film by tuning a range of deposition parameters. If the deposition process can be controlled reliably the film parameters can be tuned to meet the requirements for a high performance solar cell. In contrast, badly calibrated deposition parameters will lead to thin films missing the desired characteristics.
In general, a thin film is prepared by the random nucleation of individual atomic, ionic, or molecular species on a substrate [33]. It is not a bulk material that has been thinned down (bottom-up approach). STM studies show that electrical properties of surfaces and interfaces differ significantly from those of bulk materials and depend greatly on the deposition process [52].

2.4 Cu_2O in Photovoltaic Devices

A promising material for a thin-film absorber is cuprous oxide, the exploration of which has started as early as 1925 [53]. A first Cu/Cu_2O solar cell was built in 1926 [54]. However it never gained great interest. Recently there is a renewed interest because of its abundance [24], sustainability and non-toxicity and numerous methods for low-cost thin-film production [52].
Bulk cuprous oxide features a band gap of 2.1 eV which is far from the predicted maximum at 1.4 eV according to SQL [44] limiting the maximum theoretical efficiency to 20%. The first Cu_2O based solar cells in the 1970s used mostly Schottky-type junctions but the conversion efficiency stayed as low as 2%. More recent Cu_2O solar cells use mainly hetero-junctions. Current experimental data for Cu_2O based solar cells is at 5% [2]. As Cu_2O is an inherently p-type semi-conductor [55, 56] and so far there was no successful n-type doping homojunction solar cells are not possible.
The properties of the p-type absorber govern the most important parameters of the photovoltaic device: absorption coefficient, direct or indirect band gap, band gap energy and transport properties including carrier mobility [52].

When combining the semiconducting layers one inherently faces problems of lattice mismatch, band alignment, band offsets and of low interface quality due to defects [52]. Limitations are also attributed to crystal orientation, grain size, series resistance due to high resistivity of the absorber layer as well as minority-carrier transport length [14]. In copper oxide hetero-junction solar cells the interface needs to be controlled to avoid reduction of Cu_2O [1]. Recent improvement on conversion efficiency was made with a cell consisting of Al-ZnO/Ga_2O_3/Cu_2O produced by Minami et al. [2]. According to Minami and co-workers the improved performance was due to the surface condition of the Cu_2O sheet before Ga_2O_3 deposition and a decrease of defect levels at the Ga_2O_3/Cu_2O interface rather than by the work function of the thin film. Thus to further optimize copper-oxide solar cells the established physical properties of thin-film cuprous oxide need to be reevaluated and poorly determined parameters need to be measured with high accuracy. After all thin film solar cells are only improving when a better understanding of thin film properties can be reached.

In this study, Cu_2O is examined as a model system for thin films on gold and molybdenum as examples for chemically inert and reactive supports respectively. In section 5 an overview on the physical and chemical properties of Cu_2O is given. In the next section the experimental techniques and the experimental setup to analyse the Cu_2O-films is presented.

Chapter 3

Experimental Techniques

3.1 Scanning Tunneling Microscopy

3.1.1 Introduction

Optical microscopy is limited to features of about 200 nm because of the finite wavelength of visible light. The maximum achievable resolution is given by Abbe's law [57]

$$d = \frac{\lambda}{2n\sin(\alpha)} \tag{3.1}$$

with d smallest distance between two distinguishable objects, λ wavelength of light, n refraction index and α half the aperture angle.

By using accelerated electrons instead of photons the wavelength λ can be reduced and the achievable resolution considerably improved. The drawbacks of electron microscopy invented in 1987 by Ruska [58] is the need of vacuum and a highly sophisticated system of lenses to focus the electron beam. Furthermore high energy electrons can interact with and possibly destroy the sample.
A new method of imaging surfaces called the Topografiner was invented in 1972 by Young et al. [59]. The setup uses a sharp metal tip as a field emitter which is scanned across the surface with the help of piezo ceramics. The measured current between tip and sample is directly proportional to the distance between tip and sample.

A very similar setup but this time using quantum mechanical principles was devised in 1982 by Binning and Rohrer [61]. The STM uses a sharp metal tip and a conducting sample with the tip-sample distance in the range of a few nano-meters. By applying a voltage between tip and sample a tunneling current starts to flow which is exponentially

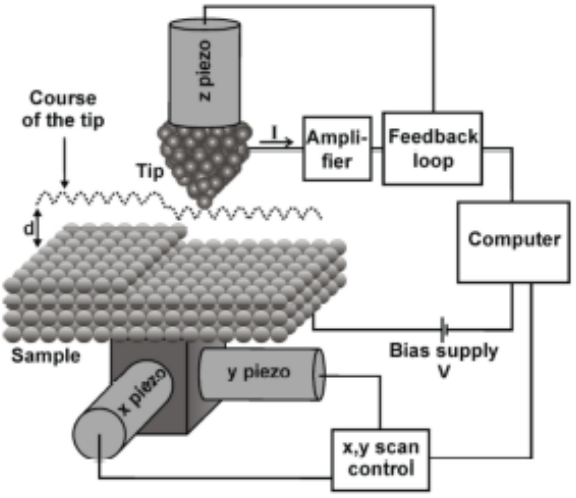


FIGURE 3.1: STM Setup with atomically sharp metal tip, sample and feedback loop. [60]

dependent on the distance. Using the new device the Si(111)7x7 surface reconstruction could be imaged with atomic resolution. Binning, Rohrer (tunneling microscopy) and Ruska (electron microscopy) were awarded the Nobel prize in 1987.

In modern physics Scanning Tunneling Microscopy and Scanning Tunneling Spectroscopy are routinely used to measure topography, electronic (local density of states), optical and magnetic properties (spin polarized tunneling) of metal and semi-conductor surfaces as well as of single atoms and molecules. A wider range of applications includes low temperature measurements, vibrational properties of molecules (inelastic electron tunneling spectroscopy) and photon emission STM. This variety of applications is possible because STM can be operated under various temperature and pressure conditions including for example ambient conditions and in liquids [62, 63].

3.1.2 STM Setup

Scanning tunneling microscopy uses the unique property of electrons flowing from the last tip-atom to the sample surface crossing the classically forbidden vacuum gap. The quantum mechanical tunneling current shows an exponential dependence on the distance between tip and sample. This allows for very sensitive placement of the tip above the sample (in the range of a few Å) when the current remains constant.
The basic components of any STM setup are shown in Fig. 3.1. A piezo system with three degrees of freedom is used for positioning the sample and scanning the atomically sharp and conductive tip above the surface. Scan ranges depend on the microscope used but can be up to $(500\times500)\,\mathrm{nm}^2$. To do so a high voltage source is needed which is applied to the piezos in order to shift the sample and move the tip. The electronics

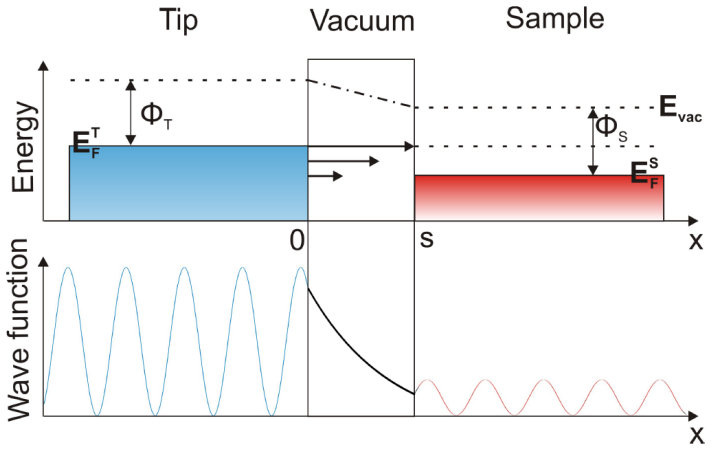


FIGURE 3.2: Sketch of a tunneling process through a one-dimensional barrier. The tunnel current depends exponentially on the tip sample distance. [64]

include the tunnel current amplifier, a supply for the bias voltage to be applied between tip and sample and a feedback loop which adjusts the tip in a way that the tunnel current is kept constant. The feedback loop can be entirely electronic but in modern microscopes sophisticated software is used.
The adjustment of the vertical tip position to keep a constant current results in different heights of the tip above a surface atom than between two atoms. The signal generated by the feedback to adjust the tip hight can be translated into atomically resolved images. With a vertical resolution in the sub-nm regime atomically resolved images are possible even for metal surfaces with small lattice constants and small corrugation (due to the delocalized electronic structure) as well as for surfaces with large corrugation or adfeatures without risking a tip crash because of the enabled feedback loop.

3.1.3 Calculating the Tunnel Current

An exact calculation of the tunneling current is very complicated because of the number of unknown parameters such as non-equilibrium condition or breaking of the symmetry in the tunnel junction. To get a basic understanding a 1-d tunnel junction and elastic tunneling are considered at the beginning.

The tunnel barrier is a potential with the following shape: (see Fig. 3.2)

$$V(x) = V_0 \qquad \text{for } 0 < \mathrm{x} < \mathrm{s} \tag{3.2}$$

$$V(x) = 0 \qquad \text{else} \tag{3.3}$$

an electron with energy $E < V_0$ and mass m can be described by its wave function $\psi(x)$:

$$\psi(x) = e^{kx} \qquad \text{with } k = \sqrt{\frac{2m(V_0 - E)}{\hbar^2}} \qquad \text{for } 0 < x < s \tag{3.4}$$

$$\psi(x) = e^{\pm iKx} \qquad \text{with } K = \sqrt{\frac{2mE}{\hbar^2}} \qquad \text{else} \tag{3.5}$$

The wave function $\psi(x)$ is a solution to the stationary Schrödinger equation for the system:

$$-\left[\frac{\hbar^2}{2m}\frac{\delta^2}{\delta x^2} + V(x)\right]\psi(x) = E(x) \cdot \psi(x) \tag{3.6}$$

At the edges of the potential barrier ($x = 0, x = s$) the Schrödinger equation has to be continuously differentiable. At each edge of the potential a part of the original wave function is transmitted while the other part is reflected. This results in a finite possibility that the electron can tunnel through the barrier. The transmission coefficient T for the barrier is given by the transmitted amplitude divided by the incident amplitude:

$$T = \frac{I_{\text{trans}}}{I_{\text{in}}} = \frac{1}{1 + \frac{(K^2+k^2)^2 \sinh^2(ks)}{4K^2k^2}} \tag{3.7}$$

In the case of a large barrier, i.e. $ks \gg 1$ the coefficient T becomes

$$T \approx \frac{16K^2k^2}{(K^2+k^2)^2} e^{-2ks} \tag{3.8}$$

with the exponential term giving the main contribution. So T depends strongly on the barrier width s and the effective barrier height $\sqrt{(V_0 - E)}$. This is a typical behaviour for the tunnel current regardless of the exact barrier shape. Because of the exponential dependence on the barrier width, i.e. the tip-sample distance, small changes in the range of a few Å lead to changes in the current of up to one order of magnitude. This makes the high resolution images possible that are typical for STM.

Bardeen [65] gives a formula to characterize a 3d metal-insulator-metal tunnel junction by using time dependent perturbation theory (Fermi's golden rule). The electron starts in an unperturbed state μ with wave function ψ_μ in front of the barrier and ends up in a unperturbed state ν with wave function ψ_ν after the barrier. The transition probability T is characterized by the tunnel matrix element $M_{\mu\nu}$ with $|M_{\mu\nu}|^2 = T$ and

$$M_{\mu\nu} = -\frac{2m}{\hbar}\int ds(\psi_\mu \nabla\psi_\nu^* - \psi_\nu^* \nabla\psi_\mu) \tag{3.9}$$

The integral is evaluated in an area the current goes through. The difficulties in calculating $M_{\mu\nu}$ lies in finding the wave functions for tip and sample. Because the atomic

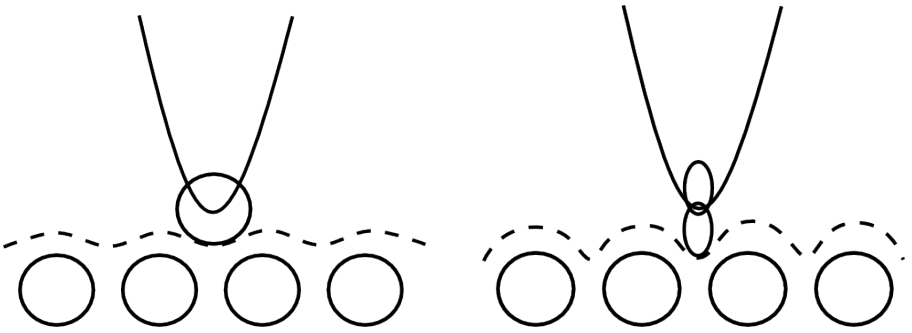


FIGURE 3.3: Tip trajectory with an s-orbital (left) and a p-orbital (right). Because of the directed shape of the p orbital the atomic corrugation of the sample is imaged at a higher resolution.

configuration of the tip apex is generally not known, Tersoff and Hamann [66, 67] assumed a single sphere-shaped s-orbital. They found the tunnel current I_T to depend on the applied bias voltage and the sample density of states (DOS) ρ_s at the tip position r_0 and the Fermi energy E_F:

$$I_T \propto eU_{\text{bias}}\rho_s(r_0, E_F) \tag{3.10}$$

The Tersoff-Hamann model however cannot describe high corrugations observed for some metal surfaces [68] as seen in STM. Chen [69] improved the model by allowing different tip-orbitals, for example the tungsten $3d_z^2$ orbital, to correctly reproduce the observed resolution [68]. One conclusion of this model is that not only the atomic structure of a surface but the density of states determines the resolution seen in STM.

3.1.4 STM on thin insulating films

On semi-conducting or insulating samples the tunneling current will result in charging of the sample, making it impossible to analyse their surfaces via STM. However semi-conducting and insulating materials can still be scanned in STM if they are prepared as thin films on a metal substrate, see [70]. The film has to be thin enough to allow electrons to flow into the metal substrate fast enough to prevent charging. A few monolayers are generally thin enough for STM analysis with readily observed atomic resolution but on the other hand the material already shows bulk features such as the band-gap value for semi-conductors. A few systems that have been studied extensively include NaCl on Al(111) and Al(100) [71], MgO on Mo(001) [72].

There are two possible scenarios for tunneling through such a thin film. If the bias voltage is below the band gap of the semi-conductor the electrons have to overcome two tunneling gaps: the vacuum and the insulating film as shown in Fig. 3.4. Only the metal states at the interface are accessible to tunneling electrons. However in many cases

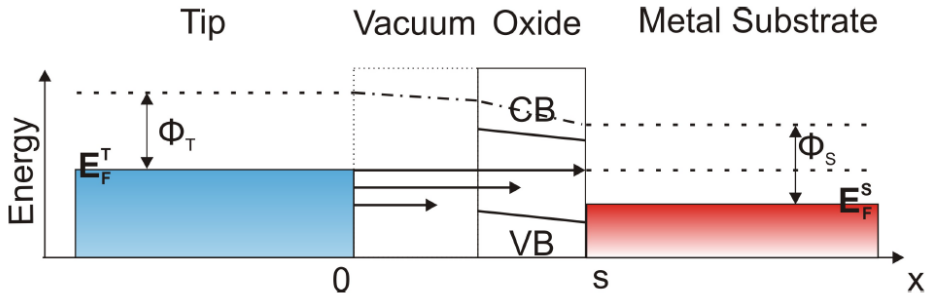


FIGURE 3.4: Schematic view of a tunnel junction consisting of the vacuum gap and the oxide layer on top of the metal substrate. The bias voltage is not large enough for electrons to reach the conduction band. CB and VB are bend due to the electric field across the tunnel junction. [64]

atomic resolution of the film structure is achieved showing that the tunneling matrix elements are influenced by the presence of the oxide film even at low bias.
Due to the tip electric field, band bending will occur in the oxide or semiconductor thin film. The amount of bending depends on the film thickness and its dielectric constant. Because of the band bending, tunneling into the CB or out of the VB becomes possible at electron energies not adequate to do so without the band bending as shown in Fig. 3.4. A full theoretical description of the process such as with the scattering theory [73] is still of interest to theoretical physics.
If the bias Voltage is larger than the band gap, the electrons have sufficient energy to reach the oxide band gap. In this case the apparent film height is closer to the real film height. But because of the large tip-sample distance atomic resolution is more difficult to achieve.

3.1.5 Scanning Tunneling Spectroscopy

Any STM image is a convolution of the topographic structure and the electronic features of the sample, as shown in section 3.1.3. Scanning Tunneling Spectroscopy (STS) can access the information on the electronic states contained in the tunnel current. The first derivative (dI/dV) shows the elastic contributions to the tunnel current, yielding information about e.g. the band gap and surface states. The second derivative (d^2I/dV^2) is used to show the inelastic contributions, e.g. vibrational states of a molecule located in the tunnel gap (i.e. on the sample).

dI/dV constant distance STS
The current measured in STM is proportional to the integrated local density of states (LDOS) ranging form the Fermi energy to the applied bias voltage. Thus the derivative of the current dI/dV is proportional to the LDOS and the transmission coefficient [68].

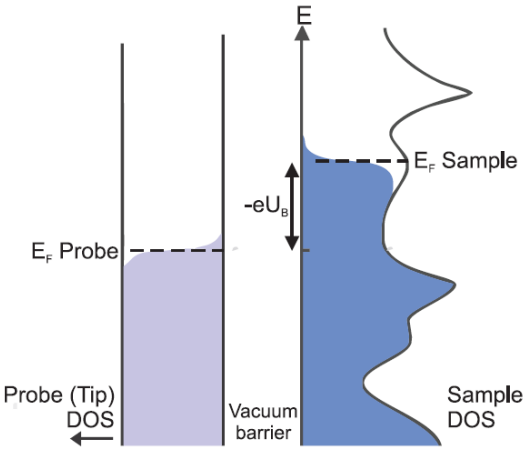


FIGURE 3.5: Tip DOS (left) and Sample DOS (right). Because of the applied bias voltage E_F (Sample) is offset with respect to E_F (Tip) electrons above E_F (Tip) are tunneling from occupied states in the sample into unoccupied states in the tip. The tunnel current depends on the number of available states in the tip and the sample. [74]

$$\frac{dI}{dV} \propto \rho_s(eU_{\text{bias}})T(d, E, eU_{\text{bias}}) \tag{3.11}$$

By ramping the bias voltage with the feedback turned off, the change in tunneling conductance at a given point above the sample surface can be analysed as shown in Fig. 3.5. Here, a lock-in amplifier is used to improve signal to noise ratio. A small AC signal is added to the bias voltage. A signal proportional to the resulting tunneling current is fed back into the lock-in amplifier where a phase-sensitive measurement dissects the signal to access dI/dV.

Because the feedback is turned off very small changes in U_{bias} can result in drastic changes in the current. That is why usually only small energy ranges (1-3 V) are recorded. STS is limited to energies below the work function of both electrodes (tip and sample) but provides access to both occupied and unoccupied electronic states simply by changing bias polarity. Because the contribution of electronic states from tip and sample are convoluted, the sample states can only be accessed easily under the assumption the density of states of the tip is a perfect step function. Electronic states with little extension perpendicular to the surface and therefore insufficient overlap with the tip electronic states (like d- and f-states) are hardly observed in STS [69].

dI/dV images

Sometimes it might be of interest to tie spectroscopic data to topographic images. By choosing the modulation frequency of the lock-in amplifier well above the cut-off frequency of the feedback and record in-phase current modulation with a lock-in amplifier

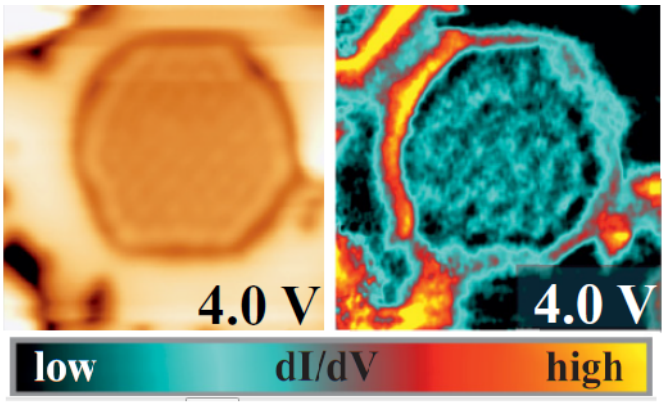


FIGURE 3.6: Topographic image and conductance map of an Au island on 25 ML CaO(001) [75]

it is possible to record laterally resolved dI/dV images at a certain voltage U_{bias} simultaneously with a constant-current topographic image. A series of images taken at different U_{bias} shows the change in conductance for different surface structures as seen in Fig. 3.6.

dz/dV constant current STS

With the feedback switched on during STS it is possible to access a larger energy range as long as the tunnel voltage is nonzero because it would inevitably result in a tip crash. The feedback will stabilize the tip at the chosen current by changing the tip-sample distance. The result is a distance-voltage-plot or a dz/dV spectrum. With voltages above the work function of the sample, even electronic states above the vacuum level become accessible.

The first theoretical description of high-bias spectra [76] found oscillations superimposed on the conductance. These can be explained by the large electron mean free path in vacuum and the reflection of electrons at the sample surface and the tunnel barrier. The results are standing electron waves that depend on the shape of the electronic potential inside the tunnel gap. The shape of the potential is controlled by the tip, the tip-induced electric field (slope of potential), the electron energy and the reflectance of the sample surface.

Coombs and Gimzewski [77] found resonances whenever the length of the electron path between sample surface and reflection point in vacuum equals half the electron wavelength times an integer, much like the well-known particle in a box behaviour as seen in Fig. 3.7 on the left hand side. The bias voltage at which the n-th state can be found is given by

$$U_n = \Phi + \alpha n^{2/3} E^{2/3} \tag{3.12}$$

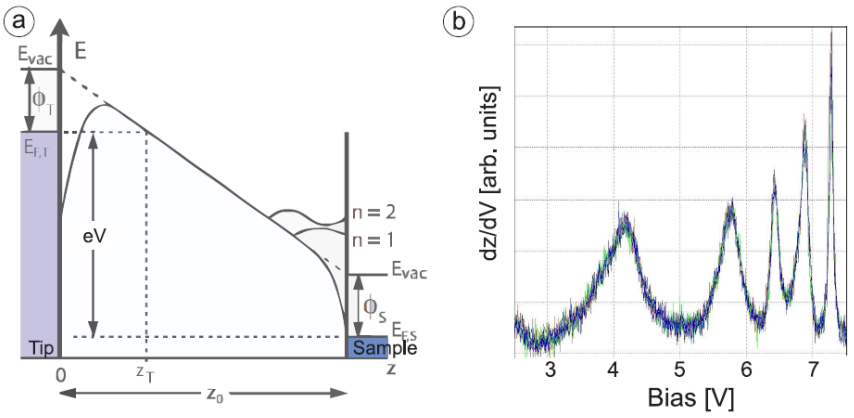


FIGURE 3.7: Field Emission Resonances caused by reflected electrons between tip and sample. [74]

with Φ the work function, a constant ($\alpha = 4,39V^{1/3}A^{2/3}$) and the field strength E measured in V/Å [74]. As the positions of the oscillations also depend on the work function, they can be used to calculate this quantity from from dz/dV spectroscopy, too. Such Field Emission Resonances (FER) [78, 79] can be detected with dz/dV spectroscopy as the the feedback stabilizes the tip at a constant current, leading to changes of the tip-sample distance whenever they occur as seen in Fig. 3.7 right hand side.

d^2I/dV^2 inelastic STM spectroscopy

The majority of the tunneling electrons cross the barrier without loosing energy in the process. This is considered elastic tunneling and makes up for the major part of the current. If the electron energy however is big enough to excite inelastic modes e.g. vibrations in an adsorbed molecule or collective electron excitations (plasmons) the electron will loose energy equal to the energy of the excitation.

Inelastic tunneling provides an additional channel for electron transport and will thus lead to a changing slope of the tunneling current at the threshold of the excitation $\hbar\omega = e \cdot U_{\text{bias}}$. This small onset in conductance yields a pronounced peak in d^2I/dV^2, as seen Fig. 3.8.

Typically the temperature-dependant peak broadening requires LT-STM which also contributes to a more stable tunnel current which in turn is beneficial for measurement of the small contribution of inelastic tunneling. Inelastic spectroscopy is performed as described earlier, with the open feedback loop and the bias voltage swept across the region of interest. With this spectroscopic method vibrations of single adsorbates [80] diffusive motion of molecules [81] but also optical excitation in the tunnel gap can be measured.

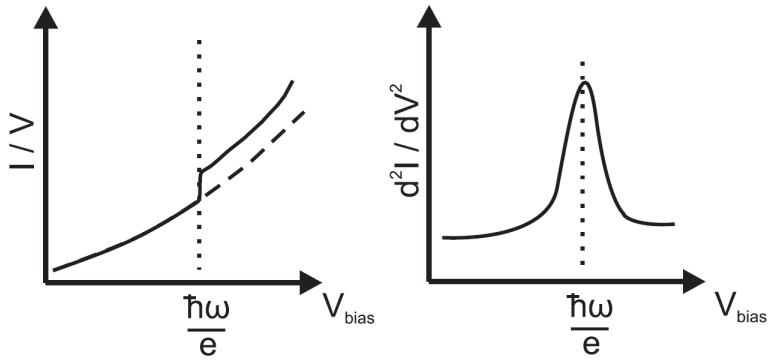


FIGURE 3.8: Inelastic tunneling electrons give a small contribution to the overall tunneling current. d^2I/dV^2 shows the Energy of the inelastic process. [74]

3.1.6 Surface States

One example for the application of STS is the investigation of surface states that are particularly accessible to STM due to their high surface localization. A bulk crystal can be described as a periodic potential created by the atomic cores. At a surface, the periodicity is broken and the potential changes to the vacuum value. For electrons in the crystal and at the surface different energy eigenvalues exist. These are calculated by solving the Schrödinger Equation [82]. Surface states are accessible for tunneling and will result in higher conductivity for electrons of matching energy thus resulting in additional peaks in dI/dV spectra.
There are two mathematical models to approach the physical nature of surface states: The nearly free electron approximation and the tight binding approach.

Shockley Surface States

In the first model the electrons in the crystal are assumed to be a nearly free electron gas. This model was first described by Shockley in 1939 [83] and is best suitable for metals and narrow gap semi-conductors.
For a metal the potential can be described as a periodic function with a step function at the surface as seen in Fig. 3.9:

$$V(z) = P\delta(z + la) \qquad \text{for z} < 0 \tag{3.13}$$

$$V(z) = V_0 \qquad \text{for z} > 0 \tag{3.14}$$

with a periodicity of the crystal, l an integer and P a normalization factor. The solution to the one dimensional one-electron Schrödinger equation

$$-\left[\frac{\hbar^2}{2m}\frac{\delta^2}{\delta z^2} + V(z)\right]\psi(z) = E \cdot \psi(z) \tag{3.15}$$

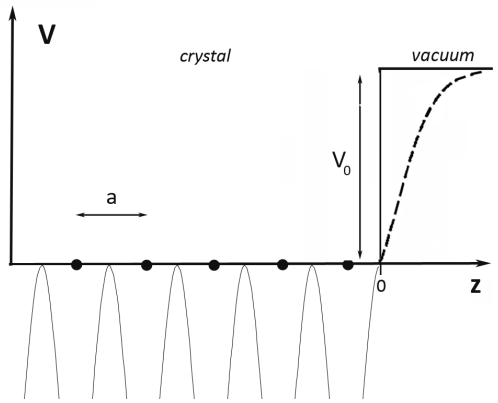


FIGURE 3.9: Periodic potential created by atomic cores with a step function at the surface. The dashed line is a more realistic form of the potential than the step function. [84]

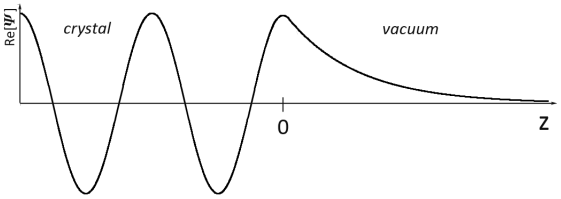


FIGURE 3.10: Electronic states are Bloch waves within the crystal that exponentially decay into the vacuum at the surface. [84]

are the electronic waves shown in Fig. 3.10

$$\psi(x) = Bu_{-k}e^{-ikz} + Cu_k e^{ikz} \qquad \text{for z} < 0 \tag{3.16}$$

$$\psi(x) = A\ e^{-\sqrt{2m(V_0-E)}z/\hbar} \qquad \text{for z} > 0 \tag{3.17}$$

For $z \leq 0$, within the bulk crystal the electronic waves are a linear combination of two Bloch waves, one incoming from the crystal and another reflected at the surface. Above the surface the electronic waves decay exponentially into the vacuum. This results in a number of electrons situated just above the surface with holes left behind in the crystal. The resulting dipole layer leads to a change of the metal's work function.

Modelling the periodic potential with a cosine potential results in the picture shown in Fig. 3.11. At the Brioullin zone boundary $k = \pm\pi/a$ Bragg reflection occurs resulting in standing waves. These lead to band splitting and a band gap of V being proportional to the amplitude of the periodic oscillations. Within the bands electronic states equivalent to those in metals exist. Within the bulk crystal they are described as periodic Bloch waves which decay exponentially into the vacuum at the surface (Fig. 3.10). Within the band gap no electronic states for the bulk crystal are allowed. However, at the surface states within the band gap are found which decay both into the bulk and into the vacuum as seen in Fig. 3.12. Typical examples for Shockley surface states are the free-electron like states residing at the surface of noble metal (111) surfaces.

Tamm Surface States

In the second model the electronic states are modelled as a linear combination of atomic orbitals (LCAO) also called the tight binding approach. This model was first shown

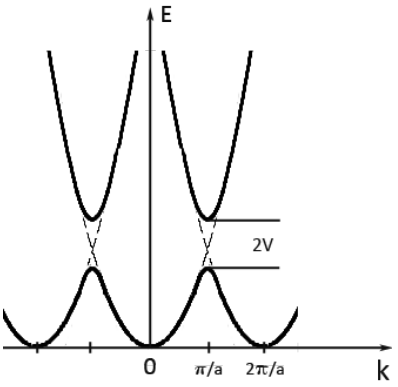


FIGURE 3.11: Bragg reflection at the brillouin zone boundary ($\pm\pi/2$) creates a band gap. [84]

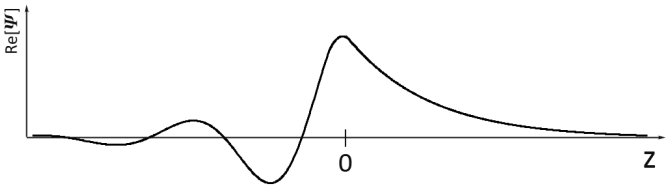


FIGURE 3.12: Electronic states with energies inside the band gap can exist at the surface but decay exponentially into the bulk and the vacuum. [84]

by Tamm in 1932 [85] and is better suited for transition metals and wide gap semiconductors. The atoms at the surface are missing binding partners which results in a shift in energy for their electron orbitals. Also if orbitals responsible for bindings in the bulk are broken at the surface they result in so called dangling bonds with the unfilled orbitals sticking out of the surface.

Extrinsic Surface States

Additionally to the intrinsic surface states described before, there are also extrinsic surface states resulting e.g. form defects or adsorbates which break the translational symmetry of the surface. Also there are a different states at the interfaces between materials and at the interface between a crystal and a surrounding gas or liquid phase.

3.2 X-Ray Photoelectron Spectroscopy

3.2.1 Introduction

In 1954 Kai Siegbahn recorded the X-ray photoelectron spectrum of sodium chloride (NaCl) [86]. He dubbed the new technique ESCA (electron spectroscopy for chemical analysis) to emphasize that it is not only capable of showing the elemental composition of a sample but also the chemical states the elements are in. In 1981 he received the Nobel Prize acknowledging his extensive efforts to develop XPS into a useful analytical tool.

In modern physics XPS is used routinely to analyse the chemical composition of anorganic compounds, metal alloys, semiconductors, catalysts, and many others [63, 87–89]. Because of the ionization charge compensation has to be considered for non-conducting samples. Usually XPS is executed in UHV conditions limiting its use to solid samples.

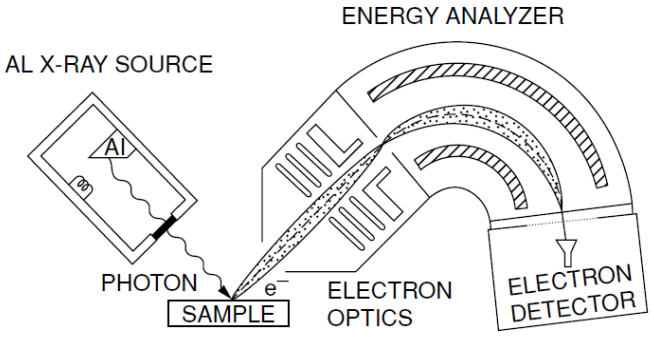


FIGURE 3.13: XPS Setup: An X-ray beam hits the target thereby emitting electrons which are collected by electrostatic lenses. The analyser only admits electrons of a certain energy range to the detector. [91]

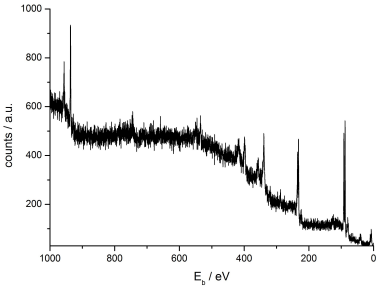


FIGURE 3.14: XPS survey spectrum of a gold sample showing the binding energy on the abscissa. Typical peaks are seen at ≈90 eV (Au 4f), ≈350 eV (Au 4d) and ≈550 eV (Au 4p). [92]

However there are ambient and near-ambient pressure setups that work in pressures of up to a few mbars, extending XPS analysis to fluids and gasses [63, 90].

XP-Spectroscopy analyses the electrons emitted by the sample when exposed to X-ray radiation. The kinetic energy of the collected electrons is specific for the electronic configuration of the sample atom. The electron mean free path determines the maximum escape depth of electrons from the sample. The electron mean free path can be determined from the universal curve shown in Fig. 3.15. It depends on the electron's kinetic energy but hardly on the element it passes through. Thus XPS is not only sensitive to the surface layer but provides information about the top few nm of the sample.

For lab use non-monochromatic Mg-kα and Al-kα X-ray sources are most common. These produce kα X-rays by bombarding an Al or Mg target with electrons. The two main transitions from 2p 3/2 and 2p 1/2 initial states to the 1s final state produce the kα_1 and kα_2 radiation. For soft X-rays in the order of 1 keV as discussed here the continuous spectrum originating from bremsstrahlung is hardly noticeable. The kα has a FWHM of about 1 eV for Al and 0.8 eV for Mg [91]. To achieve a better resolution in XPS a monochromator for the X-rays has to be used. These generally make use of diffraction to select a specific energy from the X-rays. Also synchrotron beam lines can be used which produce very stable monochromatic X-ray beams.
The intrinsic line width of an XPS line depends on the hole state lifetime according to the uncertainty principle. It can be calculated as

$$\Delta E = h/\tau \tag{3.18}$$

with h the Plank constant and τ the lifetime. Typical lifetimes of 10^{-14} s result in line widths of 0.4 eV [93].

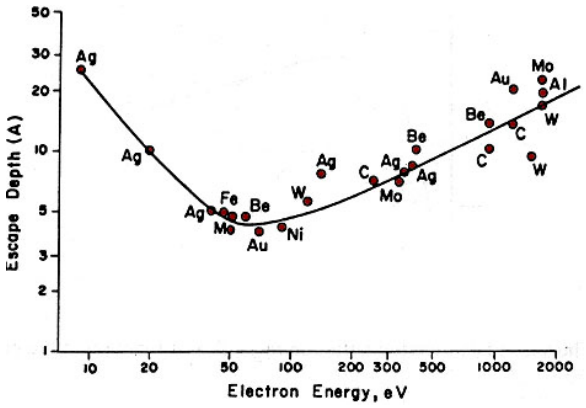


FIGURE 3.15: Electron escape depth for different elements depending on universal electron mean free path. [94]

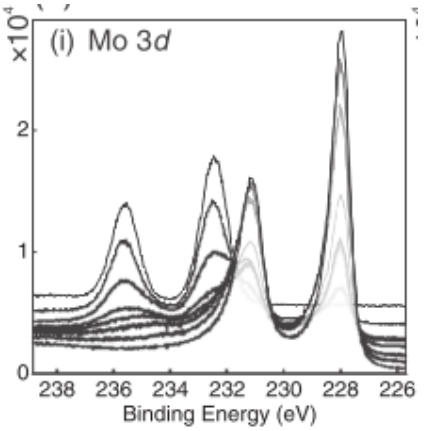


FIGURE 3.16: Mo 3d XP-spectrum showing a doublet structure (3/2 and 5/2) due to spin-orbit-splitting as well as chemical shift for different oxidation states between Mo^0 at 228 eV + 231 eV and MoO_3 at 233 eV + 235 eV. [95]

Detection area for non-monochromatic sources is in the range of $(10-30)\,mm^2$ depending on the employed X-ray source. A hemispherical analyser with a set of electrostatic lenses is used to separate electrons of different kinetic energies. A potential is applied to the two concentric plates such that the electrons travel along equipotential lines to reach the electron detector. The energy range of electrons that will reach the detector is proportional the pass energy E. A smaller pass energy will result in a better resolution but somewhat smaller overall intensities.
The resulting XP-spectrum as seen in Fig. 3.16 shows the number of electrons collected versus the electron binding energy which can be calculated from the measured kinetic energy and the known energy of the X-ray photons.

The easiest accessible information obtained from XPS is the elemental composition of the sample. Each element shows a number of peaks at specific energies depending on its unique electron configuration and can thus be easily identified. A vast number of electron binding energies can be found in online databases such as NIST X-ray Photoelectron Spectroscopy Database [96].
A chemical bond creates a spatial redistribution of valence electrons which creates a slight shift in energy levels of the core electrons. This shift can be detected by XPS and is commonly referred to as "chemical shift". Thus a metal and its oxide will be distinguishable by a small shift in XPS peak energies. The same holds for a variety of processes that cause electron binding energies to shift, e.g. surfaces, interfaces, alloying and the local chemical and physical environment [95, 97–100]. For some elements the shifts will be rather small, making interpretation of XPS spectra more difficult. Additional difficulties arise from the nature of XPS as a multi-electron process. Each XPS

peak is actually a convolution of many possible electron transitions that are happening while the atom is excited with X-ray radiation. That is why detailed XPS analysis relies on extensive software to fit the measured results.

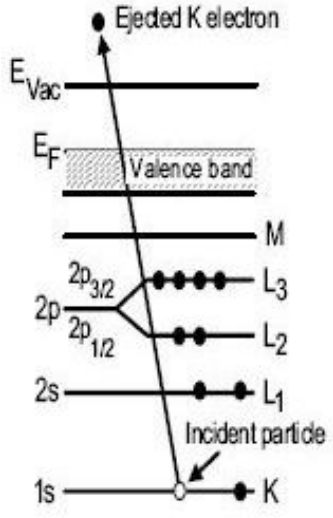
3.2.2 Theory

Calculations of the transition probabilities involved in a XP-Spectrum is of ongoing interest to theoretical physicists and not resolved until today [101–103].

The basic process behind XPS is the photoelectric effect. Part of the photon's energy is used to overcome the electron's binding energy while the remaining energy will be transferred to the electron's kinetic energy. A schematic view of the process can be seen in Fig. 3.17.

$$E_{\text{kin}} = E_{\text{photon}} - E_{\text{bind}} \tag{3.19}$$

The respective XPS lines are denoted by the element and electronic state (quantum numbers) the electron comes from, i.e. Au 4f, O 1s, Mo 3d as listed in Fig. 3.17. Because of spin-orbit-coupling those XPS lines with $l \neq 0$ are split up into doublets, like Mo 3d 5/2 and Mo 3d 3/2 as seen in Fig. 3.16, with the intensities reflecting the number of electrons with each spin. The kinetic energy cannot be calculated from the eigenvalue of the respective orbital in an atom with all electrons still present (initial state calculation). There are a number of possible effects that change the kinetic energy with which



Quantum Numbers			Level Symbol	Auger Notation	XPS Notation
n	ℓ	j			
1	0	1/2	$^2S_{½}$	K	$1s_{1/2}$
2	0	1/2	$^2S_{½}$	L_1	$2s_{1/2}$
2	1	1/2	$^2P_{½}$	L_2	$2p_{1/2}$
2	1	3/2	$^2P_{3/2}$	L_3	$2p_{3/2}$
3	0	1/2	$^2S_{½}$	M_1	$3s_{1/2}$
3	1	1/2	$^2P_{½}$	M_2	$3p_{1/2}$
3	1	3/2	$^2P_{3/2}$	M_3	$3p_{3/2}$
3	2	3/2	$^2D_{3/2}$	M_4	$3d_{3/2}$
3	2	5/2	$^2D_{5/2}$	M_5	$3d_{5/2}$

FIGURE 3.17: Schematic view of the basic photoelectric effect used in XPS and respective quantum numbers, electron levels, Auger and XPS notation. [104]

the electron leaves the atom and again some effects that can change the kinetic energy until it leaves the sample.

The energy the electron carries when leaving the atom is the difference of the total energy of the atom in its final state and the total energy of the atom in its initial state $E_f - E_i$. The created core hole will result in a readjustment of the outer electrons, thereby lowering the final state energy. This will result in a higher kinetic energy as would be calculated from an initial state calculation [91].
Additionally there is a finite probability that the final state ion is left in a specific excited state above the ground state after the electron is emitted. The energy necessary for this excitation results in less kinetic energy of the photoelectron. This will lead to so called "shake up" peaks on the high binding energy side as found for example in Cu 2p for CuO see Fig. 3.20. The presence or absence of shake-up structures can help in the assignment of chemical states [97] especially if the main peak is otherwise nearly identical as in Cu^0, Cu^+ and Cu^{2+}.
For metals with accessible states close to the Fermi level these "shake ups" can occur at very low energies basically exciting a valence electron. The measured kinetic energy of the photoelectron will only be slightly smaller resulting in an asymmetry of the peak shape with a broader side on the high binding energy side. This effect is more pronounced in elements with a significant density of occupied states at the Fermi level such as Pt whereas Au shows a symmetric peak shape because of the much lower density of states at the Fermi level.

Upon leaving the sample the electron "sees" the difference in work function between the sample and the spectrometer. For conducting samples in contact with the spectrometer the Fermi energies are at the same level. This leaves a difference of $\Phi_{spec} - \Phi_{sample}$ that the electron looses from its initial kinetic energy as seen from Fig. 3.18. The binding energy is thus:

$$E_{\text{bind}} = E_{\text{photon}} - E_{\text{kin}} - \Phi_{\text{spec}} \tag{3.20}$$

For non-conducting samples the position of the Fermi energy within the band gap is uncertain. Moreover sample charging will result in shifts of measured kinetic energy making the interpretation of XPS from insulating and wide gap semi conductors more difficult. Referencing to a known spectral line is common practise in this case. Photoelectrons excited below the surface of the sample will likely undergo inelastic scattering on their way out resulting in a background at the high binding energy side.

Quantitative Analysis
For quantitative analysis the line intensities, or better the peak areas are of interest. The

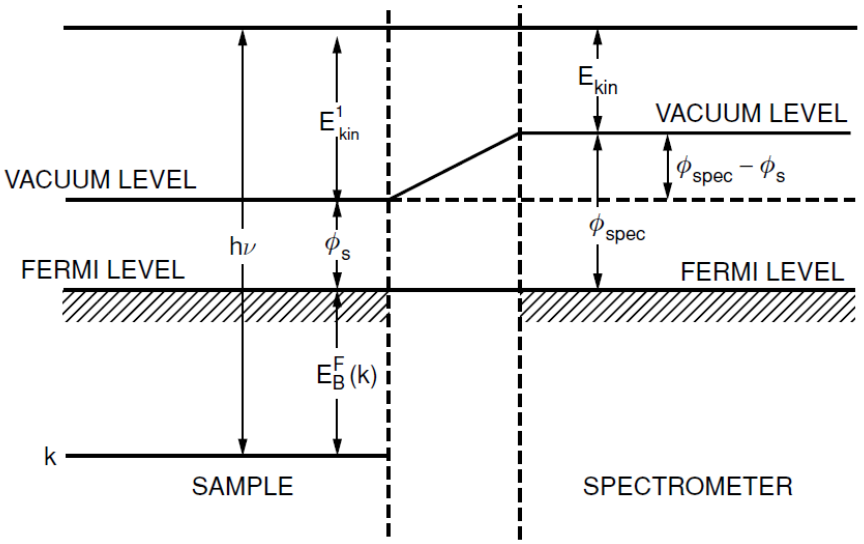


FIGURE 3.18: Difference in measured kinetic energy E_{kin} and initial kinetic energy E^1_{kin} due to the spectrometer work function Φ_{spec}. [91]

intensity depends on different factors, such as the electron escape depth, the spectrometer transmission, the photoelectric cross section (depending on the sample) as well as surface roughness or inhomogeneities and eventually the presence of satellite structures which will result in a decrease of the main peak. The flux of photons is unattenuated over the depth from which photoelectrons can escape. The photoelectric cross section depends on the element and the XPS line which is measured. It has been calculated for various elements by Scofield in 1976 [105] and is shown in Fig. 3.19.
The possibility to produce a detectable photoelectron from $1\,\mathrm{cm}^2$ of sample surface is than calculated by

$$P = \sigma N \lambda \tag{3.21}$$

with σ the photoelectric cross section, N the number of atoms per $1\,\mathrm{cm}^2$ and λ the electron escape depth. Usually the ratio of two elements A and B is of interest. If the two peaks are close in energy, the mean free path cancels out and the ratio can be calculated as

$$\frac{n_{\mathrm{A}}}{n_{\mathrm{B}}} = \frac{I_{\mathrm{A}}\sigma_{\mathrm{B}}}{I_{\mathrm{B}}\sigma_{\mathrm{A}}} \tag{3.22}$$

with n the ratio of the element and I the measured intensity. Detection of up to 0.01% in bulk samples and 0.01 ML of surface contamination can be achieved.

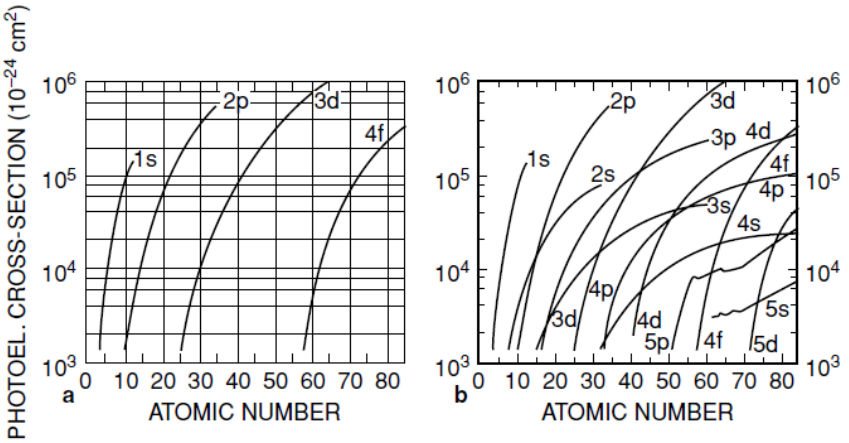


FIGURE 3.19: Photoelectric cross section at an incident radiation of 1.5keV for various elements and electronic sub-shells [91].

Inelastic Background

As mentioned previously, inelastic scattering of the electrons will result in an energy background on the high binding energy side. To calculate the background intensity at energy E all electrons with kinetic energies $E' < E$ (i.e. higher apparent binding energies) are relevant. The primary excitation spectrum *F(E)* is then given by subtracting the background intensity *I(E)* from the measured electron flux *j(E)*.

$$F(E) = j(E) - I(E) \tag{3.23}$$

There are different methods of calculating and subtracting the background see Fig. 3.21. The easiest is the linear or horizontal background more sophisticated methods are Shirley [106] and Tougaard [107, 108]. For more in depth theoretical description see [106, 109, 110].

In the case of a Shirley background two points A and B on the two sides of the XP-peak (A $\leq E \leq$ B) are chosen to have no background intensity: I(A) = I(B) = 0 All background intensities in between are fitted in a way that

$$I(E) \propto \int_{\mathrm{B}}^{E} j(E')dE' \tag{3.24}$$

So the background energy depends only on the number of electrons measured at higher kinetic energies.

The Tougaard background is calculated using the electron mean free path $\lambda(E)$ and the probability $k(E', E' - E)$ that an electron with starting energy E' looses the energy *E'-E* (thus it is detected at energy E) while travelling one unit length [106].

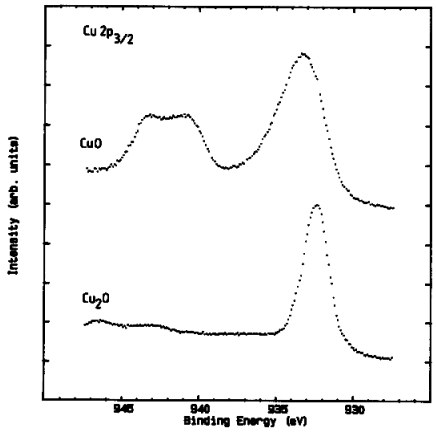


FIGURE 3.20: Shake-up peak in CuO on the high binding energy side of Cu 2p 3/2. No shake-up peaks occur in Cu_2O. [97]

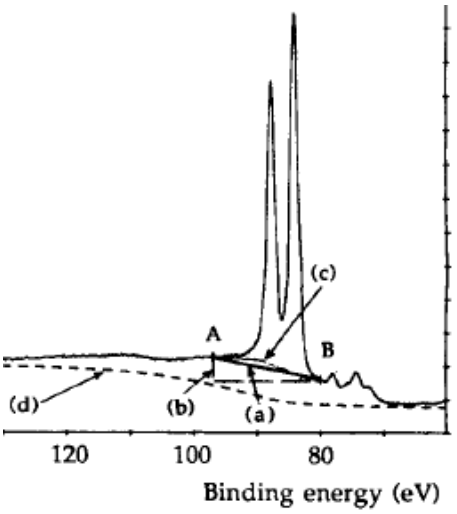


FIGURE 3.21: Different Backgrounds as compared by Repoux
: (a) linear, (b) horizontal and (c) Shirley background all work between user-chosen point A and B whereas (d) the Tougaard Background needs a larger energy range. [106]

$$I(E) = \lambda(E) \int_{\infty}^{E} k(E', E' - E) j(E') dE' \tag{3.25}$$

Because the electron mean free paths depends on the amount of energy lost while travelling one unit length the product of λk is independent of E and can be written by the universal function with $T = E' - E$

$$\lambda(E) k(E, T) \approx \frac{BT}{(C + T)^2} \tag{3.26}$$

with $B \approx 2886\, eV^2$ and $C \approx 1643\, eV^2$ and thus

$$I(E) = \frac{BT}{(C + T)^2} \int_{\infty}^{E} j(E') dE' \tag{3.27}$$

Because no points with $I(\mathrm{A})=I(\mathrm{B})=0$ are chosen the background will extend up to 100 eV below the peak. This of course means that data in a wider energy range has to be collected which increases measuring times. Comparison of the different methods [106] shows the Tougaard background to be the most accurate but Shirley background is the most widely used because it features the best mix of accuracy and ease of use.

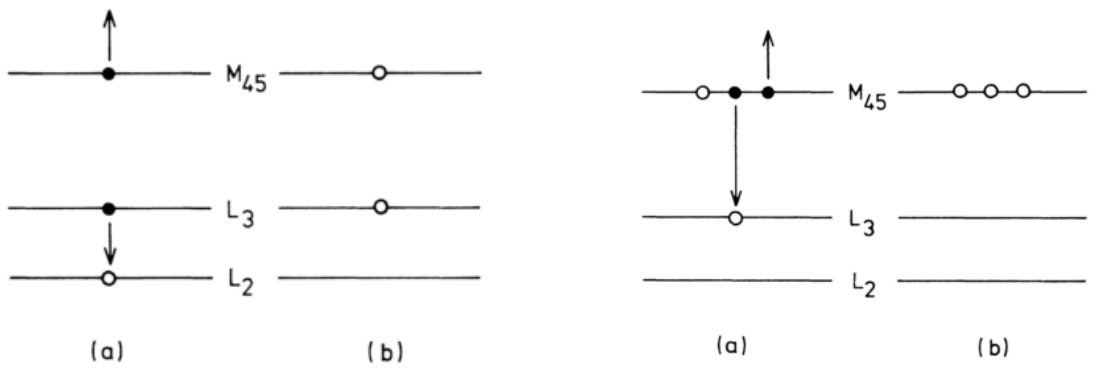


FIGURE 3.22: Coster-Kronig process (left) followed by Auger process (right). In the Coster-Kronig process an electron from the L_3 shell fills the hole left by the primary electron. With the freed energy an electron from $M_{4,5}$ shell is ejected. There are now two holes in the electron configuration. In a subsequent Auger Process the L_3 hole is filled by an electron from the $M_{4,5}$ shell simultaneously emitting another electron from the $M_{4,5}$ shell, leaving the atom with three holes in the valence band. [112]

Auger Processes

If the core hole left by the photo-ionization is filled up by an electron from a higher electron shell, the freed-up energy difference can emit a second electron from the atom. This is the main deexcitation process for elements $Z \leq 35$ and called Auger process [111]. The emitted electron has a kinetic energy that only depends on the energy difference between the electron shells, not on the energy of the X-ray photon.

With the energies of the L- and M-shell, E_L and E_M respectively, the energy gained by filling the L-shell hole with an electron from the M-shell is $E_\mathrm{L} - E_\mathrm{M}$. To eject a second electron from the M-shell, the energy E_M is needed. Thus Auger lines will always be at the kinetic energy

$$E_\mathrm{kin} = E_\mathrm{L} - E_\mathrm{M} - E_\mathrm{M} \tag{3.28}$$

and not shift if another X-ray source is used.

Notation for Auger lines gives the three electron shells involved in the process. So LMM means a core hole in the L-shell is filled by an electron from the M-shell and another electron of the same shell is subsequently emitted. L and M denote the electronic shell (main quantum number) see Fig. 3.17. Because there are a number of equivalent pairs of electrons for one Auger line calculating the transition rates is much more difficult. The large number of available final states makes Auger lines in general broader than XPS lines.

The processes changing the final state discussed before for photoelectron lines hold for Auger lines as well. Relaxation of the ion with two holes will change the final state

levels thereby changing the kinetic energy of the ejected electron. Chemical shift occurs in Auger lines as well, although the inner electron shells shift about the same amount, so their energy difference stays the same. But as two electrons from the same shell are involved chemical shift is also evident in Auger lines. However it is more difficult to interpret as coming from a two-electron process.
Of course inelastic scattering will also produce a background from Auger lines.

Coster-Kronig Processes

If the core hole is filled by an electron from the same shell, but higher sub-shell this is called a Coster-Kronig process [113]. Like the Auger process it will emit a second electron and leave two holes. For this process to occur the energy difference between L_3 and L_2 (due to spin-orbit-coupling) has to be bigger than the energy of the $M_{4,5}$-shell, see Fig. 3.22. This is fulfilled for some elements like Cu and Zn but not for others like Ga and Ge [112]. The Coster-Kronig transition has usually much higher transition rates than the Auger transition because transitions within different sub-shells (L_2 to L_1) are very fast. This inhibits the L_1 vacancy to be filled by an electron from the M shell thus reducing the intensity of the Auger line. However the Coster-Kronig process can itself be followed by an Auger process resulting in an electron of slightly smaller kinetic energy than of the main Auger line ($L_3M_{4,5}M_{4,5}$ instead of $L_2M_{4,5}M_{4,5}$) and triple ionization of the atom. (Fig. 3.22 on the right-hand side.)
Because the energy difference between the two sub-shells is still small the emitted electron will have hardly any kinetic energy. The $L_2L_3M_{4,5}$ process is shown in Fig. 3.22 on the left-hand side.

3.2.3 Applications

Peak Fitting

To assess the area of a measured XPS line and for deconvolution of overlapping lines a fit of the peak shape is necessary. The natural line shape as generated by the hole state lifetime is a Lorentzian. However due to atomic vibrations at finite temperatures as well as the instrumental work function a Gaussian broadening is imposed on the XPS peak shape. For most symmetric peak shapes a mixed Gaussian-Lorentzian fit can be used.
On the other hand in conductors line shapes tend to be asymmetric. This is due to the excitation of valence electrons which will lead to a small loss in kinetic energy of the photoelectron. Thus the line shape is skewed to the higher binding energy side. In the case of an asymmetric peak shape a Doniach Sunjic [114] fit is better suited. However the asymmetry factor has to be chosen with care as it depends on the average density of states of electrons and holes around the Fermi energy which will change e.g. by alloy formation.

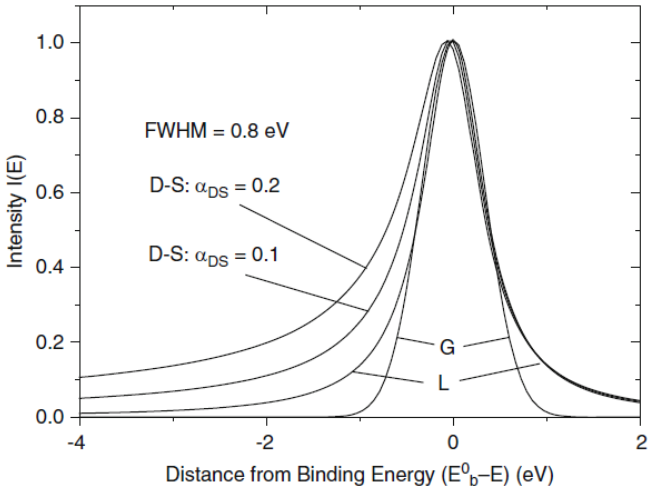


FIGURE 3.23: Gaussian (G), Lorentzian (L) and two Doniach-Sunjic (D-S) line shapes with different asymmetry factors α_{DS}. [93]

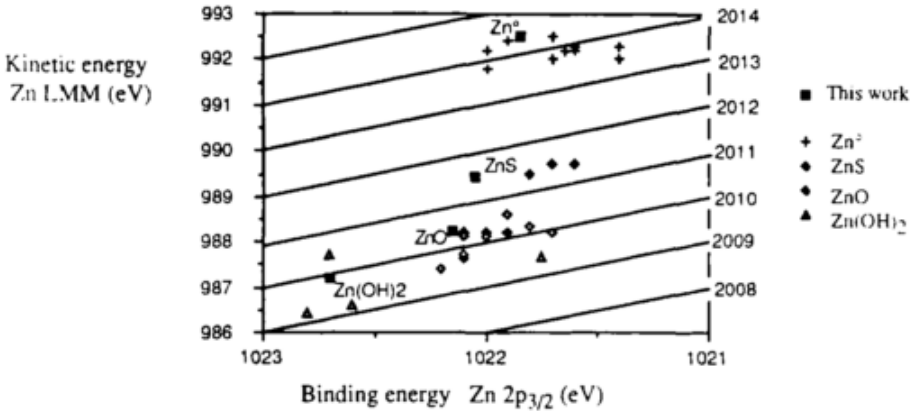


FIGURE 3.24: Wagner plot for the zinc compounds showing the $L_3M_{4,5}M_{4,5}$ kinetic energy versus the 2p 2/3 binding energy. Different chemical configurations are easily distinguished. [99]

The differences in line shapes are shown in Fig. 3.23. Generally the G-L shape is better used for insulators, semiconductors and metals with low electron state densities around the Fermi level whereas D-S is better suited for metals with a high electron state density around the Fermi edge [93].

Wagner plot and Modified Auger Parameter

In some cases it is useful to look at Auger lines in conjunction with XPS lines [115]. A Wagner plot shows the position of the strongest XPS line Zn 2p 2/3 in Fig. 3.24) versus the strongest Auger line ($L_3M_{4,5}M_{4,5}$). Measurements for the same chemical state of a compound will group together and can be easily distinguished. This is especially helpful if the element shows little to no chemical shift in the XPS line for example for Cu and Cu_2O or Zn and ZnO (see Fig. 3.24).

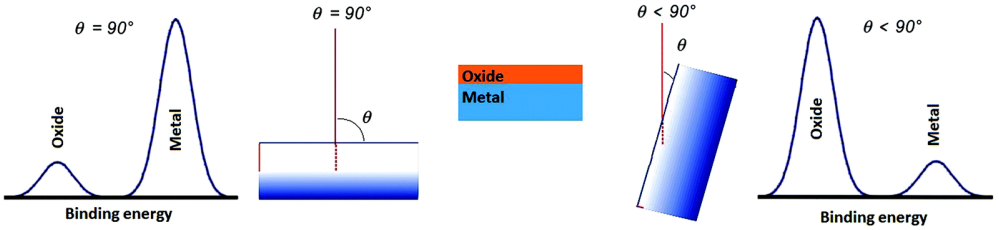


FIGURE 3.25: Angle resolved XPS showing the change in relative intensities of thin film and substrate with changing emission angle. [117]

The diagonal lines in Fig. 3.24 show the modified Auger parameter *a'* [98, 116]. This is calculated using the binding energy of the XPS-line and the kinetic energy of the Auger-line. Any shift due to charging will be cancelled in the modified Auger parameter.

$$a' = E_{\text{kin}}(\text{Auger}) - \text{E}_{\text{bind}}(\text{XPS}) \tag{3.29}$$

Film Thickness

The thickness of a thin film can be determined by looking at the intensity of XPS lines from the substrate. According to Beer-Lambert's Law the intensity of the substrate XPS line gets attenuated with increasing film thickness while the intensity from the film will increase. Using an exponential attenuation model the film thickness can be calculated as follows [22]:

$$d = \ln\left(\frac{I}{I_0}\right) \cdot \lambda \cdot \cos(\Theta) \tag{3.30}$$

Here I_0 is the clean substrate intensity, I the intensity of the substrate covered with a film of thickness d, Θ the take-off angle of electrons from the sample and λ the mean free path of an electron calculated from the universal curve (shown in Fig. 3.15). The latter can be approximated with:

$$\lambda = \frac{143}{E^2} + 0.054 \cdot \sqrt{E} \tag{3.31}$$

By changing the take-off angle Θ the minimum length an electron from the substrate has to travel through the film before emission will be changed. This is used to measure film thickness and distribution of elements with respect to the surface in angle-resolved XPS.

When depositing films thicker than one mono-layer the lower layers will start to be attenuated resulting in a change in slope for the calculated film thickness as seen in

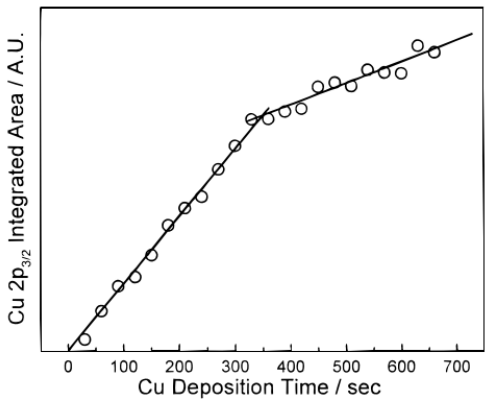


FIGURE 3.26: With longer deposition times, the films thickness grows and XP intensities increase. At the completion of 1 ML the 2nd layer starts to attenuate the signal from the first, resulting in a slower rise in XP intensities. [100]

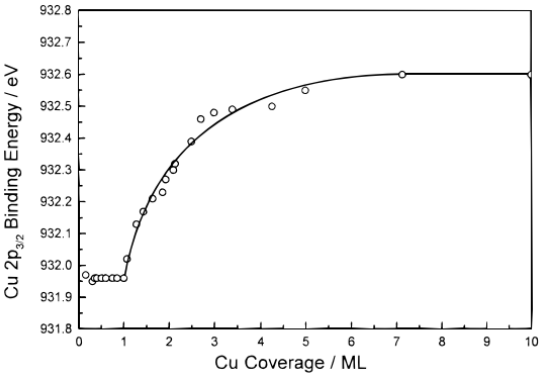


FIGURE 3.27: Sub mono-layer films show binding energies different than the bulk values due to the relatively higher interface and surface contributions. With increasing film thickness the surface and interface contributions get attenuated and the binding energy shifts towards the bulk value. [100]

Fig. 3.26. The shape of the kink can yield information about the growth mode (islands or layer-by-layer) of the film. Respective shifts in binding energies can also be measured for increasing film thickness as shown in Fig. 3.27 for copper thin films on a palladium substrate [100].

3.3 Low Energy Electron Diffraction

3.3.1 Introduction

In 1924 de Broglie predicted the existence of electron waves [118] which were three years later found by Davisson and Germer [119] by deflecting low energy electrons at a nickel target and observing a diffraction pattern. Development of low energy electron diffraction as a wide spread technique in surface analysis only started in the 1960s when vacuum techniques and detection methods had improved.

LEED uses low energy (20-200 eV) electrons which are elastically back-scattered from the surface of a single-crystalline material. The spot positions in the resulting diffraction pattern (see Fig. 3.29) yield information about the symmetry of the surface structure. In the presence of adsorbates the size and rotational domain with respect to the substrate unit cell can be determined.

Exact position of the adsorbate structure in real space can't be determined. Moving the whole adsorbate structure e.g. form top to bridge positions but without changing the overall arrangement, won't change the resulting LEED pattern. Single defects or impurities which do not change the basic symmetry of the surface cannot be detected

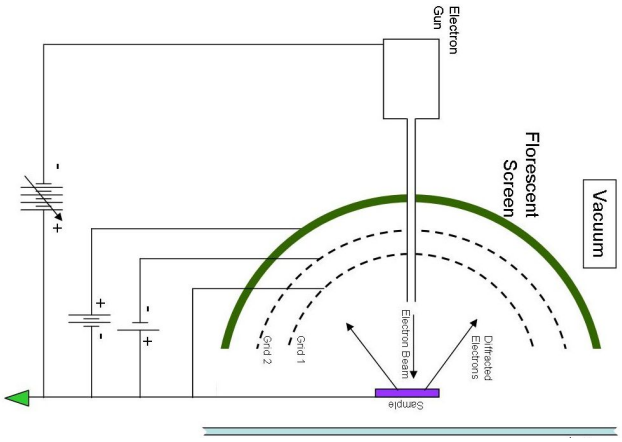


FIGURE 3.28: Schematic LEED Setup. The Diffraction pattern on the fluorescent screen can be seen through the view port. [120]

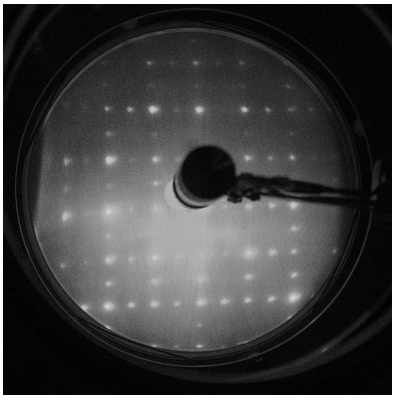


FIGURE 3.29: LEED pattern of a Si(100) reconstructed surface. [120]

at all.

A schematic LEED setup is shown in Fig. 3.28. The filament in the electron gun generates an electron beam of about 0.1 to 0.5 mm spot size that is accelerated towards the sample by 10-600 V. The reflected electrons are accelerated towards the fluorescent screen where they produce the characteristic spots. In front of the screen are usually two to four hemispherical grids to slow down the electrons and to sort out electrons which have undergone inelastic scattering.

The electron mean free path depends on the electron energy as discussed in section 3.2.1. For the usual energies LEED is sensitive to the top 1-2 nm of the sample.

3.3.2 Theory

In single scattering theory each electron is deflected once from the surface. According to de Broglie the wavelength of an electron with energy E is $\lambda = \frac{h}{\sqrt{2mE}}$. The respective wave vector in reciprocal space is given by

$$k = \frac{2\pi}{\lambda} \tag{3.32}$$

Constructive interference and hence a spot in the diffraction pattern can be calculated using the Laue Condition [121]

$$k - k_0 = G_{hk} = ha^* + kb^* \tag{3.33}$$

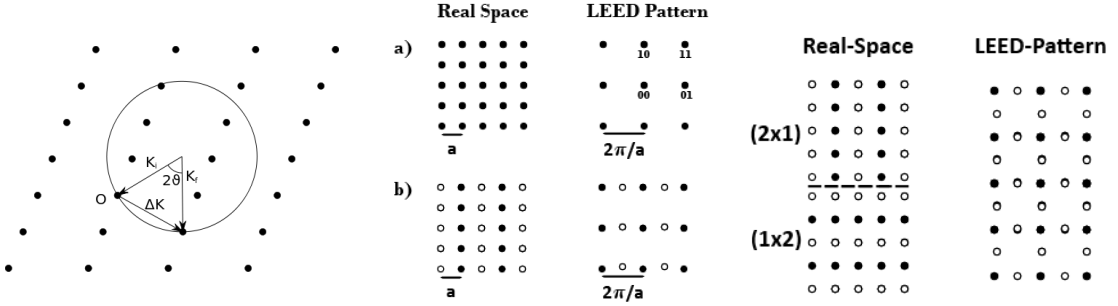


FIGURE 3.30: Left: Ewald-sphere with incident wave vector k_i and diffracted wave vector k_f [123]. Centre and right: Atomic surface structures in real space and resulting LEED pattern in reziprocal space. [120]

Here k and k_0 are the incident and scattered wave vectors with $|k| = |k_0|$ because only elastic scattering is considered. G_{hk} is a vector in reciprocal space with a^*, b^* being the primitive translation vectors of the 2D reciprocal lattice and h, k integers. The condition is best visualised using the Ewald sphere [122], see Fig. 3.30 left side.

The pattern observed in LEED is a direct image of the surface structure in reciprocal space. A square lattice with lattice constant a will show a square lattice with lattice constant $\frac{2\pi}{a}$ in reciprocal space as shown in Fig. 3.30 on the top left side. A structure of adsorbates on symmetric sites of the surface will lead to extra spots in the LEED image shown on the bottom left side of the same figure.

Because the electron beam spot size is about $1\,\mathrm{mm}^2$, diffraction from several domains on the surface can contribute to the LEED pattern. The coherence length of the electron waves however is only about (10-20) nm. Waves with a path difference beyond the coherence length cannot interfere. If domains are larger than the coherence length two electrons from different domains will not interfere instead leading to a superposition of all superstructures as shown in Fig. 3.30 on the right-hand side for two domains of rotational symmetry.
In this thesis, LEED has been used to check the quality of the single crystals used as substrates for film growth. Moreover, LEED provided a first insight into the nature and long range order of ultra thin oxide films directly after preparation.

3.4 Gibbs-Curie-Wulff Theorem

When a material (metal, oxide) is dosed onto a surface it can grow in a layer-by-layer fashion or it form into small particles. Which of the two possibilities is realized depends on the surface free energies of the two materials and the interface energy between them.

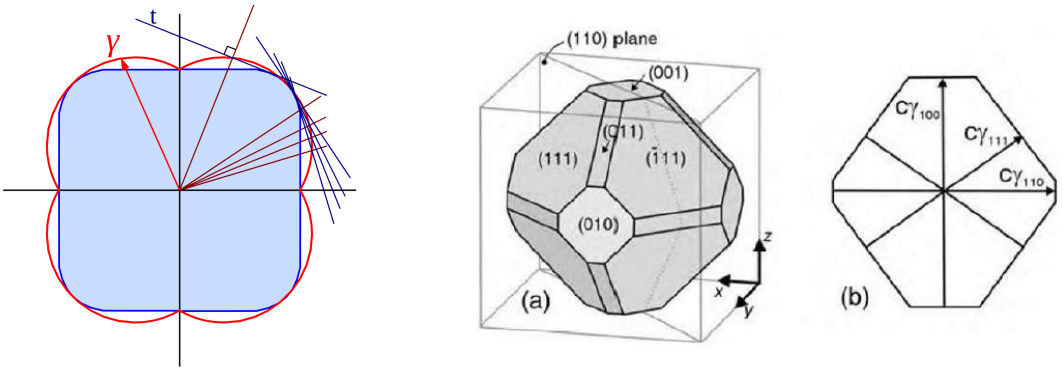


FIGURE 3.31: Shape of an unsupported particle derived from surface free energy (Wulff construction) left [125], right [126]

The system will try to minimize the overall free energy, so the metal will grow in a layer-by-layer fashion if the ad-material's energy γ_{ad} plus the interface energy γ_{int} is smaller than that of the support γ_{sup}. If the surface free energy of the support is already lower three dimensional growth of the ad-material will prevail in order to keep the overall energy low.

$$\gamma_{\text{ad}} + \gamma_{\text{int}} < \gamma_{\text{sup}} \quad \text{layer} - \text{by} - \text{layer growth} \tag{3.34}$$

$$\gamma_{\text{ad}} + \gamma_{\text{int}} > \gamma_{\text{sup}} \quad \text{particle growth} \tag{3.35}$$

In the case of particle growths the shape will again be determined by the the surface free energies of the particles facets. In equilibrium the particle will take a form that minimizes the overall surface free energy times the surface area. The Wulff Theorem [124] thus states that the distances of a facet from a central point within the crystal (Wulff-point) corresponds to the specific surface free energy of this facet:

$$d_i/\gamma_i = \text{constant} \tag{3.36}$$

The shape of the crystal can be determined by the intersections of the lowest surface energies for each direction from the Wulff-point as seen in Fig. 3.31 known as Wulff-Construction.

In the case of a supported nano-particle the interface energy has to be considered as well. This is made up of the two surface energies and the work of adhesion which are connected by the Dupre equation:

$$\gamma_{\text{int}} = \gamma_{\text{ad}} + \gamma_{\text{sup}} + W_{\text{adh}} \tag{3.37}$$

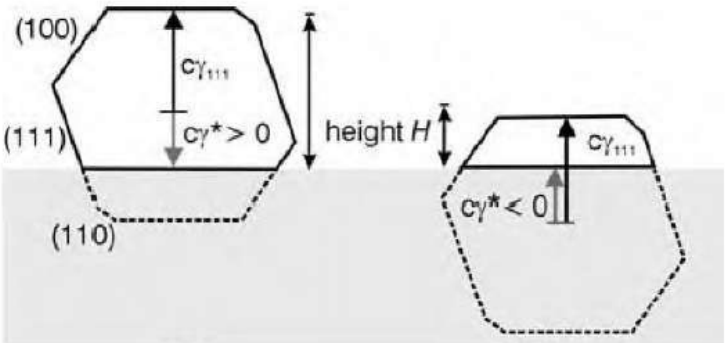


FIGURE 3.32: Shapes of supported particles [126]

For the shape of the supported nano-particle the modified Wulff construction can be used in which the surface free energy of the supported facet is replaced by an effective energy which is the difference between interface energy and the surface free energy in the unsupported case.

$$\gamma^* = \gamma_{\text{int}} + \gamma_{\text{ox}} = \gamma_{\text{sup}} - W_{\text{adh}} \tag{3.38}$$

For values of $\gamma^* < \gamma_{\text{sup}}$ the particle gets truncated and for $\gamma^* < 0$ it will be less than half in hight as the equivalent unsupported particle as seen in Fig. 3.32 If the surface free energies are known, the work of adhesion can be derived from the experimentally accessible shape (height and width) of the particles. In this work, the concept of the Wulff construction was applied to analyse the growth of Cu on Mo(001) in the presence of oxygen in chapter 9.

Chapter 4

Experimental setup

Experiments have been conducted in a custom-built ultra-high-vacuum low-temperature scanning-tunneling-microscope setup. The system consists of four UHV chambers shown in Fig. 4.1: the STM, Preparation, XPS and high pressure chamber. All chambers are separated by gate valves, enabling the sample to be transferred from one chamber to another without breaking the vacuum.

4.1 The Preparation and XPS Chambers

The preparation chamber is equipped with standard sample preparation and analysis facilities that is: LEED (low energy electron diffraction), Quadrupole Mass Spectrometry (QMS), Ion Sputtering and a heating stage.

Samples can be cleaned by argon ion sputtering usually followed by annealing in the heating stage. In the heating stage samples can be heated up to 900 K using electron bombardment. Electrons are emitted from a filament and then accelerated towards the backside of the sample by voltages of up to 2000 V leading to emission currents of up to 100 mA. Temperatures are measured with a pyrometer (Metis MI16 by Sensotherm GmBH) connected to a PC for easy recording of temperature curves.

To prepare oxide films the preparation chamber contains a leak valve connected to a 12 bar O_2 bottle allowing for high partial oxygen pressure while evaporating metals such as copper from an electron beam evaporator. For the latter purpose, electrons are emitted from a tungsten filament and accelerated towards the crucible thus heating and evaporating copper towards the sample. Some of the copper atoms are ionized and able to reach the flux monitor resulting in a current proportional to the atomic copper flux. The deposited film thickness is controlled by evaporation flux and exposure time.

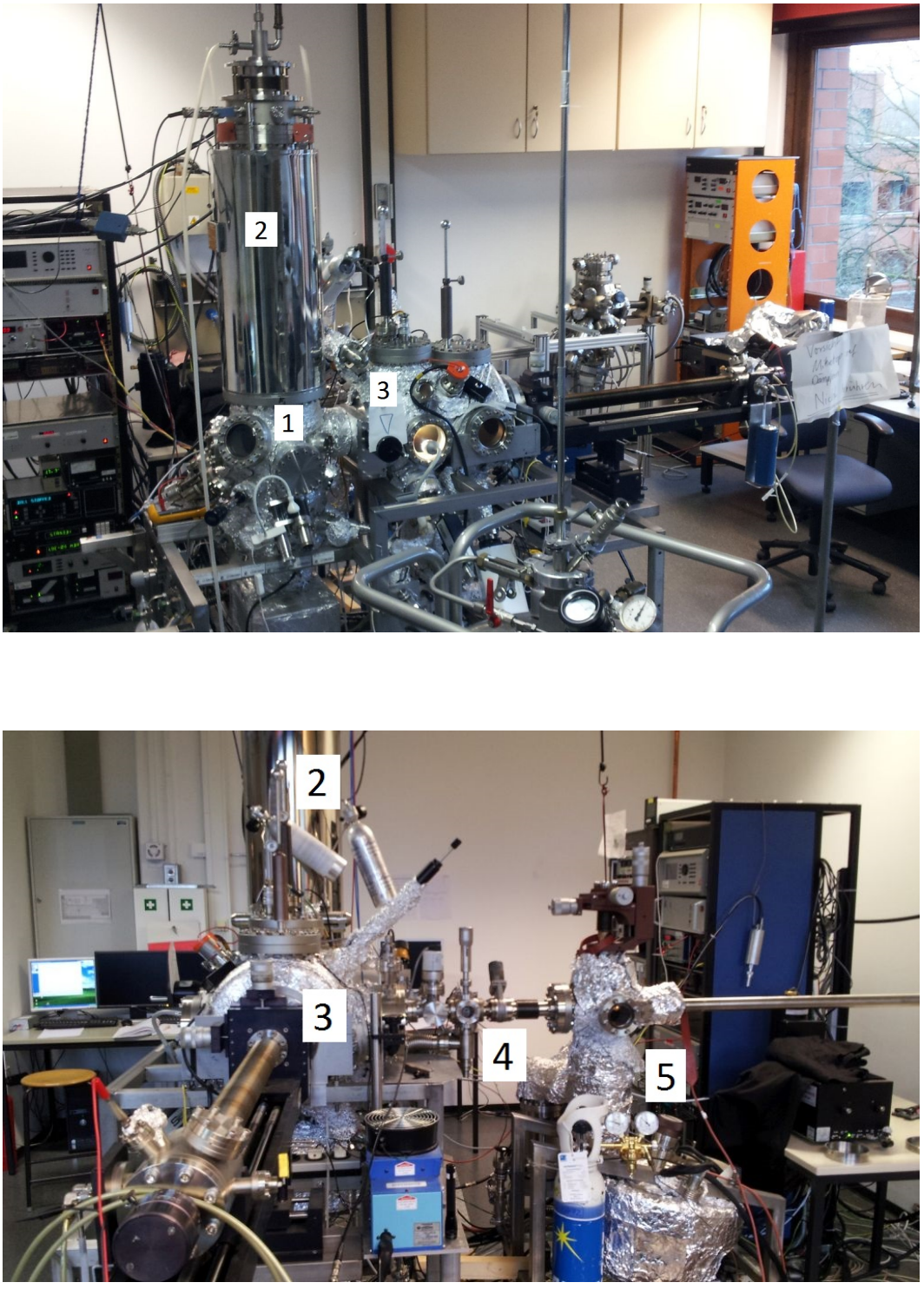


FIGURE 4.1: Pictures of the UHV-Setup. 1: STM chamber, 2: bath cryostat, 3: preparation chamber, 4: high pressure chamber, 5: XPS chamber

A manipulator with four degrees of freedom allows to transfer samples between different positions within the chamber or towards the STM. The manipulator can be cooled with liquid nitrogen lowering the sample temperature to approximately 100 K. Alternatively the sample can be heated up to 550 K by resistive heating. The temperature is monitored by a chromel/alumel thermocouple spot welded to the end of the manipulator.

The base pressure below 5×10^{-10} mbar is maintained by a turbo-molecular pump and an ion-pump. The resulting pressure is measured with a Leybold Heraeus IM220 Ionivac ion gauge. The UHV setup is damped against external vibrations by six active piezo damping elements (AVI350S by JRS Scientific Instruments) in a frequency window of 0.8 Hz to 200 Hz.

XPS measurements were carried out with a hemispherical electron analyser (ESCALAB 200) combined with non-chromatized Mg-Kα and Al-Kα twin source. The XPS chamber is attached in a T-configuration with respect to the preparation chamber (see Fig. 4.1). A second transfer rod is used to transfer samples to the XPS chamber or the high pressure chamber. The XPS chamber is pumped by a separate turbo pump, reaching a base pressure of 5×10^{-10} mbar.

The high pressure chamber (HPC, see section 4.3) located between XPS and preparation chamber serves as a load lock. The HPC is pumped by a separate turbo pump reaching 1×10^{-7} mbar after two hours of pumping.

4.2 The STM Chamber

The STM scan head was realized as a Besocke type as shown in Fig. 4.2. The metal sample holder shows a triple helix structure at the bottom with an inclination of 1 mm/120°. During scans the sample is placed on three piezo tubes. When rotating the sample it can be approached or retracted from the tip. The piezo tubes are electrically isolated from the samples by small sapphire parts. The small steel balls on top of the sapphire connect the tunnel bias voltage to the sample holder and reduce mechanical friction during sample movement. Apart from retracting and approaching, coarse x-y-movement of the sample is possible. The tip is mounted on a fourth piezo in the middle of the setup which is used for the scan movement. A detailed description of the system can be found in [74].

Low temperatures are achieved using a top-mount bath cryostat (CryoVac GmbH) with two dewars of 8.5 l and 19 l capacity. During measurement the cryostat is filled with liquid nitrogen. The STM head is surrounded by movable cryo-shields connected to the

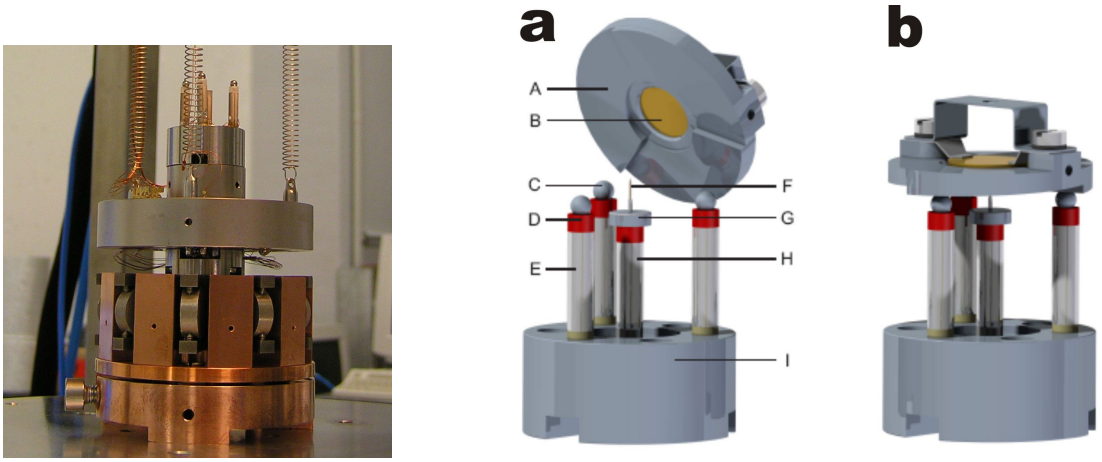


FIGURE 4.2: Left: Photo of the STM scan head hanging on springs and damped by an Eddy Current Unit. Right: Drawing of the scan head setup[74]. A: ramp with different sectors, B: sample, C: support ball, D. sapphire, E: support-piezo, F: tip, G: tip-holder, H: scan-piezo, I: base [64]

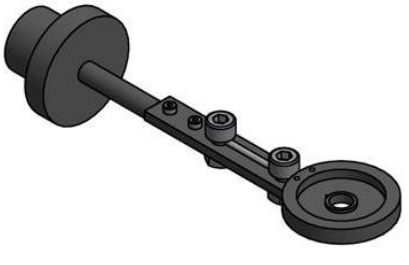
dewars. The temperature measurement is done using the characteristic voltage curve of a Si-diode (DT 470 BO by Lake Shore) connected to the base plate of the STM.

As mentioned before the UHV setup is damped against external vibrations by six active piezo damping elements (AVI350S by JRS Scientific Instruments) in a frequency window of 0.8 Hz to 200 Hz. Higher frequencies are damped using a passive spring suspension system. Additionally the STM stage is damped against the cryo-shields with an eddy current damping system.

A commercial control electronic (SPM 100 by RHK Technology) was used to operate the STM. Images were treated using WSxM software [127] afterwards.

4.3 The High Pressure Chamber

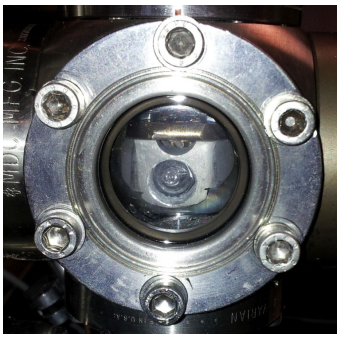
The new high pressure chamber was designed to oxidise metal thin films evaporated before in the preparation chamber. As a wide combination of temperatures and oxygen pressures are accessible, preparation of metal oxides in different oxidation stages and thickness regimes could be achieved. Note that the main preparation chamber of the setup is suitable only for O_2 partial pressures of up to 10^{-5} mbar, a value that is often too low to oxidise chemically inert metals, such as copper.
To be able to prepare thick oxide films the load-lock of the UHV system was upgraded to a high pressure chamber shown in Fig. 4.3. An Alphagaz2 S10 O_2-bottle with 200 bar and 99,9995% purity was attached to the HPC by means of a pressure regulator (up to 5 bar) and a leak valve. This allows for oxygen partial pressures adjustable between 10^{-4} mbar to 500 mbar. The already present turbo pump allows for a quick evacuation



(A) Schematic drawing of the new sample holder



(B) Test of the aluminium heating block



(C) Installed sample holder with aluminium heating block

FIGURE 4.3: Setup of the new high pressure chamber. The back of the sample holder is attached to a linear transfer rod. Underneath the circular plate that holds the sample the aluminium heating block is attached.

of the relatively small chamber after the high pressure preparation. The base pressure of 1×10^{-7} mbar is reached after two hours of pumping. The sample can then be analysed via XPS or STM. During the experiments the thick oxide films prepared in the HPC turned out to be too rough for successful STM analysis. However chemical characterization via XPS was done. Additionally the HPC can be opened and the sample removed to be analyzed ex-situ to characterize optical properties as is done recently in a Master thesis [128].

A special sample holder (Fig. 4.3) was developed for the HPC. Because the HPC is in between the preparation and the XPS chambers, the new holder had to be retractable so not to block the access to the XPS chamber. This was realized by attaching it to a short linear transfer rod.

Below the sample holder an aluminium heating block is attached which houses an Osram 64642 HLX lamp. The lamp is operated with a standard voltage supply. The maximum voltage is 24 V and the maximum power through-put 150 W. The lamp reaches up to 900 K easily. The aluminium block transfers the heat evenly on the sample. A type K thermocouple attached to the sample holder is used to monitor the temperature.

Part II

Scientific Results

Chapter 5

Introduction to Cu_2O

5.1 Structural Properties

Cu_2O forms a simple cubic Bravais lattice [129] with six atoms per unit cell as seen in Fig. 5.1. This results in two interwoven sub-lattices hold together by dispersive Cu-Cu forces [130]. In each sub-lattice oxygen (red balls) forms a bcc structure binding four Cu(I) ions (turquoise balls) in tetrahedral coordination. Thus all oxygen atoms are fourfold coordinated to the nearest copper atoms which in turn are two-fold linearly coordinated between two oxygen atoms. Lattice parameters and atomic distances are given in Tab. 5.1.

Other phases of copper oxides are CuO and Cu_4O_3. Cupric oxide (CuO) crystallizes in a monoclinic unit cell. Copper atoms in CuO are planar four-fold coordinated by oxygen atoms whereas oxygen atoms are coordinated by four copper atoms in a slightly distorted tetrahedron. Cu_4O_3 is of tetragonal symmetry. The crystal is built by twofold

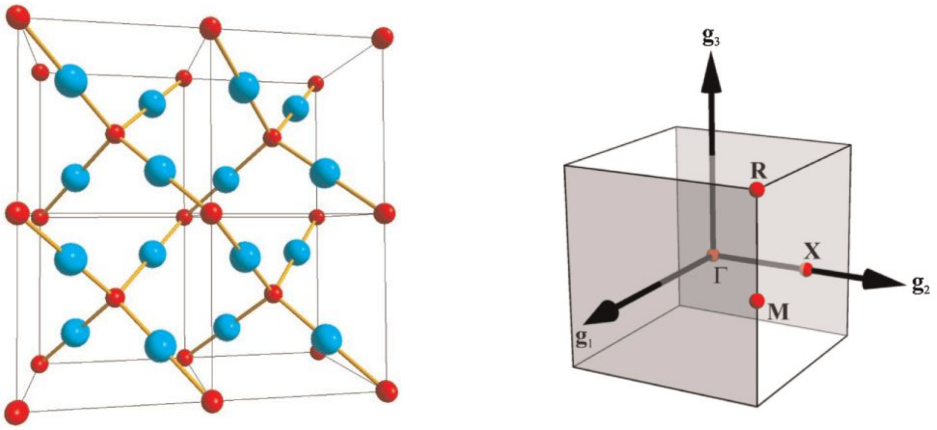


FIGURE 5.1: Unit cell and Brioullin zone of Cu_2O. [52]

Cu_2O	unit cell	a = 4.27 Å α = 90°
	bond length Cu-O	1.85 Å
	separation O-O	3.7 Å
	separation Cu-Cu	3.02 Å
CuO	unit cell	a=4.68 Å b=3.42 Å c=5.13 Å α=β=90° γ=99.54°
	bond length Cu-O	1.96 Å
	separation O-O	2.62 Å
	separation Cu-Cu	2.90 Å
Cu_4O_3	unit cell	a=5.837 Å c=9.832 Å

TABLE 5.1: Structural properties of copper oxides [52]

coordinated Cu^+ ions as in Cu_2O and fourfold coordinated Cu^{2+} as in CuO. Lattice parameters of both CuO and Cu_4O_3 are given in Tab. 5.1. The unit cell and Brillouin zone of CuO and Cu_4O_3 are shown in Fig. 5.5 and Fig. 5.6 respectively.

As for most thin-films there are a variety of ways to produce Cu_2O thin films: electro-deposition, sol-gel, spray and sputtering [23, 131–134] just to name a few. Also a wide variety of substrates can be used. Cu_2O deposition on sapphire or glass for example leads to textured films with grain sizes from 40 to 100 nm.
To achieve epitaxial growth of a thin-film a substrate with a matching lattice constant has to be chosen. For the cubic Cu_2O MgO is a good match with the unit cells almost identical in size: a(MgO)=4.213 Å and a(Cu_2O)=4.269 Å. Deposition of Cu_2O on MgO has been done in various studies, using molecular beam epitaxy [135], chemical vapour deposition [136] and pulsed laser deposition [21, 137].
However preparation procedures and substrate temperatures still play a critical role even though an epitaxial relationship between substrate and deposited thin film has been ensured. Because of the very small lattice mismatch [21, 135–137] cube on cube growth with 001 orientation should be preferable for Cu_2O on MgO(001). Instead the Cu_2O-layer is rotated by 45° in plane resulting in a 3:4 orientation with the edges of the Cu_2O cell along the face diagonals of MgO [137]. In this case the surface energy anisotropy rather than the lattice match determines the orientation.
Studies on Cu_2O thin-films done by Meyer et. al [52] show that by varying the oxygen flow during copper deposition the level of oxidation can be tuned from metallic Cu to CuO. A rather wide range of oxygen flow rates at a substrate temperature of 400° C yielded Cu_2O, but only a small interval of oxygen flow rates resulted in pure Cu_2O. With too little oxygen during preparation Meyer et. al found metallic copper inclusions whereas with too high oxygen flow rates CuO started to show up. Cu_4O_3 was found at intermediate oxygen flow rates where Cu_2O changes to CuO.

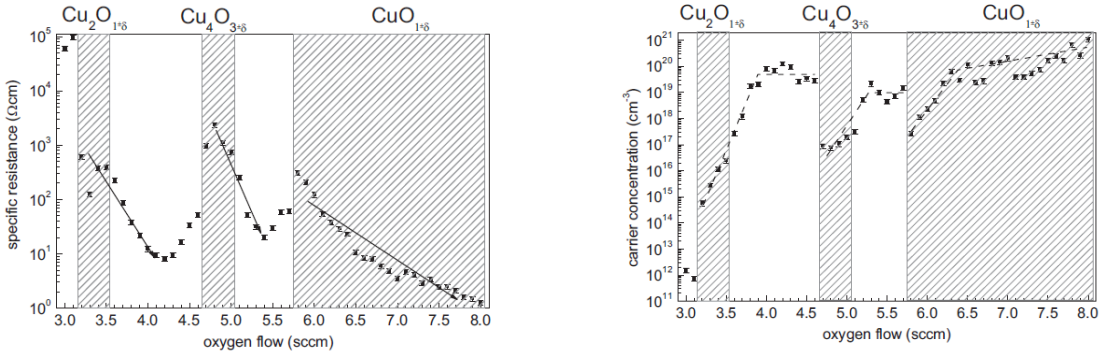


FIGURE 5.2: Specific resistance and hole carrier concentration in Cu_2O depending on oxygen flow during preparation [52]

5.2 Electronic Properties

Cuprous oxide is a semiconductor with a band gap of 2.1 eV as shown by experimental studies [19]. Other copper oxides have smaller band gaps of 1.4-1.7 eV and 1.5 eV for CuO and Cu_4O_3 respectively. Values for the band gaps are shown in Tab. 5.2.

Cu_2O	direct optical	2.17 eV [52] 2.62 eV [52]
CuO	indirect	1.4-1.7 eV [52, 97, 138, 139]
Cu_4O_3	indirect	1.5 eV [52]

TABLE 5.2: Experimentally determined band gaps of different copper oxides.

As shown from experimental findings [52] the oxygen flow rate during thin-film preparation controls which oxide forms. Also the obtained oxide films vary by two orders of magnitude in resistivity within each oxide phase as shown in Fig. 5.2 on the left. This is likely due to hole carrier density which changes according to the oxygen flow used during preparation, as seen from hall measurements shown in Fig. 5.2 on the right. The Cu_2O carrier density starts at $10^{15}\,cm^{-3}$ and increases to $10^{19}\,cm^{-3}$. This is commonly interpreted as a change in stoichiometric composition most likely by creating copper vacancies which allows for the electrical conductivity and hole density to be tuned.

To reproduce the experimental findings calculations of the electronic states have been done. Among the different copper oxides the most work was performed for Cu_2O [130, 140]. Ab initio density functional theory (DFT) can be used to calculate the density of states, however this is challenging for copper oxides. The crucial ingredient in DFT studies is the exchange-correlation functional being often simplified via mean-field approaches (LDA, GGA). As known local density approximation (LDA) underestimates band gaps therefore an empirical Hubbard term is used (LDA + U). LDA calculations for Cu_2O [25, 141, 142] show an underestimation of the band gap by 1.5 eV. LDA+U yields a somewhat better result by some hundred meV [142, 143].

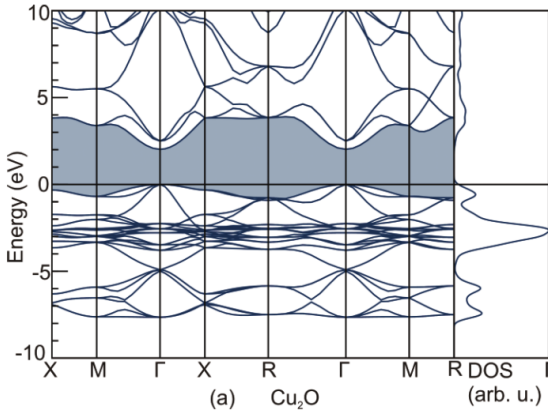


FIGURE 5.3: Band structure of Cu_2O with a direct band gap at Γ and the resulting DOS as calculated in hybrid functional DFT. The calculated values for the indirect band gap are 0.7 (LDA), 0.99 eV (LDA+U) and 2.02 eV (HSE) and for the optical band gap 0.99 (LDA), 1.88 eV (LDA+U) and 2.5 eV (HSE). [145]

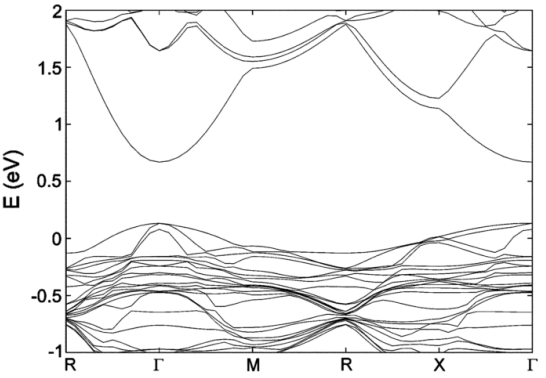


FIGURE 5.4: Band structure of Cu_2O with consideration of copper vacancies. Around Γ and along Γ-X the VBM crosses the Fermi level contributing hole states for p-type conductivity. [146]

In Cu_2O the highest VB states stem from the fully occupied Cu $3d^{10}$ states. The O 2p states are a little lower inside the VB and the lowest energy conduction band is of Cu 4s character. However partial occupation of Cu 4s states may exist which together with Cu 3d-3d interactions contributes to a direct band gap of 2.1 eV (at Γ point) as shown in Fig. 5.3. In optical experiments a band gap of 2.6 eV is measured. This is because the VBM has predominantly Cu-d character and is of even parity while the CBM has a strong Cu d_{z^2} contribution and is also of even parity. Hence the direct optical transition is dipole forbidden. The CB at 0.45 eV higher energy is of odd parity causing the strong increase of absorption above 2.5 eV [144].

Most DFT calculations are done for stoichiometric Cu_2O. However this might not be the best choice. After all Cu_2O is known to be p-conductive because of inherent copper vacancies V_{Cu} as will be discussed in section 5.3. Fig./,5.4 shows the calculated band onset for Cu_2O with V_{Cu} present [146]. The VB is still predominantly Cu 3d, but a tail of Cu 3d states crosses the Fermi level forming acceptor states above the valence band characteristic for p-type materials. The number of hole states above the Fermi level, especially around the Γ-point and along Γ-X direction suggests that delocalized holes are present upon V_{Cu} formation. An acceptor state 0.2 eV above the VB at Γ point with an energy gap to the conduction band of 0.5 eV is found consistent with experimental findings [24, 147]. According to Raebiger et al. [148] a good p-conductivity arises from a VBM formed by the interaction between a filled anion shell and a filled cation shell that lie as high in energy as possible. Thus suitable materials contain d^{10} electrons as Cu($3d^{10}$ $4s^1$), Ag($4d^{10}$ $5s^1$), and Au($4f^{14}$ $5d^{10}$ $6s^1$).

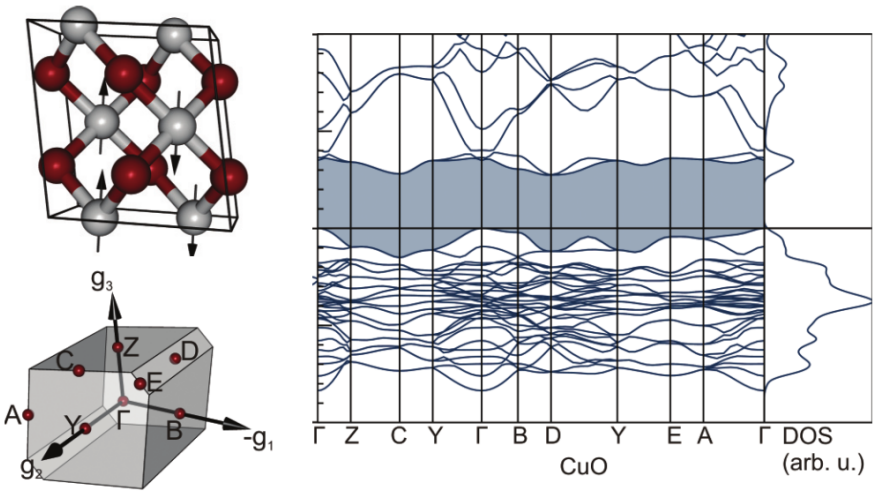


FIGURE 5.5: left: Structure and Brillouin zone of CuO. Arrows indicating the antiferromagnetic ground state and high symmetry points are shown. right: Band structure of CuO with an indirect band gap at Γ-D and the resulting DOS as calculated in hybrid functional DFT. The calculated values for the indirect band gap are 1.39 eV (LDA+U) and 2.74 eV (HSE) and for the direct band gap at B-point 1.91 eV (LDA+U) and 3.26 eV (HSE). [145]

Neutron-scattering experiments show that CuO is antiferromagnetic below 220 K [149] which doubles the the size of the unit cell as compared to the primitive unit cell of the crystal [145] and makes calculations of the electronic structure even more demanding. The band structure of CuO is shown in Fig. 5.5 calculated from LDA+U yielding an indirect band gap of 1.0 eV [150] with the minimum of the CB at the D point. Because of the indirect band gap the carrier effective masses are not isotropic. The electron effective mass along the Γ-D direction are different to those perpendicular to Γ-D. The VBM and the CBM are both predominantly of Cu 3d orbitals. Compared to e.g. silicon where the CB states are from s-p hybridization this leads to a smaller curvature of the band in CuO. Also the d-electrons are more localized than sp electrons overall yielding a smaller carrier mobility.

Similar to CuO, Cu_4O_3 is antiferromagnetic in its ground state doubling the crystallographic unit cell in all three directions [151]. However hybrid functional DFT shows an indirect band gap in Fig. 5.6. Calculations also suggest that Cu_4O_3 is not a thermodynamically stable phase but possibly metastable at the phase transition of CuO to Cu_2O matching experimental observations [52].

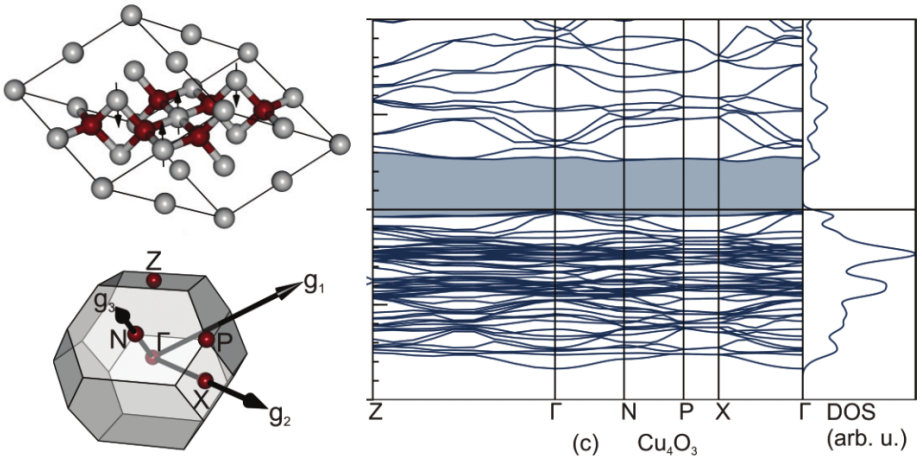


FIGURE 5.6: left: Structure and Brillouin zone of Cu_4O_3. Arrows indicating the antiferromagnetic ground state and high symmetry points are shown. right: Band structure of Cu_4O_3 with an indirect band gap at Γ-N and the resulting DOS as calculated in hybrid functional DFT. The calculated values for the indirect band gap are 1.2 eV (LDA+U) and 2.54 eV (HSE) and for the direct band gap at Γ-point 1.47 eV (LDA+U) and 2.71 eV (HSE). [145]

5.3 P-type Conductivity

Already in 1951 [56] the nature of Cu_2O was described as "copper oxide is a defect semiconductor ... the main impurity centres, acceptors in this case, are probably vacant ion lattice sites". Recent experimental [24, 52, 147] and theoretical studies [148, 152] still characterize cuprous oxide as a naturally p-type semi-conductor. Copper vacancies are widely believed to act as shallow acceptors.

For an oxide to be p-conductive a stable and large concentration of holes is paramount. Additionally a good mobility of the holes is valuable to achieve good p-type conductivity. Thus to create a good p-type conductor a few specifications have to be met [148] :

- A low formation energy of defects that produce holes such as cation vacancies (acceptors)
- A small ionization energy of such defects, so that holes can be released (i.e. shallow acceptor levels close to the VBM)
- A high formation energy of defects that act as "hole killer" such as anion vacancies and cation interstitials (donors)
- A highly disperse and delocalized VB to ensure light hole masses and thus good mobility

A small formation energy means a defect is easily created and there will be a high concentration of these defects. A small ionization energy describes a defect that is easily

charged. In the case of an acceptor the defect will change from neutral to negatively charged with the ionization energy $\epsilon(0/-)$ leaving a hole (to preserve the total amount of charges) that can possibly contribute to p-type conductivity.

Cu_2O is well known to be naturally p-conductive. This is generally attributed to a non-stoichiometry with carrier concentrations that depend on the amount of cation deficiency [153]. The presence of hole states above the valence band is attributed to copper vacancies [24, 147].
There are a number of theoretically possible defect sites in Cu_2O. Copper vacancies V_{Cu}, copper interstitials Cu_i, oxygen vacancies V_O and oxygen interstitials O_i. Of these V_{Cu} and O_i can act as acceptors whereas V_O and Cu_i can act as donors. There are two types of copper vacancies: the simple vacancy V_{Cu} and the split vacancy $V_{Cu,split}$. They are different in the way the remaining atoms arrange around the vacancy, but are not so different in terms of formation and ionization energies [146, 148, 150, 152–154]. Also there are two possible oxygen interstitial sites in octahedral and tetrahedral position within the lattice, which again differ not too much in their formation and ionization energies [146, 148, 154].
From the possible defects V_{Cu} and $V_{Cu,split}$ show the smallest formation energies ($\leq$1 eV) both under Cu rich / O poor as well as Cu poor / O rich conditions [148]. Thus copper vacancies are the predominant defect type in Cu_2O. The next common type are oxygen interstitials O_i (in both configurations) with formation energies between 1 eV and 2 eV for both growth conditions. Both V_{Cu} and O_i act as acceptors thus possibly contributing to p-type conductivity. The ionization energy $\epsilon(0/-)$ to change V_{Cu} to a negatively charged state is at E_i=0.28 eV [148] and thus close to the VBM, forming a shallow acceptor state. O_i are slightly higher in ionization energy as seen in Fig. 5.8.

The single particle level of a copper vacancy is 4 eV below the VB shown in Fig. 5.7 on the top. However due to the surrounding atoms the single particle levels merge to the band structure of Cu_2O as seen in Fig. 5.7. The VB in Cu_2O is derived from the occupied Cu(d) states. thus the hole created at 4 eV below the VBM can "float up" to the VBM (or rather an electron from the occupied VB drops down to ionize the defect). In contrast in ZnO the single particle level is at 1 eV above the VBM resulting in localized hole states. Furthermore the VB in ZnO is derived from the unoccupied Zn(p) orbitals thus the hole cannot reach the VB which is why ZnO is not p-conductive.

The possible "hole killers" for Cu_2O are V_O and Cu_i. The formation energy of V_O is only slightly higher than that of copper vacancies but it is only stable in the charge neutral state [155]. Copper interstitials have a very high formation energy making them unlikely to appear. Also copper interstitials are amphoteric in nature, meaning that they will act as an acceptor under n-type conditions and as a donor under p-type conditions, thus

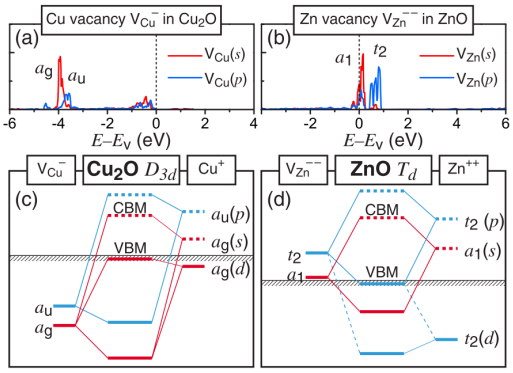


FIGURE 5.7: (a+b) local density of states of copper and zink vacancies in Cu_2O and ZnO respectively. (c+d) Schematic band diagram of Cu_2O and ZnO constructed from the interaction of the single vacancy levels (left) and the free metal ions (right). In Cu_2O holes from the vacancy can "float up" to the occupied VBM. [148]

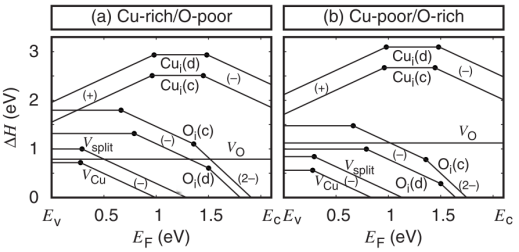


FIGURE 5.8: Formation energies and ionization levels for intrinsic defects in Cu_2O under different preparation conditions. [148]

counteracting any type of conductivity. The negatively charged state lies high inside the band gap but with the Fermi level close to the VBM it will not be occupied under equilibrium conditions.

The equilibrium carrier concentrations derived from thermodynamic simulations at T = (800-1400) K growth temperature show V_{Cu} to be predominant at $(10^{18} - 10^{20})\,cm^{-3}$ matching experimental results [156]. O_i are 1-2 orders less abundant at $(10^{16} - 10^{18})\,cm^{-3}$ and Cu_i are hardly formed ($\leq 10^{14}\,cm^{-3}$). While at high temperatures the carrier concentration follows the defect concentration closely, meaning almost all V_{Cu} have released a hole to the VB the carrier concentration drops at T=300 K by a few orders of magnitude. Only a small fraction of the available defects will be ionized at room temperature.

Cu_2O is intrinsically copper deficient with V_{Cu} forming shallow acceptor states and acting as efficient hole producers. The potential hole killers V_O and Cu_i cannot suppress p-type conduction, because V_O has no transition level within the band gap and Cu_i has a high formation energy and deep transition levels.

5.4 The Cu_2O Surface

The Cu_2O(111)-surface consists of Cu-O-Cu trilayers with a 2.47 Å spacing between copper planes along the film normal [26]. As with every surface there are unsaturated atoms that have less binding partners than the equivalent atoms in the bulk. In the case

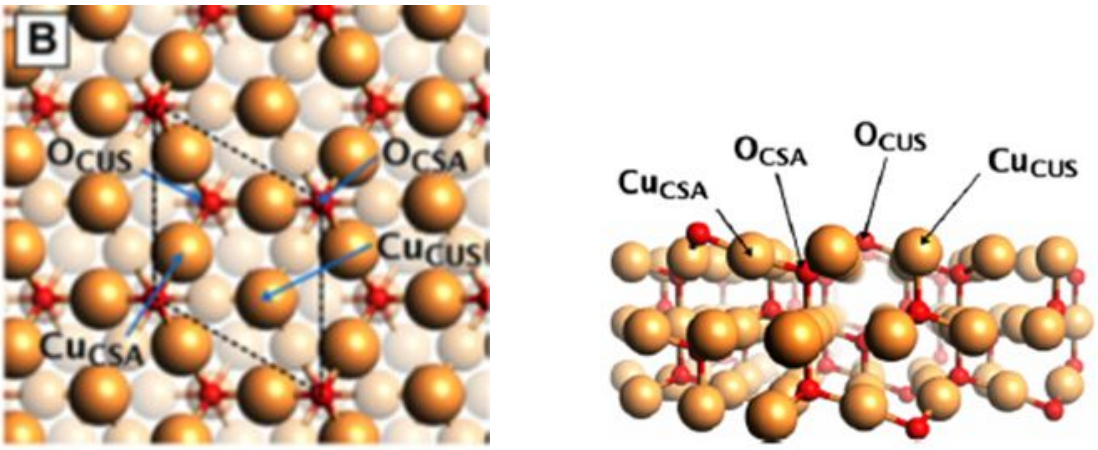


FIGURE 5.9: The $Cu_2O(111)$ surface top view and side view. Coordinativley saturated and unsaturated atoms are marked. [130]

Cu_2O-(111)	unit cell	(6.04×6.04) Å^2 60°
	Cu_{cus} - Cu_{cus}	6.04 Å
	Cu_{csa} - Cu_{csa}	3.02 Å
	O_{cus} - O_{cus}	6.04 Å
	O_{csa} - O_{csa}	6.04 Å
Cu_2O-(110)	unit cell	(4.27×6.04) Å^2 90°
	Cu - Cu	3.02 Å
	O - O	3.7 Å

TABLE 5.3: Structural properties of Cu_2O surfaces [52]

of $Cu_2O(111)$ there are **c**oordinatively **sa**turated copper ions (Cu_{csa}) bound to two ions in the layer above and below and **c**oordinativly **uns**aturated copper ions (Cu_{cus}) with only one oxygen binding partner in the layer below. Correspondingly there are saturated oxygen atoms (O_{csa}) with four Cu-partners and unsaturated oxygen atoms (O_{cus}) with only three Cu-partners. The resulting structure of $Cu_2O(111)$ has a (6.03×6.03) Å^2 unit cell shown in Fig. 5.9.

According to earlier theoretical [4, 130, 140] and experimental [18, 157] studies $Cu_2O(111)$ is composed of rows of saturated copper atoms Cu_{csa} alternating with rows that feature alternating saturated Cu_{csa} and unsaturated Cu_{cus} within one row. The atomic distances of Cu-Cu within the (111) plane are close to that of Au(111) with a lattice mismatch of 3.8% only. Thus Au(111) is a good substrate for the growth of $Cu_2O(111)$ thin films.

The (110) surface of cuprous oxide features a rectangular unit cell measuring (4.27×6.03) Å^2 containing two copper and oxygen atoms. All copper atoms in the $Cu_2O(110)$ are coordinatively saturated whereas all oxygen atoms are only three-fold instead of four-fold coordinated as in bulk cuprous oxide. The (110) surface structure features a zig-zag pattern of alternating copper and oxygen atoms shown in Fig. 5.10.

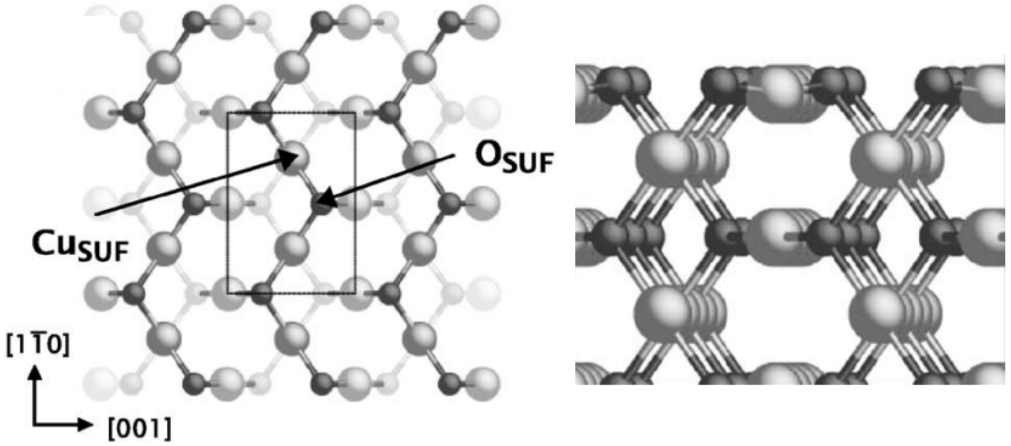


FIGURE 5.10: $Cu_2O(110)$ surface top and side view. The topmost Cu atoms together with the topmost oxygen atoms form parallel zig-zag chains. [3]

The stability of surfaces depends on the amount of energy used to generate the surface. The smaller the surface free energy the more stable a surface will be. Therefore most systems undergo a change with respect to the bulk structure to reduce the surface energy as e.g. the well-known herringbone reconstruction for Au(111). Surface free energies for the Cu_2O-surfaces have been calculated by DFT studies [3, 5] showing the stoichiometric $Cu_2O(111)$-surface to be higher in energy than the same surface with missing uncoordinated copper ions $Cu_2O(111)$-Cu_{cus} as shown in Fig. 5.11. This result will be challenged later in this work.

Alternative structures such as the $(\sqrt{3} \times \sqrt{3})R30°$ surface formed after annealing a $Cu_2O(111)$ bulk crystal [18]. Annealing a Cu(111) crystal in an oxygen atmosphere

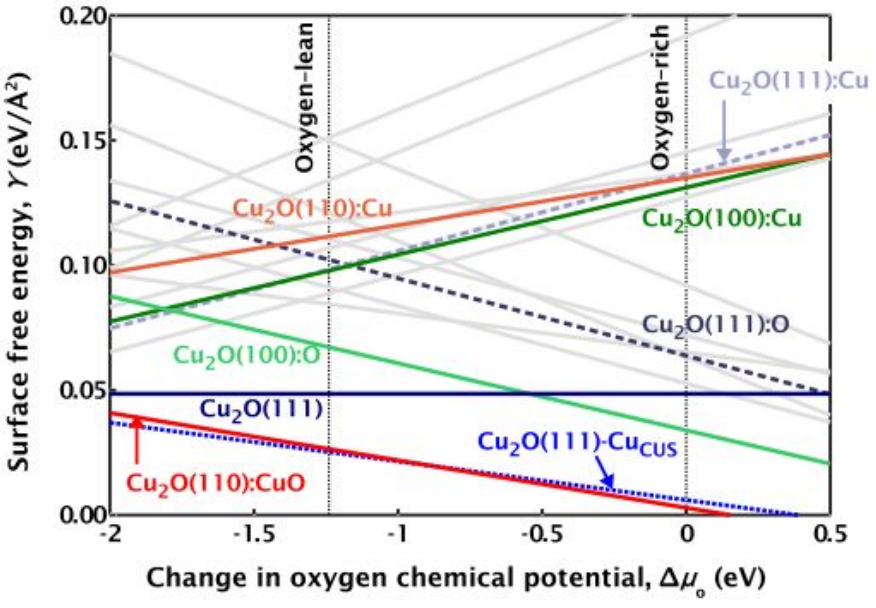


FIGURE 5.11: Surface free energies of $Cu_2O(111)$ as calculated by Soon and Co-workers [3, 5].

leads to an oxygen ad-structure that can be seen as an "oxide precursor" before the formation of a bulk oxide [26]. Jensen and co-workers [26] found two coincidence structures for the Cu + O layer on Cu(111). The first coincidence lattice shows a unit cell 29 times larger than the primitive unit cell whereas the second structure features a unit cell 44 times larger. Hence they have been dubbed "29" and "44" structure. Jensen et al also identified a hexagonal substructure with 6 Å periodicity leading to the assumption that the oxide layer bears resemblance to the $Cu_2O(111)$ surface. A model consisting of three O and two Cu layers was proposed. Matsumoto at al. [27] studied the 29 and 44 structures in great detail, again arriving at a structural model derived from the $Cu_2O(111)$ surface as shown in Fig. 5.12.
Due to the lattice mismatch between oxide and bulk Cu(111) of 12% and 2% for the 29 and 44 structure respectively [26] the hexagonal Cu-O network is distorted relatively little for the 29 structure but severely distorted for the 44 structure. From a high energy ion scattering combined with nuclear reaction analysis and Auger spectroscopy Jensen et al. found the concentrations of Cu and O to be 1.05 ML and 0.52 ML respectively. From this they deduced that the Cu_{cus} ions are missing, exposing the underlying oxygen atoms.
In the structure models derived by Matsumoto et al. (Fig. 5.12) copper ions are represented as white balls while, (subsurface) oxygen atoms are (dark) grey. In the 29 structure some of the subsurface O_{csa} are missing too, exposing the Cu(111) substrate.

Önsten and co-workers [18] found a $(\sqrt{3}\times\sqrt{3})R30°$ surface on a $Cu_2O(111)$ crystal after annealing in UHV conditions at 800-1000 K. Annealing in oxygen atmosphere restored the surface to the hexagonal (1x1) structure. Two different types of protrusions called P1 and P2 are observed. P2 protrusions are hexagonally arranged with a distance of 6 Å whereas P2 are also hexagonal but 11 Å apart. Both P1 and P2 can coexist on the surface as shown in Fig. 5.13 c and f. Annealing in oxygen increases the number of P2 whereas annealing in UHV increases the number of P1 features. This is interpreted as the P1 features representing the formation of oxygen vacancies.
Two models A and B for both types of surface terminations are proposed by Önsten and co-workers [18] as shown in Fig. 5.13. Model A starts with a stoichiometric $Cu_2O(111)$-(1x1) surface. The P2 protrusions are assigned to Cu_{cus}. Upon removal of 1/3 of the surface oxygen ions the $(\sqrt{3}\times\sqrt{3})R30°$ surface develops. The large P1 protrusions are believed to consist of 6 copper ions.
Model B starts from the (1x1)-Cu_{cus} surface. P2 protrusions are now at the place of the missing Cu_{cus} where the subsurface oxygen and surrounding Cu_{csa} give rise to the contrast in STM. Again after removal of 1/3 of surface oxygen the $(\sqrt{3}\times\sqrt{3})R30°$ surface develops. In this model the P1 are assigned to a group of nine Cu_{csa}.

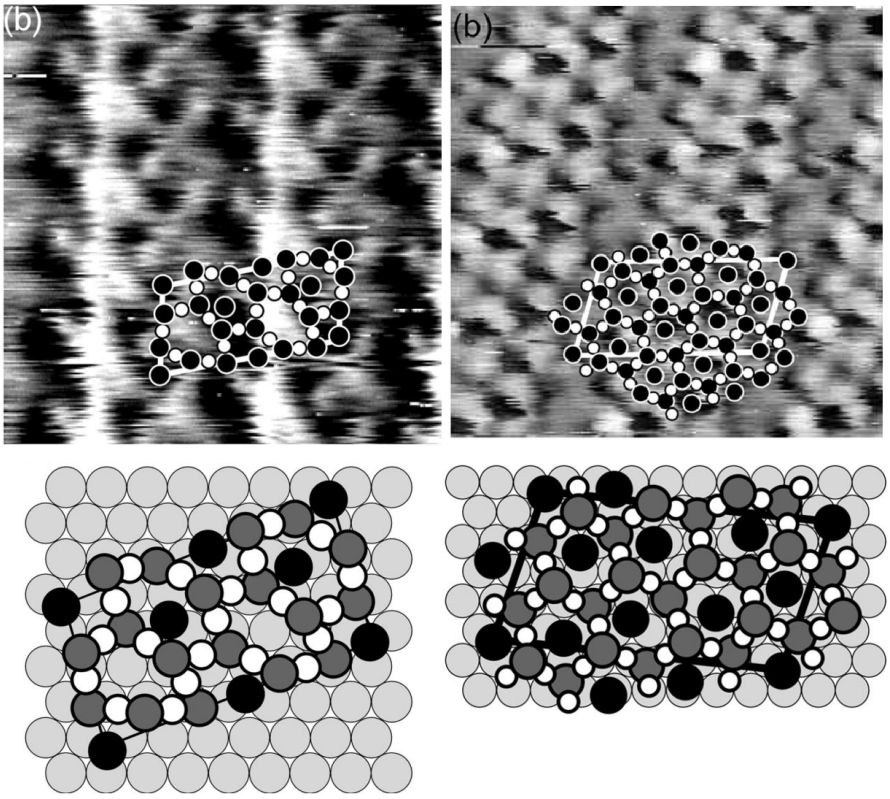


FIGURE 5.12: "29" (left) and "44" (right) structure of a $Cu_2O(111)$ overlayer on Cu(111) as found by Matsumoto and co-workers. Copper atoms are represented in white, (subsurface) oxygen atoms are (dark) grey. Cu_{cus} are missing from the surface. For the 29 structure also some oxygen atoms are missing. [27]

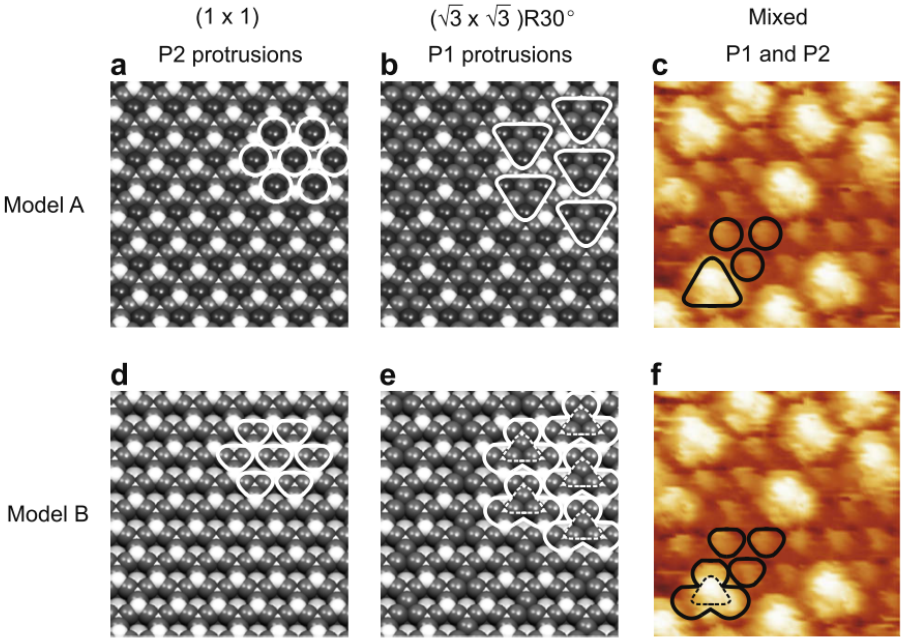


FIGURE 5.13: $(\sqrt{3} \times \sqrt{3})$R30° as found by Önsten and co-workers. P1 maxima increase with annealing in UHV whereas P2 increase with annealing in oxygen. STM images (c,f) of $(4.4 \times 4.4)\,\text{Å}^2$ show both features P1 and P2. Two structural models are proposed: Model A (a,b) starts from the stoichiometric (1x1) surface (a) whereas Model B (d,e) starts with the (1x1)-Cu_{cus} surface (d). In both models P1 emerge upon the removal of 1/3 of surface oxygen ions (b,e). White balls indicate oxygen ions whereas dark and light grey balls symbolize Cu_{cus} and Cu_{csa} respectively. [18]

Chapter 6

Preparation of Cu_2O Thin Films

Before preparation of Cu_2O thin films the Au and Mo crystals used as substrates are cleaned by several sputtering and annealing cycles. Ar^+ ion sputtering was set to 0.8 kV and 1.5 kV for Au and Mo respectively. Subsequent heating was done at 900 K and 1500 K for the Au and Mo crystal. The cleanness and flatness of the crystals was checked with XPS and STM respectively. Also using LEED (Figs. 6.1 and 6.2) the expected hexagonal and square symmetry of gold and molybdenum was observed, speaking for the long range order of the cleaned surfaces. In the first step elemental Cu is dosed onto the sample from an electron-beam evaporator in an O_2 ambience ranging from 1×10^{-6} mbar to 1×10^{-5} mbar. During evaporation the sample is held at room temperature or slightly above (up to 500 K) by resistive heating at the manipulator. The temperature was monitored by a thermocouple at the manipulator. Also, to reach higher temperatures during reactive copper deposition, samples were prepared directly after ending a sputter-anneal cycle, with the sample still at higher temperature ("hot preparation"). Thin films not subjected to any further treatment are referred to as **as-grown films**.

After evaporation the sample could be annealed using electron bombardment to access thermal equilibrium states. Annealing was done under UHV conditions or in oxygen partial pressures. The temperature was monitored via a pyrometer or calculated from the heating power. These samples are referred to as **annealed films**.

To be able to prepare samples at higher oxygen pressures the high pressure cell (see section 4.3) was constructed. After dosing elemental Cu in the usual preparation chamber the sample was transferred into the HPC where it was annealed in p_{O2} ranging from 1×10^{-5} mbar to 0.1 mbar. Sample temperature ranging from 400 K to 600 K was monitored with a type k thermocouple.

To handle the sometimes competing influences of oxygen partial pressure and sample

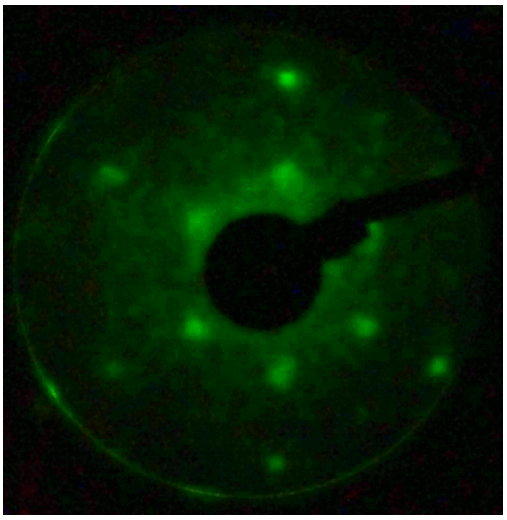


FIGURE 6.1: Hexagonal LEED pattern of the Au(111) single crystal at 100V electron energy

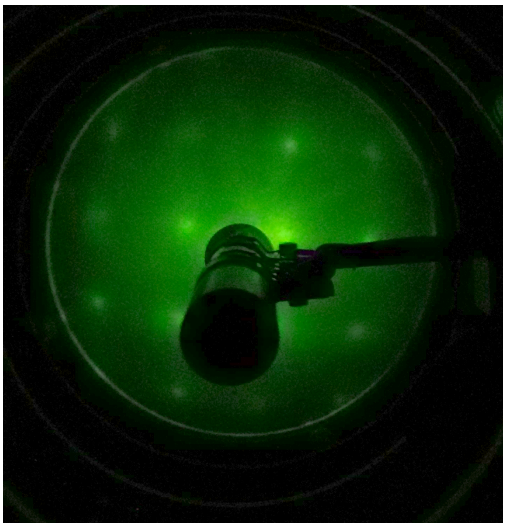


FIGURE 6.2: Square LEED pattern of the Mo(001) single crystal at 130V electron energy

temperatures more easily the oxygen chemical potential is used to describe the preparation conditions. It is calculated as follows:

$$\mu = k_B T \ln\left(\frac{p}{p_0}\right) \tag{6.1}$$

with k_B Boltzmann constant, T temperature, p oxygen partial pressure and p_0=1000 mbar.

Topographic images as well as electronic state information were gathered using the STM setup described before. Chemical information were derived using a hemispherical electron analyzer (ESCALAB 200) and a non-chromatized Mg-Kα x-ray source (see section 4.1).
This chapter will discuss the calibration of preparation parameters, such as the temperature during annealing, the deposition rate of copper, and the reference peak used to calibrate XP-spectra.

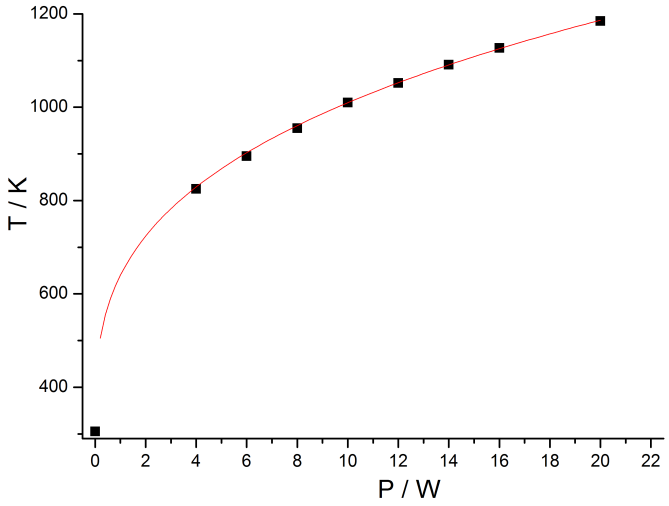
6.1 Temperature of the Heating Stage

Samples were heated using electron bombardment. Electrons are emitted from a tungsten filament and accelerated by a high voltage applied to the sample stage. From the applied voltage (up to 2 kV) and the measured emission current (several mA) the heating power $P = U \times I$ can be calculated. To relate the heating power to the sample temperature the heating stage was calibrated using the molybdenum sample. The calibration experiments could not be performed with the Au(111) directly, because its low

emissivity makes temperature measurements with a pyrometer unreliable.
Different heating powers were set and the sample temperature was monitored with an infrared pyrometer. Emissivity was set to 18% and environmental temperature to 30°C in the software. For each heating power a couple of minutes was allowed for the sample to thermalize. The data and fit are shown in Fig. 6.3.
The most likely error during experiments is that at a given heating power the sample did not reach the expected temperature probably because of the heating stage alignment.

The sample temperature (in K) can thus be calculated from the heating power (in W) by

$$T = 305 + 335\sqrt[3]{P} \tag{6.2}$$



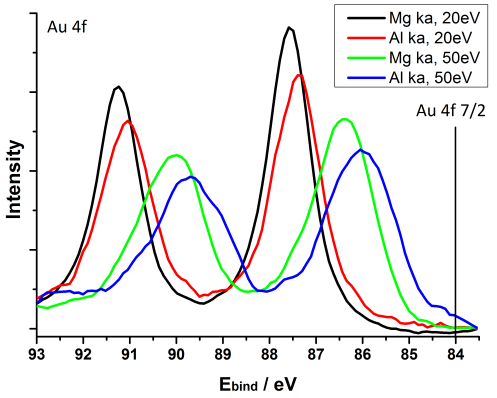
fit y = a + b × x^c

a	305
b	0.06718
c	0,323

FIGURE 6.3: Temperature as a function of heating power

6.2 XPS Energy Reference

To assess the chemical composition of the Cu+O_2 films prepared on Au and Mo substrates XP-spectra were recorded using a hemispherical electron analyser (ESCALAB 200) and non-chromatized Mg-Kα and Al-Kα x-ray sources. Measured energies were calibrated against the Au 4f line as an internal reference as shown in Fig. 6.4. Differences in measured kinetic energy depend on the x-ray source and the pass energy. Typically, measured kinetic energies are too small so calculated binding energies are too big. The resulting values for calibration are shown in Fig. 6.4.
The XPS was operated at 20 eV pass energy to ensure a good energy resolution (see 3.2.1) while still getting a reasonable intensities. The accumulation time of 1 s has been



E_{pass} / Source	Al-Kα	Mg-Kα
50 eV	-2.1 eV	-2.4 eV
20 eV	-3.4 eV	-3.6 eV

FIGURE 6.4: Measurement of Au 4f with different pass energies and x-ray sources. In all cases the resulting binding energies are too small as compared to the expected value for Au 4f 7/2 at 84 eV binding energy from NIST database [96]. This results in the corrective energies shown in the right hand table.

chosen to get a good signal to noise ratio while still keeping the measurement time manageable (around 20-30 min for one spectrum). Also the pressure in the XPS chamber had to be controlled if several consecutive spectra where taken.

6.3 Copper Evaporation Rate

Based on the calibrated XP spectra, the thickness of the Cu2O films could now be determined. For this purpose, a series of XPS measurements with different Cu evaporation times has been taken. Starting with a sputtered and annealed Au(111) single crystal copper was evaporated at a flux of 1 μA for 5 min. Before evaporation XP-spectra of Au 4f and Cu 3p which are close in energy were collected. To exclude a possible influence of the setup both X-ray sources (Mg-Kα and Al-Kα) were used. Afterwards, the film thickness was increased by subsequent 5 min evaporation steps and the respective XP spectra were taken in between. The total deposition time was set to 35 min.

As the probing depth of XPS is limited, the gold peak intensity gets attenuated with growing copper film thickness while the copper peak grows in intensity. Intensities of XP-Spectra also vary slightly between measurements probably due to differences in the sample placement or changing x-ray source intensities. After normalization of all spectra to 1, Au 4f 5/2 peaks were fitted with Gaussians. The scaled spectra can be seen in Fig. 6.5. From the Au 4f intensities the film thickness can be calculated using a simple attenuation model

$$d = -\ln\left(\frac{I}{I_0}\right) \times \lambda(E) \tag{6.3}$$

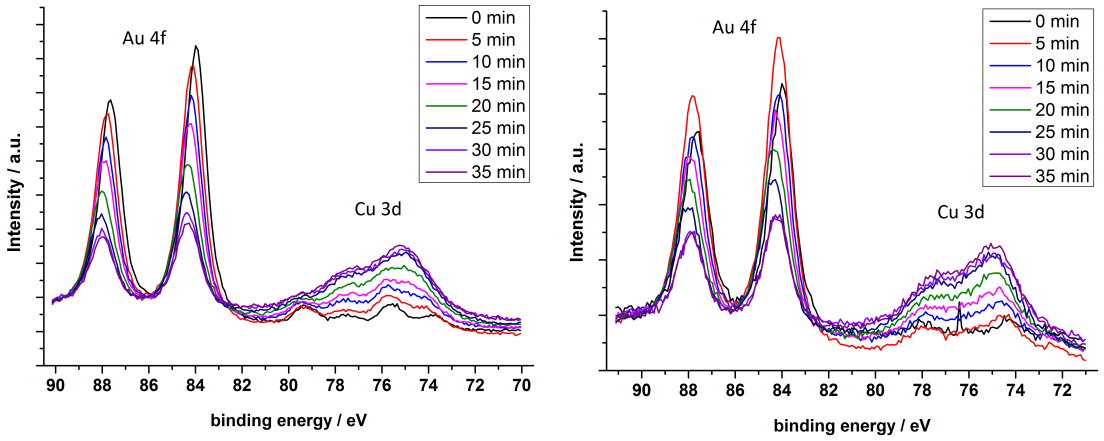


FIGURE 6.5: Au 4f and Cu 3p Xp-spectra for different Cu evaporation times collected with Mg-Kα and Al-Kα X-ray sources.

where I is the intensity (area under gauss fit) of Au 4f 5/2, I_0 corresponds to the measurement before evaporation and λ denotes the electron mean free path which depends on the x-ray energy and thus on the source used. It is 1.84 nm and 2.02 nm for Mg-Kα and Al-Kα respectively. The calculated film thickness is shown in Tab. 6.1. To get the evaporation rate a linear fit is utilized.
For the Al-Kα series the Au 4f spectrum taken after 5 minutes is higher in intensity than the spectrum taken before Cu deposition even after scaling. This results in some negative film thicknesses. However the rate of evaporation (the slope of the linear fit) remains the same and the change in film thickness Δd for both series has been determined to 2 nm within 35 min.

Assuming a linear behaviour of the flux intensities the film thickness can be calculated as

$$d = \frac{0.07\,\text{nm}}{\text{min} \times \mu\text{A}} \cdot t[\text{min}] \cdot flux[\mu\text{A}] = \frac{0.3\,\text{ML}}{\text{min} \times \mu\text{A}} \cdot t[\text{min}] \cdot flux[\mu\text{A}] \tag{6.4}$$

As calibration has been performed for bare Cu, renormalization for Cu_2O needs to be undertaken. The distance between two (111)-lattice planes is $1/2 \times \sqrt{2a^2}$ with a the lattice constant. For metallic copper the lattice constant is a=0.36 nm so 1 ML of Cu(111) is 0.26 nm thick. Thus the evaporation rate is 0.3 ML per minute at 1 μA flux. The Cu_2O unit cell is larger with a=0.43 nm but it also contains four copper atoms like the copper unit cell. Thus the same number of mono-layers is evaporated but resulting in a slightly thicker film with 0.3 nm thickness per mono-layer. All following nominal film thicknesses assume that the film is pure Cu_2O.

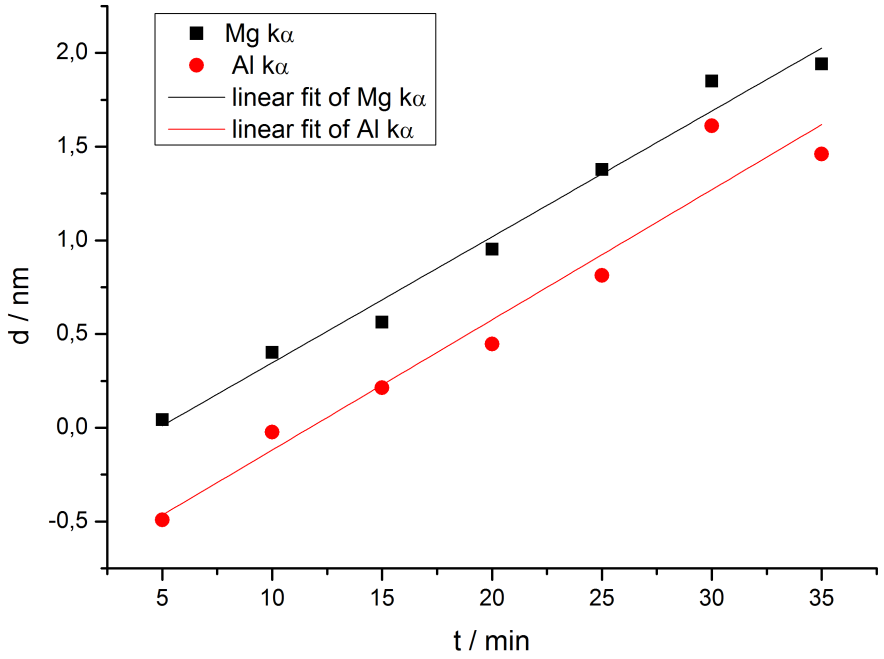


FIGURE 6.6: Film thickness depending on evaporation time and linear fit.

t / min	Mg-Kα d / nm	Al-Kα d / nm
0	0.001	0.002
5	0.043	0.165
10	0.402	1.546
15	0.563	2.165
20	0.953	3.667
25	1.378	5.301
30	1.849	7.113
35	1.941	7.466

linear fit $y = a + b \times x$

Mg-Kα	a	-0.325	$\pm$ 0.089
	b	0.067	$\pm$ 0.004
Al-Kα	a	-0.814	$\pm$ 0.160
	b	0.069	$\pm$ 0.007

TABLE 6.1: Calculated film thickness depending on evaporation time and values for linear fit.

6.4 Thin Film Annealing

To monitor the thermal stability of films during annealing a thick copper layer was evaporated and subsequently oxidized using the high pressure cell described in section 4.3. After preparation Au 4f and Cu 2p were measured using XPS. Subsequently the sample was heated for 10 min at a heating power of 1 W (640 K). The XPS measurements were repeated followed by heating for 10 min at 2 W (727 K), 4 W (837 K) and 8 W (975 K). The collected XP-spectra were again normalized to 1 and are shown in Fig. 6.7. The third measurement (for 2 W) shows less overall intensity than the fourth which could be due to bad sample placement.

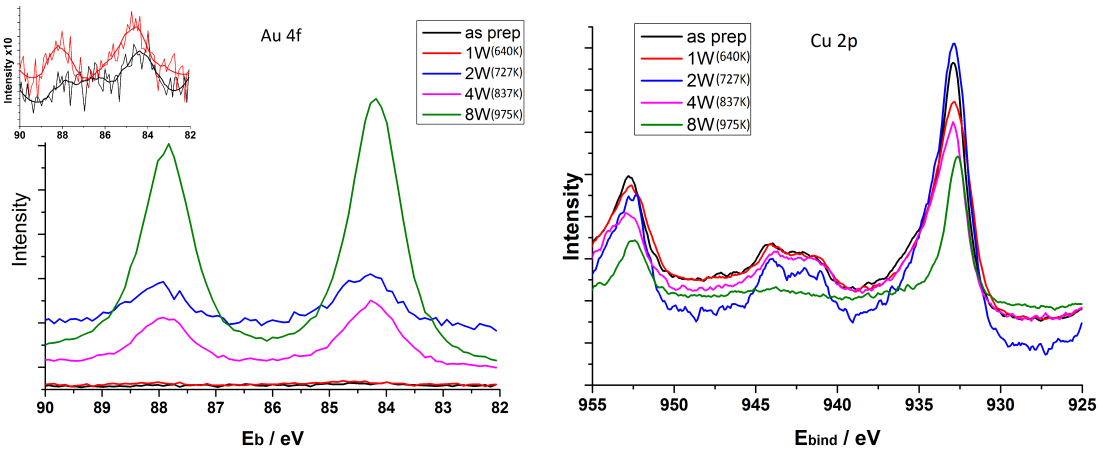


FIGURE 6.7: Au 4f and Cu 2p spectra after subsequent annealing at different temperatures, each for 10min. While little Cu intensity is lost, Au intensities start to reappear at high temperatures. CuO seems to transform into Cu_2O upon annealing, as revealed by the disappearance of the characteristic Cu 2p satellite.

In the Cu 2p line CuO was observed which seems to transform into Cu_2O upon annealing, as revealed by the disappearance of the characteristic Cu 2p satellite. Calculating the Cu_2O film thickness for each measurement from the Au intensities was done in the previous section proves challenging. While little Cu intensity is lost, Au intensities start to reappear at high temperatures. Note that the maximum temperature was 975 K at 8 W, much higher than during normal experiments (600 K-800 K). From this Cu_2O film thickness is assumed to be almost constant with only very little thinning during experiments.

Nevertheless the sample undergoes some changes at very high temperatures leading to the increase in Au signals. A desorption of Cu atoms into the gas phase or alloying of Cu atoms with the gold support are thinkable. Also dewetting of the film, exposing bare Au areas are possible. Of these alloying at medium to high temperatures and dewetting at high temperatures seem reasonable.

Chapter 7

XP Spectroscopy of Cu_2O

In this chapter the analysis of the chemical composition of the samples by X-ray photoelectron spectroscopy is discussed. Principal copper and oxygen lines (Cu 2p, Cu LMM and O 1s) were evaluated for 19 different preparations as shown in Tab. 7.2. Additionally to Au and Mo, ZnO has been used as an oxide substrate. Two samples (one on an Au and one on a ZnO substrate) were prepared by evaporating copper at UHV conditions thus resulting in a metallic copper film. Four samples were prepared in the high pressure cell (see section 4.3). Because of the higher oxygen partial pressure during annealing these samples presumably consist of a thicker cuprous oxide film than those prepared by reactive copper deposition. Furthermore five samples were held at 2 kV during copper deposition. This was done to slow down the Cu^+ ions before reaching the sample. However, it did not influence the chemical composition of the film.

From the copper flux and the evaporation time the nominal film thickness was calculated as presented in section 6.3. From the temperature and oxygen pressure during preparation the oxygen chemical potential is calculated using the formula introduced in chapter 4.3. Most samples are as-grown, while some have been annealed in UHV or O_2 after preparation. From Cu LMM kinetic energy and Cu 2p 3/2 binding energy the modified Auger parameter (see section 3.2.3) was calculated and is also shown in Tab. 7.2. For comparison entries from the NIST reference database were used. For each XPS line the mean and standard deviation from all respective entries was calculated and is shown in table 7.1.

First, the properties of the oxidized Cu films are discussed, in order to identify the nature of the produced ad-oxide. In the following, the effect of copper oxidation on the support materials is presented.

NIST	Cu 2p 3/2	Cu LMM	mod. Auger Param.	O 1s
Cu	932.61 ± 0.21	918.61 ± 0.23	1851.22 ± 0.44	
Cu_2O	932.45 ± 0.23	916.7 ± 0.30	1849.15 ± 0.53	530.52 ± 0.27
CuO	933.70 ± 0.42	917.88 ± 0.19	1851.58 ± 0.61	529.69 ± 0.37
MoO_x				530.67 ± 0.12
ZnO				530.40 ± 0.39
Cu-Au	932.42 ± 0.09			

TABLE 7.1: Mean and standard deviation of copper and oxygen XPS lines as found in the NIST database [96].

7.1 Copper and Oxygen XP-Spectra

The Cu 2p spectrum is characterized by the spin-orbit splitting of the spectrum into Cu 2p 1/2 (952 eV) and 3/2 (933 eV). For CuO additional shake-up peaks at apparent higher binding energies occur (945 eV for 2p 3/2) [19, 158]. Metallic Cu and Cu_2O are unfortunately indistinguishable in Cu 2p which occur at very similar binding energies [19, 158, 159].
Independent of the preparation conditions the Cu 2p (see Fig. 7.1) shows no shake-up satellite as would be typical for CuO. The Cu 2p 3/2 has been fitted with a Gaussian to assess the energy shift. It ranges from 933 eV to 932.25 eV matching the expected range of Cu^0 (932.61 ± 0.21) eV as well as Cu^+ (932.45 ± 0.23) eV but being about 1 eV below the expected value for Cu^{2+} (933.7 ± 0.42) eV [96] in agreement with the absence of satellite peaks.

The principal oxygen line O 1s was also measured and fitted with a Gaussian. Independent of preparation, support and film thickness the measured binding energy is in the range of 530.2 eV to 530.9 eV as shown in Fig. 7.1. However, identifying the oxygen containing phases is not always possible from the O 1s spectrum alone as the support may

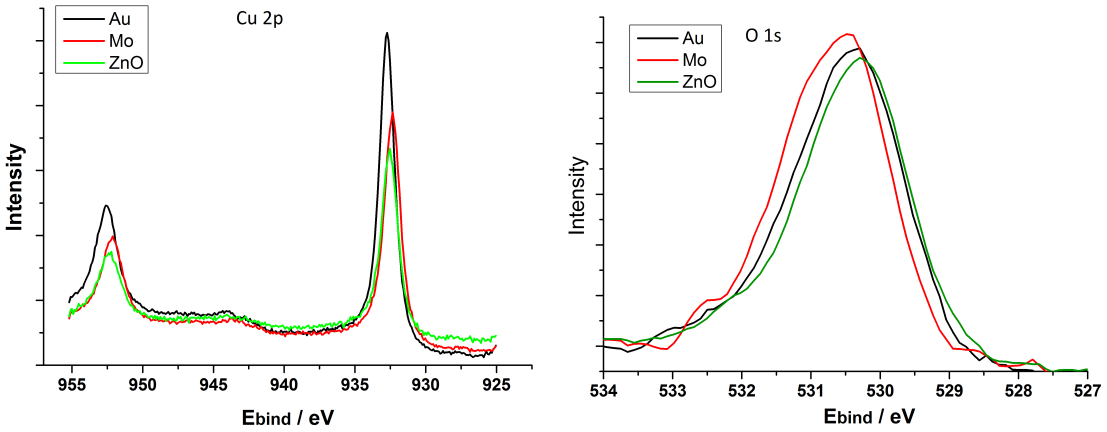


FIGURE 7.1: Cu 2p and O 1s spectra for three substrates after reactive copper deposition. Cu 2p shows no satellite and only little shift in binding energy between different samples.

Date	Substrate	T / K	p_{O2} / mbar	μ_{O2} / eV	d / nm	d / ML	O 1s	Cu 2p 3/2	Cu LMM	Line Shape	mod.AP	Notes
13.01.2015	Au	295	2.50E-06	-0.50	2.7	9	530.58	932.91	918.92	metallic	1851.83	
14.01.2015	Au	375	1.00E-08	-0.82	2.7	9	530.68	932.86	918.89	metallic	1851.74	annealed UHV (filament)
10.02.2015	Mo	295	6.00E-06	-0.48	1.8	6	530.69	932.87	918.77	metallic	1851.65	
13.05.2015	Au	788	1.50E-06	-1.38	≤ 1.8	≤ 6	530.69	932.62	918.56	thin	1851.17	annealed O2 10min
28.05.2015 A	Au	425	5.00E-06	-0.7	1.8	6	530.5	932.75	918.95	metallic	1851.7	
28.05.2015 B	Au	725	1.00E-08	-1.58	≤ 1.8	≤ 6	530.36	932.77	918.84	metallic	1851.61	anealed UHV 3min
29.05.2015	Au	295	1.00E-08	-0.64	1.8	6	530.29	932.45	918.94	metallic	1851.39	Cu (no O_2)
09.06.2015	Au	425	5.00E-06	-0.7	0.18	0.6	530.4	932.65	918.42	thin	1851.07	2 kV
11.06.2015	Au	425	1.00E-06	-0.76	0.4	1.32	530.39	932.68	918.43	thin	1851.11	2 kV
12.06.2015	Mo	425	1.00E-06	-0.76	0.36	1.2	530.9	932.38	918.57	metallic	1850.95	2 kV
16.06.2015 A	Mo	295	5.00E-06	-0.49	0.72	2.4	530.4	932.49	918.74	metallic	1851.23	2 kV
16.06.2015 B	Mo	837	5.00E-06	-1.38	0.36	1.2	530.54	932.5	918.81	thin	1851.31	2 kV
17.06.2015	Mo	425	9.00E-06	-0.68	0.18	0.6	530.71	932.49	918.68	metallic	1851.17	
18.08.2015	ZnO	295	1.00E-08	-0.64	0.9	3	530.39	932.93	918.58	metallic	1851.51	Cu (no O_2)
26.08.2015	ZnO	425	8.00E-06	-0.68	0.9	3	530.4	932.57	918.62	metallic	1851.19	
29.09.2015 A	ZnO	525	0.1	-0.42	1.39	4.5	530.73	932.94	916.63	thick	1849.57	HPC
(07.10.2015)		568	4	-0.27								HPC
(07.10.2015)		837	1.00E-08	-1.83								annealed UHV 20min
07.10.2015	ZnO	975	1.00E-08	-2.13	1.8	≤ 6	530.42	932.68	918.75	thin	1851.43	annealed UHV 20min
08.10.2015	ZnO	640	5	-0.29	1.8	6	530.63	932.9	916.5	thick	1849.4	HPC
13.10.2015	Au	551	1.6	-0.31	1.8	6	530.4	932.94	916.48	thick	1849.42	HPC

TABLE 7.2: Table of preparations and XPS peak positions with T Temperature, p_{O2} oxygen partial pressure, μ oxygen chemical potential, d nominal film thickness, Cu LMM line shape and modified Auger Parameter. Most samples are as-grown, while some have been annealed in UHV or O_2 after preparation.

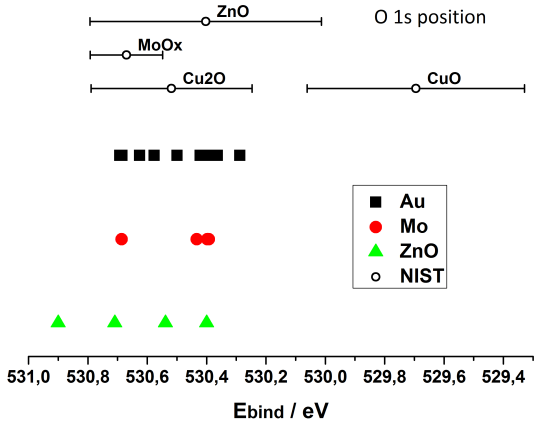


FIGURE 7.2: O 1s peak positions for different substrates and comparison with literature references [96]. Distinction of oxygen species in Cu_2O, MoO_x and ZnO is not possible from O 1s alone. Again CuO can be ruled out.

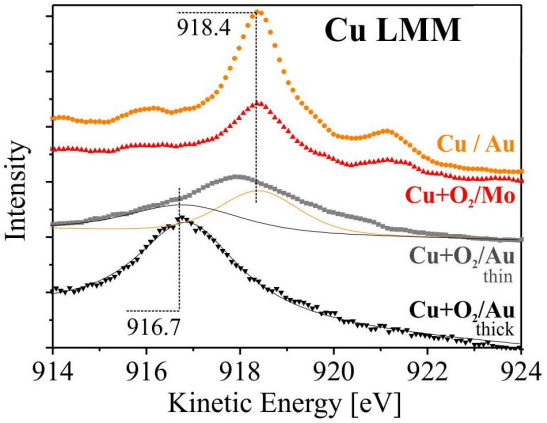


FIGURE 7.3: Three distinct kinetic energies are found for Cu LMM representing metallic Cu, thin Cu_2O and thick Cu_2O. While the results for metallic Cu and thick Cu_2O match the expectations, the unusual thin Cu_2O LMM spectrum can be explained as a convolution of metallic Cu and Cu_2O. [160]

contain oxygen as well after preparation. Unfortunately the literature values for oxygen in Cu_2O (530.52 ± 0.27) eV, ZnO (530.4 ± 0.39) eV and molybdenum oxide (MoO_x at (530.67 ± 0.12) eV are all very close (see Fig. 7.2). Again the presence of CuO can be ruled out as the expected energy range for oxygen in CuO (529.69 ± 0.37) eV is not met by the data (530.3 eV to 530.9 eV).

Because the oxygen uptake of gold should be negligible given its chemically inert nature (as also indicated by the unchanged Au 4f spectra after deposition, as seen in the next section) and the characteristic satellites in the Cu 2p line are absent, the formation of Cu_2O is the most feasible in the $Cu+O_2$ on Au(111) system. Likewise the ZnO support shows no changes in the Zn 3p spectrum during reactive copper deposition. With the results from the Cu 2p and LMM spectra Cu_2O on ZnO seems reasonable as well. For the $Cu+O_2$ on Mo(001) system any presence of copper oxides are unlikely from the shape and position of the measured Auger line. Moreover, the Mo 3d shows significant signs of oxidation after reactive copper deposition.

With this in mind the O 1s peaks acquired for Cu+O/Au, Cu+O/ZnO and Cu+O/Mo have to be interpreted differently. While the first relates to the oxygen contained in Cu_2O, for the second both the oxygen in ZnO and Cu_2O is detected while for the third it shows the oxygen within MoO_x compounds.

Cu LMM spectra are better suited to determine the nature of the prepared Cu oxide phases[19, 20]. Three preparation schemes with different Cu LMM spectra were examined (see Fig. 7.3). Unfortunately Au 4d 5/2 (binding energy 335 eV) when excited with Mg-Kα X-rays yields a kinetic energy of 918 eV similar to the one of Cu LMM. However

all LMM spectra where measured on molybdenum and zinc oxide substrates as well, ruling out a possible miss-interpretation of the spectra.
A reference spectrum for all the oxide spectra discussed below has been obtained by dosing pure Cu in UHV conditions. The resulting shape of the Cu LMM Auger line, one central peak at 918.5 eV and two shoulders at 916 eV and 921 eV, matches the shape [20, 97, 99] and position of Cu^0 (918.61 ± 0.23) eV [96]).
To reach the fully oxidized state of Cu, samples have been prepared in the HPC, presumably yielding thick oxide films because of a more complete oxidation (nominal film thickness of 10 ML). The corresponding spectrum (Fig. 7.3, black curve) shows a single peak at 916.5 eV which matches the literature values for Cu_2O (916.7 ± 0.3) eV [20, 96, 161].
Upon reactive copper deposition in 10 - 5 mbar of oxygen on the Au(111) crystal a third LMM spectrum, showing a single maximum at 917 eV, was obtained. The position would match CuO (917.88 ± 0.19) eV but the presence of CuO was already excluded from the absence of satellites in the Cu 2p spectra.
However, the oxide thin-film spectrum can be de-convoluted into two Gaussians at 916.7 eV and 918.5 eV matching Cu_2O and Cu^0 respectively [162]. This suggests that copper gets only partly oxidized on the gold support. The metallic copper is assumed to be located at the metal / oxide interface covered with Cu_2O as supported by earlier experimental studies [1, 11, 12] as well as recent DFT calculations [163]. The latter shows the Cu_2O/Au(111) interface to be instable with an oxygen depleted copper layer emerging at the interface. In the thick oxide films on Au(111), prepared in the HPC, the interfacial Cu^0 gets strongly attenuated.
When the same reactive copper deposition is done on the molybdenum support the results look very different, as shown in Fig. 7.3 (red curve). The overall shape and position of the Auger spectrum resembles that of metallic copper on gold even for as-grown Cu+O on Mo(001) with no further post annealing. Thus no Cu oxidation seems to occur on the Mo surface, as proven in section 7.2.

Further information on the nature of the different Cu_2O films comes from the Wagner plot, as introduced in section 3.2.3. The Wagner plot of the data is compared to reference values in Fig. 7.4. Overall Cu LMM kinetic energies show very little shift (≈ 0.5 eV) except for those samples prepared in the HPC which are about 2 eV lower in kinetic energy. Most of the data seem to match metallic copper. Again the presence of CuO in the samples can be excluded.
Still, formation of ultra thin Cu_2O layers on the different substrates is unambiguously proven by the STM data in chapter 8.

As already explained, from the Cu LMM shape the oxide layer is assumed to be very thin with a metallic copper layer at the interface to the substrate, which is also supported by DFT calculations. Apparently, the Cu_2O layer is too thin to significantly change

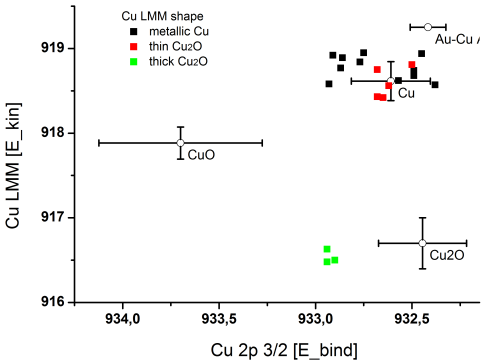


FIGURE 7.4: Wagner plot of own Cu-O data with references from NIST database [96]. For Au-Cu alloy no data on the Cu LMM kinetic energy could be found in literature. Samples prepared in the HPC are closest to bulk Cu_2O. Formation of CuO can be excluded at the preparation conditions.

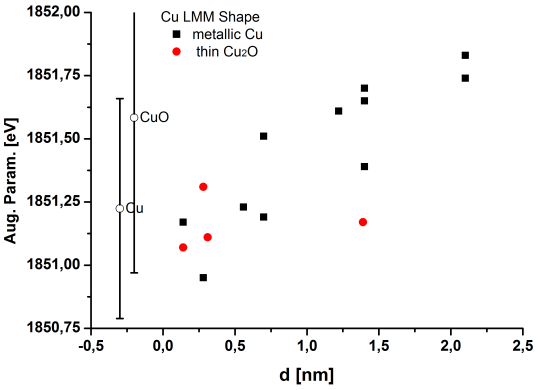


FIGURE 7.5: Observed shift of modified Auger parameter depending on calculated nominal film thickness d showing the influence of the thin film nature on XPS measurements. Thick oxide samples (prepared in the HPC) are omitted from the plot.

the Cu LMM kinetic and Cu 2p binding energies, so that all preparations (except for those from the HPC) fall within the expected range of Cu^0 in the Wagner plot. Also, as shown previously (see chapter 6.4) changes in the Cu_2O film occur during annealing. While a clear increase in Au intensity was observed, nearly no Cu signal was lost during annealing. As Cu and Au are known to alloy, it is possible that some amount of Cu disperses into the bulk while annealing, creating a Cu^0 signal without coming from the Cu_2O layer. Finally, if there are mono-layer Cu_2O films without a Cu interface layer, the Cu 2p and Cu LMM signals could differ considerably from the bulk signal. Nevertheless, the formation of Cu_2O thin films becomes clear from the STM experiments discussed later in chapter 8. The samples prepared in the HPC are, on the other hand, close to the reference values for Cu_2O to safely assume that they comprise thick Cu_2O films.

In the following paragraph, the influence of several preparation parameters, such as temperature, pressure and film thickness on the XP and Auger spectra of the Cu+O preparations is discussed. The differences are small in all cases, as expected from the overall similarity of Cu^0 and Cu^+ spectra, however some trends can be seen. Plotting the modified Auger parameter over the nominal film thickness in Fig. 7.5 shows a shift of about 0.75 eV to higher kinetic energies with increasing film thickness from 0.2 nm to 3 nm. This can be explained with the different chemical environment of surface and interface atoms and the higher portion of surface and interface atoms in thin as compared to thick films [95]. This also confirms that the thin film nature of the samples has a noticeable influence on the XP spectra thus making a comparison to values acquired on bulk samples arguable.

Figure 7.6 shows the Wagner plot according to the different substrates used. As already discussed, the samples fall into two groups: For all samples prepared in the HPC, the measured position in the Wagner plot is in good agreement with the bulk data reported for Cu_2O. All samples prepared by reactive copper deposition in the preparation chamber are within the error bars characteristic for Cu^0. Both Cu LMM and Cu 2p energies vary only by 0.5 eV. Still, a separation of Cu 2p binding energies according to the substrate used was found. On Au(111) Cu 2p binding energies tend to be higher (932.6 eV to 923.9 eV) than on Mo(001) (932.38 eV to 932.5 eV). As seen before, the former yields Cu_2O/Au while the latter results in Cu/MoO_x because of the oxidizing effect of the support. The Cu^+ ions in Cu_2O should bind the negative electrons more tightly, resulting in a larger binding energy, thus fitting the results. But still the variations are so small, that a distinction between Cu^+ and Cu^0 from the Cu 2p spectrum alone is not reliable. Two samples were prepared in UHV conditions, using the Au and the ZnO support. Again, while the difference in Cu 2p binding energy is minimal, the Cu film on the gold substrate shows a smaller binding energy than on the ZnO substrate. This might point to an oxidation of Cu with the oxygen from the substrate, thus reducing ZnO in the process. However, this effect is not very pronounced.

The influence of temperature and oxygen pressure (and hence oxygen chemical potential) during preparation on the overall chemical composition of the samples is shown in figs 7.7, 7.8 and 7.9. The only significant change in the overall chemical composition of the Cu+O films could be achieved by preparations in the HPC. These oxide films are presumably thicker, with less metallic copper at the oxide/substrate interface due to a more complete oxidation at the higher oxygen pressure and sample temperature. All films prepared by reactive oxygen deposition in the preparation chamber show a strong Cu^0 signal, likely from a metallic layer at the oxide/substrate interface, thus subduing the Cu_2O signal of the very thin oxide layer. Also the ultra-thin nature of the Cu_2O layers may result in a shift with respect to the bulk oxide thereby producing the Cu^0 like signals in presumably oxidized films.
Different temperatures during reactive copper deposition or annealing in the preparation chamber had little effect on the Auger and XPS results as long as the oxygen pressures stayed below 10^-6 mbar. However, a recent master thesis [128] shows that a strong temperature dependence for preparations at higher oxygen pressures is found.
One sample that was prepared in the HPC yielded Cu^0-like characteristics after prolonged annealing at elevated temperatures (837 K for 20 min followed by 975 K for 20 min). This might be due to film thinning (Cu-Au alloying at the interface), or reduction of the Cu_2O film (loss of oxygen at the Cu_2O surface).

Concluding, the only significant change to the overall chemical composition of Cu+O films was made by preparations in the HPC, yielding a more complete oxidation and

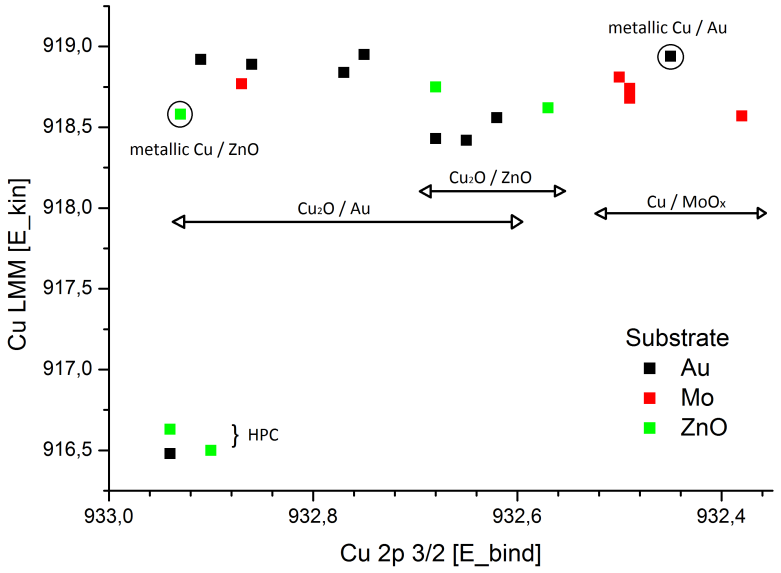


FIGURE 7.6: Disregarding the preparations in the HPC, clear distinctions between the substrates can be seen in the Cu 2p binding energy. Exemption are metallic Cu films for the Au and ZnO substrates.

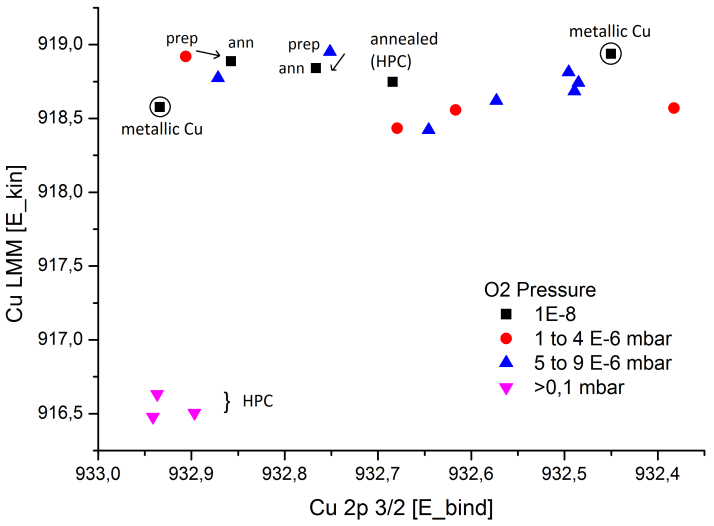


FIGURE 7.7: The O_2 pressure in the HPC ($\geq$0.1 mbar) leads to a shift in Cu LMM kinetic energies as opposed to 1×10^{-6} to 9×10^{-6} reached in the preparation chamber. Substrates used can be seen from Fig. 7.6.

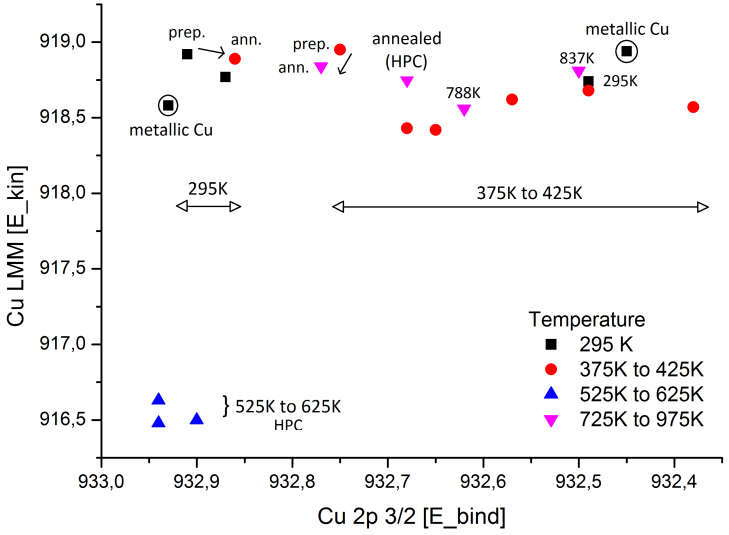


FIGURE 7.8: Influence of the temperature on the Cu_2O thin film preparation. Generally temperatures in the HPC were higher than during reactive copper deposition. However during annealing higher temperatures are possible in the preparation chamber.

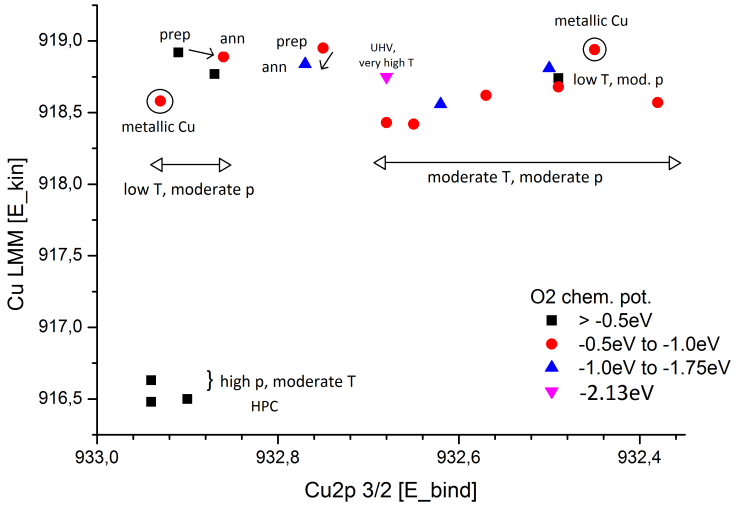


FIGURE 7.9: Distribution of O_2 chemical potential among the preparations.

thus thicker Cu_2O films. The overall chemical composition of Cu+O films produced by reactive copper deposition does not change much within the temperature and oxygen pressures reached in the preparation chamber. Still, hard to overlook changes in the XP-spectra of the substrates (Au, Mo, ZnO) and the oxygen 1s line lead to the discovery of very thin Cu_2O films on the ZnO and Au(111) samples (as supported by the STM data) while the molybdenum support was found to oxidise itself while Cu stays in its metallic form. and lead to the deposition of metallic Cu^0.

7.2 Changes of the support during reactive Cu deposition

Finally, the effect of copper oxidation on the support materials was analysed. Therefore, XPS spectra of the respective samples were taken before and after reactive copper deposition. The Au 4f spectra shows no shift as expected from the chemical inertness of bulk gold. Likewise the Zn 3p shows no changes during reactive copper deposition suggesting an unchanged ZnO support during the preparation.

On the other hand Mo 3d core levels (shown in Fig. 7.10) developed a high energy shoulder at 229 eV after reactive copper deposition in addition to the main binding energy for bulk molybdenum at 227.7 eV as measured on the cleaned molybdenum crystal. The binding energy of this new component matches the values for molybdenum oxide expected at (229.72 ± 0.85) eV for MoO_2 and at (232.77 ± 0.33) eV for MoO_3 [96]. Most likely a molybdenum oxide film develops at the topmost layers during Cu deposition in an oxygen environment whose thickness can be estimated from a simple attenuation model to be ≈ 2 ML.

Apparently, Au and ZnO are inert supports for the preparation of Cu oxide films while Mo competes with the Cu for oxygen molecules from the gas phase. Mo seems therefore less suited to grow Cu_2O films and indeed the ad-copper remains metallic in this specific case, as discussed in section 7.1.

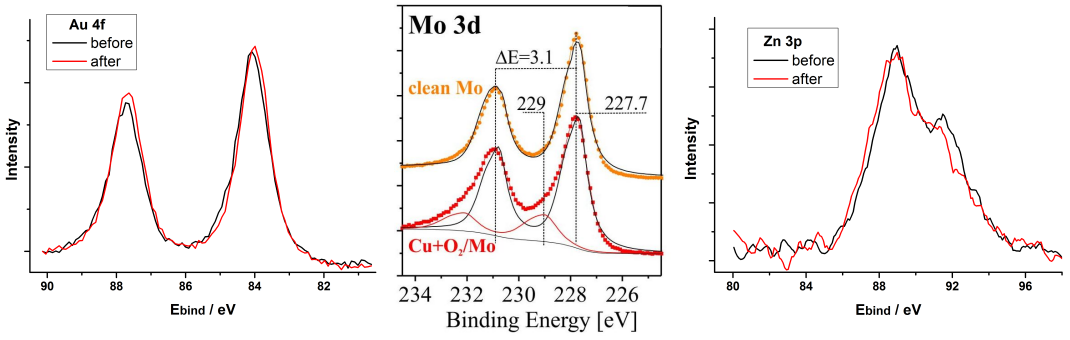


FIGURE 7.10: XPS lines for Au, Mo and ZnO substrates before and after reactive copper deposition. Whereas Au and ZnO remain largely unchanged Mo develops a high energy shoulder from MoO_x formation. For the latter, the two Mo phases were fitted with an asymmetric Doniach Sunjic function, after removing a Shirley background [160].

Chapter 8

Cu_2O-films on Au(111)

8.1 Gold substrate

Gold has been chosen as the substrate to prepare the Cu_2O film because it is known for its chemical inertness thus oxidation of the gold crystal during preparation in oxygen atmosphere should be minimal. Moreover $Cu_2O(111)$ has been shown to be easily reduced when in contact with any metal support with the exception of gold [52]. So in this combination both the support and the oxide film are expected to be chemically stable. Furthermore the atomic distances in gold are in close match to the Cu-Cu distance in Cu_2O thus it should serve as a growth template with minimal strain in the oxide film.
Gold crystallizes in a face-centred cubic lattice with a unit cell length of 4.07 Å and four atoms with 2.88 Å next neighbour distance. So the hexagonal Au(111) surface features 2.88 Å periodicity and 60° symmetry angle. The also hexagonal $Cu_2O(111)$ surface shows a periodicity of 6.04 Å, twice as large as the gold cell. Thus the oxide unit cell is 4.8% larger than a (2×2) gold unit cell. Placing $Cu_2O(111)$ directly onto Au(111) as seen in fig.8.1 results in a coincidence lattice of (7×7) $Cu_2O(111)$ unit cells on (15×15) Au(111) unit cells.
However this is not necessarily what happens. Serving as a growth template, the smaller atom periodicity of the gold surface could lead to a distortion of the Cu_2O. This in turn results in stress within the Cu_2O lattice which can be reduced by the insertion of dislocation lines.

Other than most noble metals the Au(111) surface shows a distinct surface reconstruction which reduces the surface energy by about 25 meV per surface atom [69, 164, 165] In this surface structure the atoms along the $< 1\bar{1}0 >$ direction are compressed by 4.38% [165] to a distance of 2.75Å between atoms. This results in a superstructure where 23 surface atoms fit on top of 22 atoms in the lower layer as seen in Fig. 8.2.

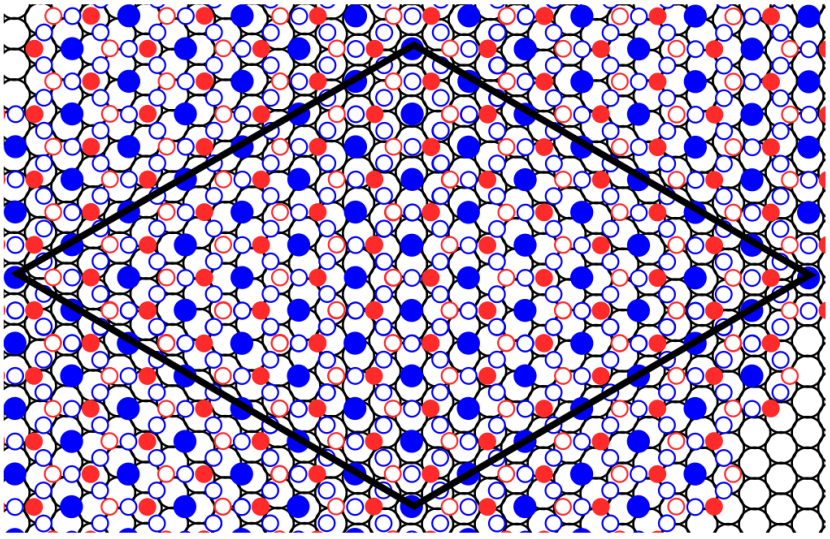


FIGURE 8.1: $Cu_2O(111)$ on Au(111) coincidence lattice. blue solid: Cu_{cus}, blue hollow: Cu_{csa}, red solid: O_{cus}, red hollow: O_{csa}

The compression leads to a slight buckling in the topmost layer resulting in ridges which are clearly visible in STM images of clean Au(111) surfaces as shown in Fig. 8.2. With the three-fold rotational symmetry of the (111)-surface the ridges form a pattern that looks like herringbones, explaining the common name for this surface reconstruction. The ridges also separate fcc from thermodynamically less favourable hcp positions in the topmost surface layer (see Fig. 8.2). The different regions therefore give rise to spatially variable adsorption behaviour of ad-particles and ad-layers on the Au(111) surface. The reconstructed surface is a challenge for density functional theories. Most DFT calculations therefore assume the Au(111) surface to be a perfect fcc surface. Spectroscopic STM measurements [164, 166] are capable of showing the well-know Shockley-surface state onset around -460 meV for all regions of the herringbone reconstruction as seen in Fig. 8.2.

If the surface free energy of a deposited film, such as Cu_2O is lower than the reconstructed gold surface, a wetting oxide layer will develop. The dangling bonds of the gold surface are then saturated by the new bonds between oxide and gold. Depending on the atomic arrangement of the oxide film the topmost gold atoms could rearrange slightly. Sometimes, even a complete lift of the herringbone reconstruction is observed. However, given the thermodynamically less favourable hcp positions can lower their energy more, they will probably be covered with oxide first, thus serving as a growth template in the Au[112] direction.

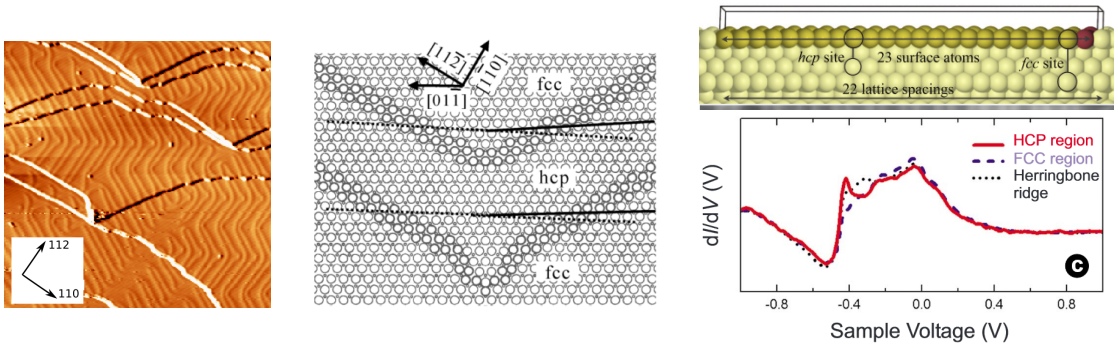


FIGURE 8.2: Herringbone-type surface reconstruction of Au(111). Topographic image (40×40) nm^2 1.15 V bias voltage, schematic top [167] and side [165] view as well as Shokley-type surface states [166].

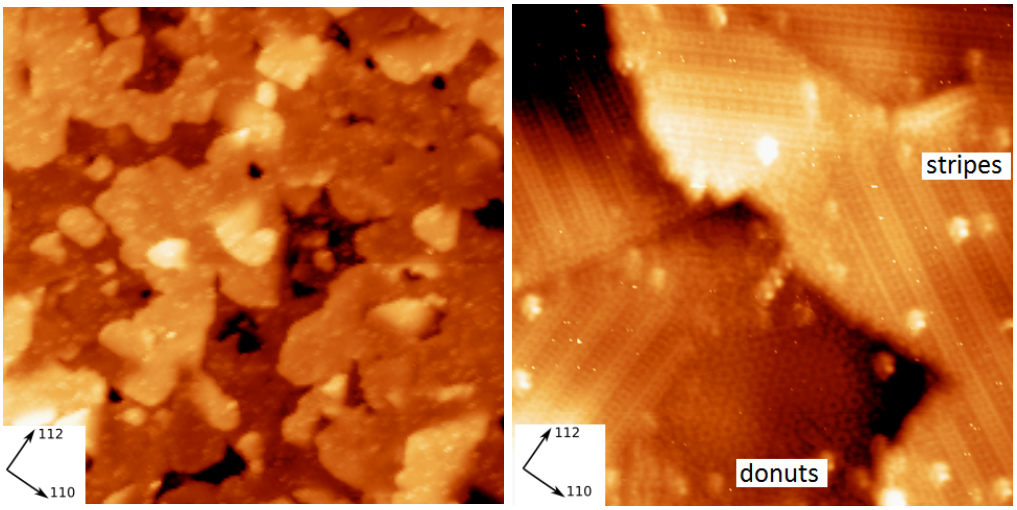
8.2 Structure and Morphology of the Cu_2O adlayer

Insight into the structure and morphology of the copper oxide thin films comes mostly from STM topographic images. Independent of the exact preparation conditions a flat, homogeneous film with an almost perfect layer-by-layer growth develops. The roughness for as-grown films is about 0.5 nm and drops to 0.2 nm in the case of post-annealed films. According to the evaporation rate calculated in section 6.3 as-grown films are generally about 1,4 nm (≈7 ML) thick. Film thickness after annealing is reduced to (0.2-1) nm (≈ 1-4 ML). Examples for as-grown films are shown in Fig. 8.3 and those for annealed films in Fig. 8.4.

8.2.1 As-Grown Films

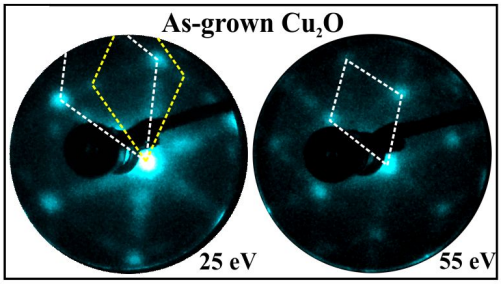
In the as-grown films two predominant surface terminations are found: Stripes along the Au[112] direction and donut-shaped six-membered rings. Domains are generally of 50-100 Å in size, delimited by step edges or domain boundaries as seen in Fig. 8.3a.

The first type is called the "stripe[112] phase" seen in Fig. 8.3d. It comprises a uniaxial pattern which aligns with one of the equivalent Au[112] directions and therefore appears in three rotational domains. Inside the stripes a rectangular unit cell can be discerned. It features a short vector parallel to Au[112] ($a1$=6 Å) and an orthogonal vector equivalent to the stripe width. The stripe width shows slight variations for different preparations but also within one sample. Most values are within a narrow range of 13-15 Å which seems close to the distances between neighbouring ridges of the herringbone reconstruction serving as a growth template. The rectangular unit cell could also be an indicator for a Cu_2O(110) based structure. The second phase is called "donut phase" due to its

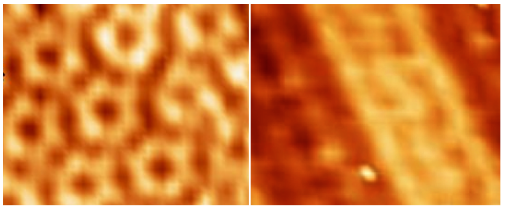


(A) $(150\times150)\,nm^2$ at 100 mV

(B) $(30\times30)\,nm^2$ at 270 mV



(C) LEED images [168]

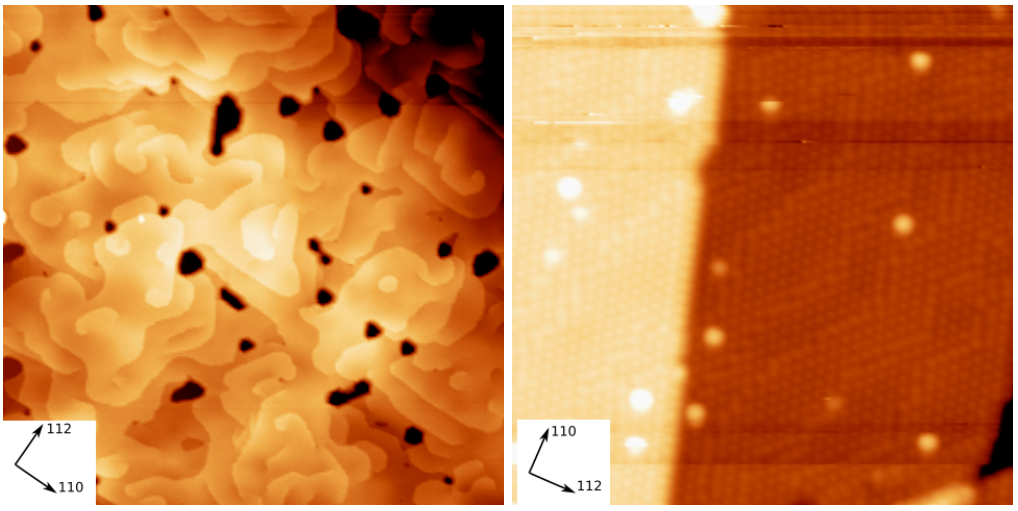


(D) Detail from (B) of donut ($(3.5\times4)\,nm^2$) and stripes [112] ($(2.5\times3)\,nm^2$) structure

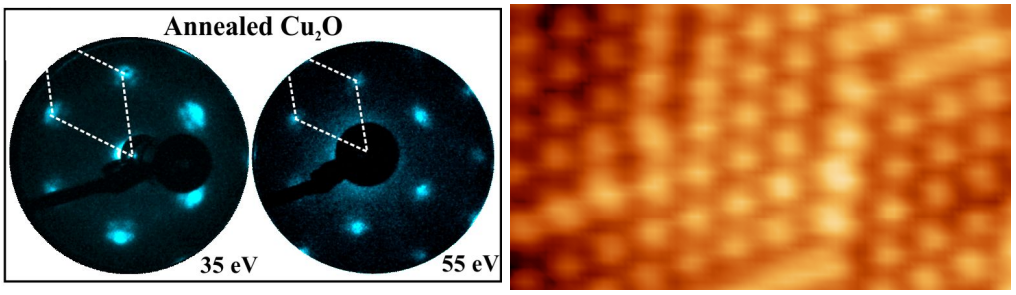
FIGURE 8.3: As-grown Cu_2O film (A) exhibiting the donut phase and stripes along the Au[112] direction (B) as well as corresponding LEED image (C) and atomically resolved details of both as-grown phases (D).

distinct six-membered rings shown in Fig. 8.3d. The donut-shaped rings form a hexagonal pattern with 12.5 Å periodicity. The axes of this hexagonal pattern connecting the centres of the donuts are rotated by approximately 18° with respect to Au[112].

Evaluation of LEED-images of as grown films (see Fig. 8.3c) show signatures of both phases stripes and donuts. The main hexagon at 25 eV and 55 eV can be assigned to the stripe phase with the connecting lines reflecting the 1d nature of this surface structure. The three-fold symmetry reflects the three rotational domains. The rectangular unit cell of the [112] stripes, seen in STM, does not produce a clear LEED signature, most likely due to the relatively large size and a limited long range.
An additional fainter hexagon is found on both sides of the fundamental spots rotated by ±20°. The donut phase is indeed a minority phase as judged from STM images and is also rotated by about the same amount. The atom spacing in the donut phase is larger than in the stripe [112] phase which results in smaller rings in reciprocal space.



(A) $(300\times300)\,nm^2$ at 450 mV (B) $(25\times25)\,nm^2$ at 1.2 V



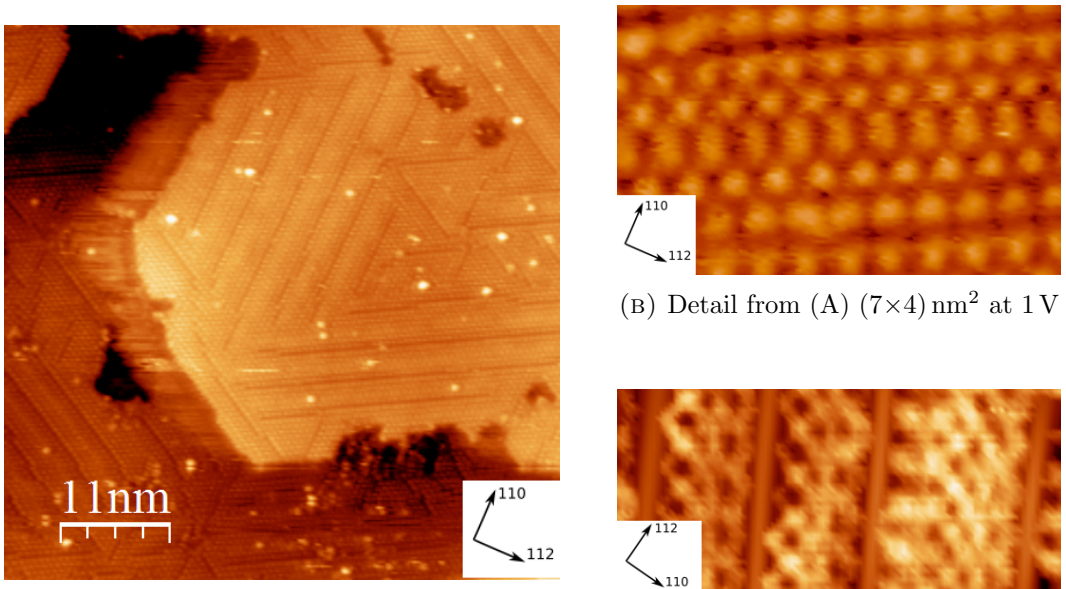
(C) LEED images [168] (D) Detail from (B) ($(6\times4)\,nm^2$)

FIGURE 8.4: Post-annealed Cu_2O film (A) exhibiting the hexagonal phase (B) as well as respective LEED image (C) and atomically resolved detail of the hexagonal phase (D).

8.2.2 Post-Annealed Films

After annealing at 650 K or higher in oxygen pressures ranging from 1×10^{-6} to 1×10^{-8} mbar a unique high-temperature phase (Fig. 8.4) develops on most samples. The annealed films are mostly flat and homogeneous, again different surface structures were found. The most common one shows a hexagonal atomic pattern and is therefore called the "hexagonal phase" but also different versions of stripes along Au[110] were found.

The hexagonal phase is characterized by wide terraces arranged around screw dislocations as typical for layer-by-layer growth. The inner structure of the terraces shows elongated domains of up to 200 Å length and 25-35 Å width with the dividing boundaries following a characteristic zig-zag pattern with the mean orientation along the Au[112] or equivalent directions.
Inside the domains a hexagonal arrangement of maxima with 0.1 Å height and 6 Å lattice constant is present. The apparent lattice registry inverts when crossing a domain boundary such that an integer position shifts to a half-order one and vice versa. This is a typical behaviour for antiphase boundaries which are commonly inserted to compensate



(A) (55×55) nm^2 at 1 V

(B) Detail from (A) (7×4) nm^2 at 1 V

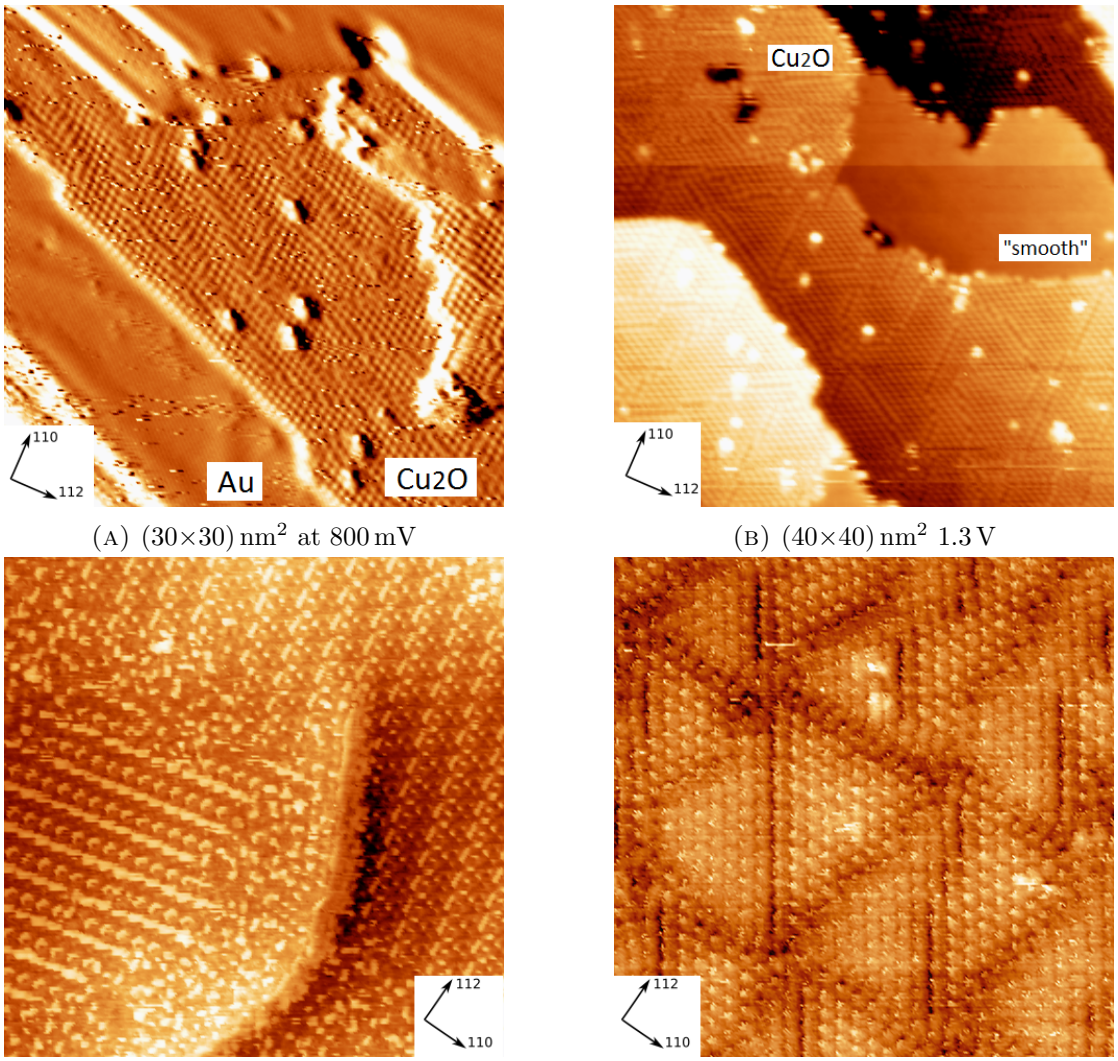
(C) (6×3) nm^2 at -500 mV

FIGURE 8.5: Stripe [110] phase as observed in annealed films. (A) and (B) show the first [110] stripe version, (C) shows a second version of the [110] stripes.

for lattice mismatch between the support and a thin film. The LEED measurement of the hexagonal phase shows a single hexagonal pattern reflecting the atom arrangement in real space. Some Cu-Au alloying might contribute to the distinct LEED pattern of the annealed films.

The second phase is again a stripe phase but this time oriented along the Au[110] direction as presented in Fig. 8.5. Similar to the low temperature stripe phase it appears in three rotational domains and with varying stripe widths. The unit cell is rectangular with a size of approximately 6 Å by 30 Å inside which a hexagonal atomic arrangement can be discerned. In some cases more complex atomic arrangements which depend sensitively on the actual imaging characteristics of the tip were found within the stripe phase. An example is shown in Fig. 8.6c. Furthermore after heating at moderate temperatures triangular domains with hexagonal atomic arrangement were found. They commonly appeared alongside with the striped phase in the same preparation. Annealing at elevated temperatures or for prolonged time resulted in the reappearance of domains with the herringbone reconstruction. Moreover, seemingly corrugation free, so-called "smooth" areas appear as seen in Fig. 8.6b. Both findings suggest that the oxygen has evaporated from the surface, leaving behind a clean Cu film or the bare Au(111) substrate.

To understand the observed surface structures DFT calculations on the stability of different $Cu_2O(111)/Au(111)$ surface configurations were carried by our collaborators from CNRS-Sorbonne University in Paris, Claudine Noguera and Jacek Goniakowsi.



(A) $(30\times30)\,nm^2$ at 800 mV

(B) $(40\times40)\,nm^2$ 1.3 V

(C) $(20\times20)\,nm^2$ at 780 mV

(D) $(15\times15)\,nm^2$ at 650 mV

FIGURE 8.6: Different surface structures on post-annealed Cu_2O film. (A) herringbone reconstruction coexisting with hexagonal Cu_2O, (B) smooth areas also coexisting with hexagonal Cu_2O, (C) stripes with complex atomic arrangement and (D) triangular domains.

From the theoretical insight and the topographic STM images structure models for five different surface structures were obtained: hexagonal phase, stripes [110] I and II, stripes[112] and the donut phase. Additionally differential conductance spectra and dI/dV maps were measured with the STM and compared to the calculated LDOS.
The hexagonal phase will be presented first, as it is the most bulk-like and therefore the easiest to understand.

8.3 Hexagonal Phase

After post-annealing to 650 K the films are possibly closest to thermodynamic equilibrium. As already seen from LEED and STM topographic images annealed films show a long range order with hexagonal symmetry and 6 Å spacing. To derive an atomic structure from the experimental findings atoms with 6 Å periodicity from the $Cu_2O(111)$ surface have to be identified. These are Cu_{cus}, O_{csa} and O_{cus} whereas Cu_{csa} shows smaller periodicity. Because of the different sites in the $Cu_2O(111)$ surface that could match the observed hexagonal pattern different models are possible. Insight into the origin of the STM contrast comes from theoretical analysis of surface stability, which will be discussed in the following section.

8.3.1 Theoretical Stability Calculations

The (1×1)-$Cu_2O(111)$ surface has already been explored on bulk samples [18, 169] as well as ultra-thin metal-supported films [26, 168]. The hexagonal pattern with 6 Å periodicity observed in STM fits both Cu_{cus} and O_{cus} thus making experimentalists unable to differentiate between a non-polar stoichiometric (both kinds of atoms being present) and a polar Cu-deficient (only O_{cus} present) surface termination. Models based on either film termination have been proposed [5, 170].
From earlier calculations both GGA and GGA+U predict the polar Cu-deficient surface termination to be preferred over the entire range of relevant O_2 chemical potentials for a very thin Cu_2O film [4, 5, 171]. Because in this termination the Cu_{cus} are missing, the observed STM contrast is suggested to arise solely from the outermost O_{cus} thus being a geometrical feature.

Theoretical calculations to better understand the stability and electronic characteristics of the $Cu_2O(111)$ surface have been done by using the DFT framework implemented in VASP [172]. Additionally to the standard GGA (PW91) [173] also the hybrid (HSE06) [174] approximation to the exchange-correlation function has been used to calculate the band gap of $Cu_2O(111)$. The interaction of valence electrons with ionic cores is described within the projector augmented wave (PAW) method [175]. Complete structural relaxation at the hybrid level for all considered systems are allowed by using soft oxygen pseudopotentials and an energy cutoff of 270 eV. The Brillouin zone of the surface unit cell is sampled with a (4x4x1) Monkhorst-Pack k-point grid [176]. The atomic coordinates of all ions in the oxide film are relaxed until residual forces dropped below 0.01 eV / Å, while in plane coordinates of the gold atoms were kept at fixed positions.

We will start our discussion with ultra thin, 1 ML films. A 1 ML thick film of $Cu_2O(111)$ consists of a network of O-Cu rings because of the structure of Cu_2O as two interwoven sub-lattices. The Cu_{cus} in the centre of the rings are not connected to the Cu-O network but have to adsorb directly to the substrate. Calculations from [163] show that the support plays a crucial role in the stabilization of the 1 ML cuprous oxide film. Lee and co-workers [177] identified two Cu_3-O pyramidal structures attaching the film to the Au(111) substrate: Cu_3-O_{low}/Au_{top} and Cu_3-O_{up}/Au_{fcc}. O_{low} are oxygen atoms shifted downwards with respect to the Cu-plane whereas O_{up} are shifted upwards. This disables the usual outwards relaxation of all oxygen atoms found in oxide monolayers supported on late transition and noble metals [163]. In simulated STM images [177] O_{up} produce a bright contrast, whereas the unoccupied place in the centre of the O-Cu rings (at the three-fold hollow site of Au(111)) show the darkest contrast (Fig. 8.7). Although Cu_{csa} are not visible the oxide film at the dislocation between stripes was found to be copper-terminated by recent stability calculations [163].

Adsorption of additional copper atoms directly in the Cu-O rings of the $Cu_2O(111)$-Cu_{cus} shows an energy gain of ≈3 eV per copper atom. This is less favourable than the energy gain per copper atom in bulk copper (3.7 eV) which makes the formation of copper clusters more likely than the integration of Cu_{cus} into an already formed $Cu_2O(111)$-Cu_{cus} film. This picture may however change if kinetic effects are included into the calculations.

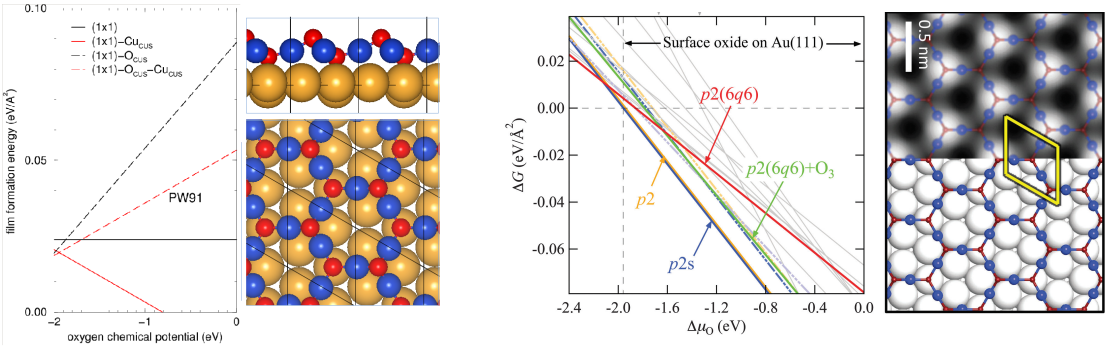


FIGURE 8.7: Stability diagram for 1 ML $Cu_2O(111)$ by Goniakowski (left) and Lee (right). In the right picture p2 denotes the (1×1)-Cu_{cus} surface. In both calculations the copper deficient surface is the most stable for 1 ML in the relevant range of oxygen chemical potentials. left [163], right [177]

From the evaporation rate discussed before, we know that the Cu_2O films in this work are about 4-7 ML thick. To compare, a 3 ML thick Cu_2O film on Au(111) is simulated as well, consisting of three O-4Cu-O trilayers in contact with three-layer Au(111). A (1×1)-$Cu_2O(111)$ // (2x2)Au(111) unit cell with the in-plane lattice parameter of Au(111) was used. The Cu_2O lattice is compressed to fit the gold lattice, which in reality might occur at the interface between Cu_2O and gold for a confined area. However the 4.8% smaller

lattice cannot be kept up indefinitely, resulting in dislocation lines to release stress from the lattice, as observed in STM. Calculations for the uncompressed bulk termination follow in the next paragraph.

All slabs are separated by at least 10 Å vacuum and dipole correction is applied to slabs with two inequivalent terminations. The results show that the gold substrate stabilizes the Cu_{cus} while destabilizing O_{cus} at the oxide/metal interface therefore making the two film terminations inequivalent. At the free film surface the stoichiometric (1×1) and the copper depleted (1×1)-Cu_{cus} surface compete. However the HSE approach shows the stoichiometric surface to be favoured at realistic oxygen lean conditions $\mu_O \leq 1.7\,eV$ in contrast to the GGA results.

Looking at the electronic properties the (1×1) termination remains insulating with E_F within the band gap (Fig. 8.8 c bottom). Theoretical calculations have estimated the band gap to be 0.5-0.8 eV for GGA+U [178] and 0.4 eV using GGA, both values much smaller than the experimental value. However, HSE-based calculations lead to a severely improved band gap of 1.96 eV [179].

Additionally an empty Cu_{cus} s - O_{cus} $p_{x,y}$ surface state is created below the bottom of the conduction band. Its position within the band gap is governed by the reduced electrostatic potential at the coordinatively unsaturated surface ions. This surface state does not appear on the non-stoichiometric (1×1)-Cu_{cus}

In contrast, in the (1×1)-Cu_{cus} the top of the oxide valence band is depleted (Fig. 8.8 c top) because of holes left by the missing Cu_{cus}. This leads to a metallization of the surface and the formation of a two dimensional hole-gas. The depletion might also work as charge compensation required for electrostatic stabilization of (1×1)-Cu_{cus} surface which is a polar type-2 surface according to Taskers classification [180, 181].

To further explore the origin of the contrast produced by the empty Cu_{cus} s - O_{cus} $p_{x,y}$ gap state of the stoichiometric surface termination the Tersoff-Hamann model [66, 67] was employed to simulate STM images. At a positive bias of 2V (similar to the experimental conditions) bright spots are located at the position of Cu_{cus}, grey regions correspond to O_{cus} and neighbouring Cu, whereas a deep black contrast is situated at positions of subsurface oxygen (Fig. 8.8 d).

Thus the geometric effect created by the O_{cus} located nearly 1 Å more outward than Cu_{cus} is overridden by an electronic contribution coming from the diffuse character of the Cu_{cus} s compared to the directional O_{cus} $p_{x,y}$ orbitals. In the case of a 3 ML gold-supported Cu_2O(111) film the calculated results show that the stoichiometric (non Cu-deficient) Cu_2O(111) is obtained at typical conditions of UHV experiments like annealing in vacuum or low O_2 partial pressures.

To better understand which surface feature leads to the difference in the two methods

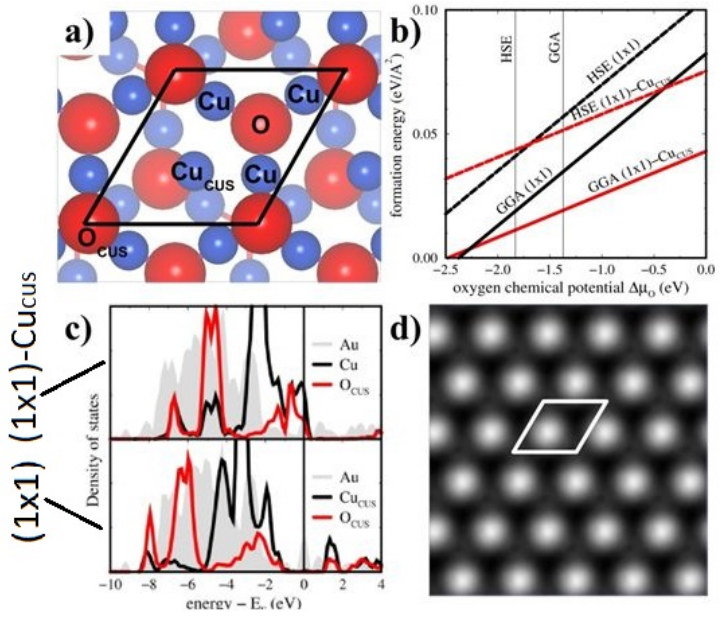


FIGURE 8.8: 3 ML of $Cu_2O(111)$ supported on Au(111) (a) Structural model of the stoichiometric $Cu_2O(111)$ surface. In the Cu-deficient surface Cu_{cus} is missing. (b) Film formation energies as calculated in GGA and HSE with respect to bulk cuprous oxide as a function of the oxygen chemical potential. Vertical lines indicate the limit of formation of bulk Cu_2O. (c) Cu-deficient (top) and stoichiometric (bottom) surface DOS calculated in HSE. (d) Simulated STM image of the stoichiometric termination at 2 V sample bias. [179]

of calculation, thick unsupported $Cu_2O(111)$ films were modelled. They consist of symmetric slabs of 6 O-4Cu-O tri-layers at the calculated in-plane lattice parameter of bulk Cu_2O (6.1 Å GGA und 6.07 Å HSE) thus representing the bulk termination.
Same as for the thin film calculations and in line with previous results [5, 171] GGA predicts the copper deficient (1×1)-Cu_{cus} surface to be stable at the entire range of oxygen chemical potentials used. HSE calculations on the other hand favour the stoichiometric (1×1) $Cu_2O(111)$ termination in an even wider range of O_2 chemical potentials than in the thin film case ($\mu \leq$ -1.4 eV compared to -1.7 eV).
The difference between GGA and HSE goes beyond the effect of an enhanced stability of the O_2 triplet state in HSE [182]. Instead it is to be linked to the Cu-deficient and thereby polar character of the (1×1)-Cu_{cus} termination, which induces surface metallicity (Fig. 8.9 b).
The hybrid calculations show an increased thermodynamic stability of the stoichiometric surface over the copper depleted surface contradicting earlier GGA-based calculations. The contrast seen in STM measurements is therefore predicted to arise from the Cu_{cus} atoms and is mostly of electronic origin.

A compilation of predicted surface terminations for different film thicknesses can be found in tab. 8.1. Calculations for a 1 ML thin $Cu_2O(111)$ film on Au(111) found

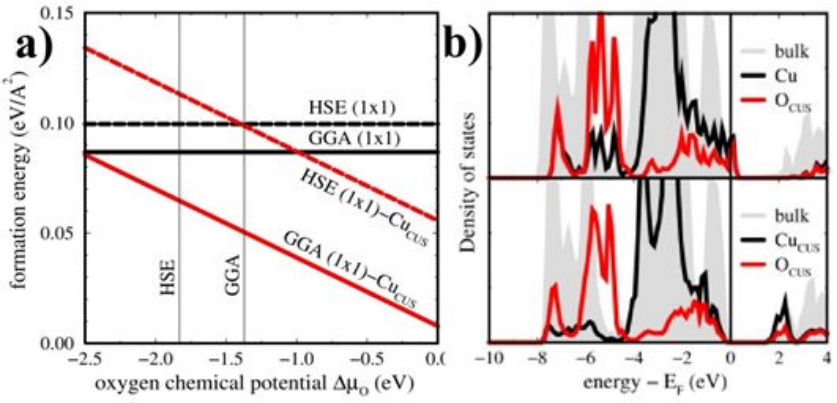


FIGURE 8.9: 6 ML of unsupported (1×1)- Cu_2O(111) (a) Film formation energies as calculated in GGA and HSE with respect to bulk cuprous oxide as a function of the oxygen chemical potential. Vertical lines indicate the limit of formation of bulk Cu_2O. (b) Cu-deficient (top) and stoichiometric (bottom) surface DOS calculated in HSE. [179]

ML	DFT	μ / eV	Surface	Reference
6	GGA	-2 $\leq \mu \leq$ 0	(1×1)-Cu_{cus}	[179]
6	HSE	-2 $\leq \mu \leq$ -1.4	(1×1)	[179]
6	HSE	-1.4 $\leq \mu \leq$ 0	(1×1)-Cu_{cus}	[179]
3	GGA	-2 $\leq \mu \leq$ 0	(1×1)-Cu_{cus}	[179]
3	HSE	-2 $\leq \mu \leq$ -1.7	(1×1)	[179]
3	HSE	-1.7 $\leq \mu \leq$ 0	(1×1)-Cu_{cus}	[179]
1	GGA	$\mu \leq$ -2.2	donuts p2(6q6)	[177]
1	PW91	-2 $\leq \mu \leq$ 0	(1×1)-Cu_{cus}	[163]
1	GGA	-2 $\leq \mu \leq$ 0	(1×1)-Cu_{cus} (p2)	[177]
	GGA(+U)	-2 $\leq \mu \leq$ 0	(1×1)-Cu_{cus}	[4, 5, 171]

TABLE 8.1: Overview of favoured Cu_2O(111) surface terminations from different theoretical works. In the case of one mono-layer the copper deficient surface is the most stable. For films of more than one mono-layer the stoichiometric surface is favoured.

the oxygen atoms to be responsible for the contrast in STM images in agreement with earlier studies [4, 5, 171]. However in this work thin films of 4-7 ML were prepared. When increasing the film thickness to 3 ML and 6 ML the stoichiometric (1×1) surface becomes the most stable over the entire range of relevant oxygen chemical potentials. An empty Cu_{cus} s - O_{cus} $p_{x,y}$ surface state is created below the bottom of the conduction band creating the contrast in STM which is thus a purely electronic effect.

8.3.2 Electronic Properties

The HSE calculations have shown a band gap of 1.96 eV and a Cu_{cus} derived surface state in the unoccupied half of the band gap. Scanning tunneling spectroscopy can be

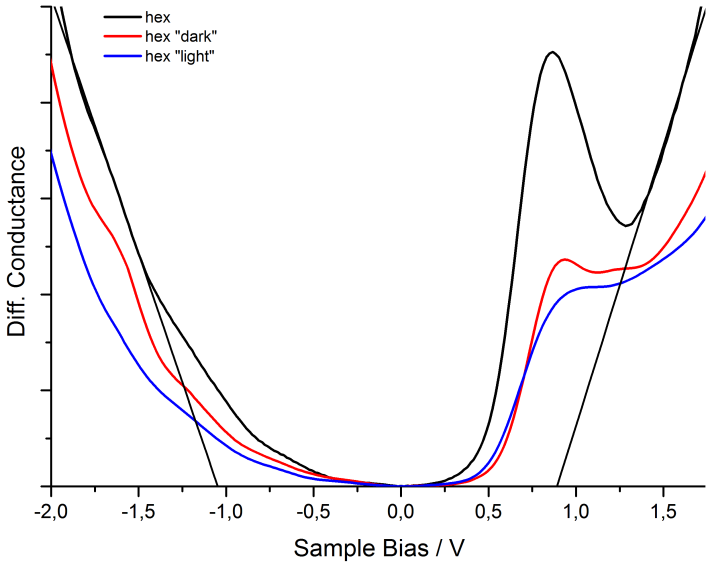


FIGURE 8.10: Differential conductance spectra of the hexagonal phase. The band gap is ≈ 1.9 eV with a pronounced surface state below the CB edge. For different domains of the hexagonal phase, different variations of the surface state were found. See Fig. 8.11 as well.

used to measure the band gap and surface states, thereby making a verification of the oxidation state and the surface termination possible.

The local electronic structure was probed with STM conductance spectroscopy (see section 3.1.5) performed with lock-in technique at 973 Hz and 10 mV modulation bias. The band gap for cuprous oxide could be easily distinguished by the voltage range showing no resulting tunnel current. Surface states (explained in section 3.1.6) for Au(111), Cu(111) and Cu_2O(111) could be observed as a rise in tunnel current in the dI/dV spectra.

The electronic properties of the Cu_2O film can be characterized by the measured band gap of $\approx 1.9\,eV$, derived from STM conductance spectra shown in Fig. 8.10, matching the calculated band gap from HSE (1.96 eV). This is smaller than the bulk value of 2.15 eV reflecting the thin film nature [52], but still larger than than the CuO gap of 1.4 eV. Fitting of the CB edge is challenging because of a pronounced surface state within the band gap close to the CB onset leading to an earlier rise of conductivity (Fig. 8.10). The surface state in the unoccupied upper half of the band gap, matches HSE calculations as shown in section 8.3.1.

Because of the lattice mismatch between Cu_2O(111) and Au(111) (4.8%) the favourable lattice registry cannot be established indefinitely. Dislocation lines occur to release the stress from the lattice. One dislocation line is shown in Fig. 8.12. The different apparent contrasts occurring in derivative image mode points to a different placement of Cu_2O on the gold support in the two domains (the exact structure model will be shown in the

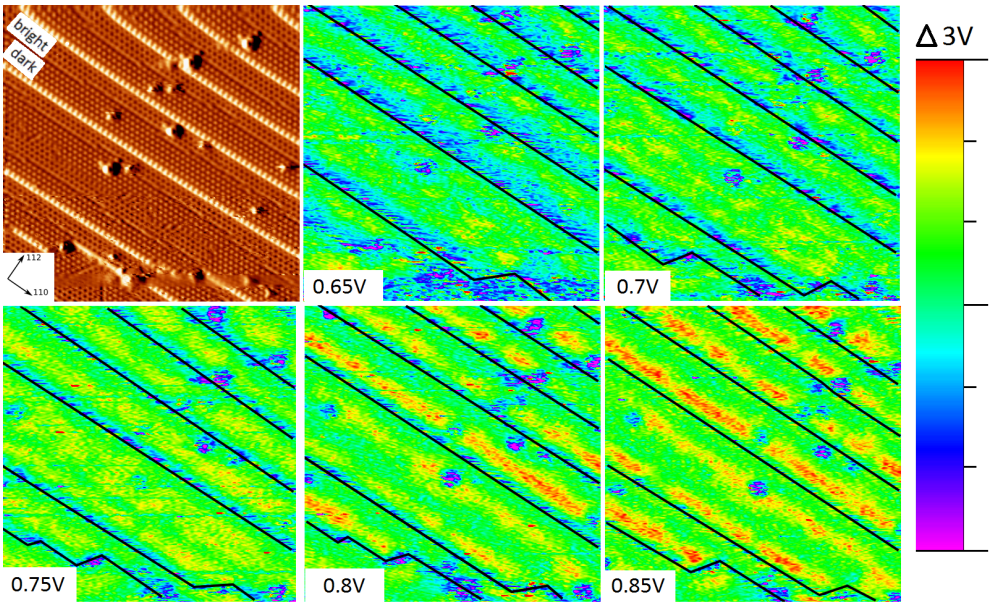


FIGURE 8.11: dI/dV maps of an annealed film $(32\times32)\,\mathrm{nm}^2$
Up to 0.7 V bias voltage the conductance is low, due to the band gap. Starting at 0.8 eV the conductivity rises, due to the surface state (also seen in Fig. 8.10. In the topographic image different domains can be distinguished by the apparent contrast. In the "dark" domain a larger surface state occurs, as seen by the red color in the dI/dV map. This is also visible in the differential conductance spectra Fig. 8.10.

next section). Also a variation in the surface state for on both sides of the dislocation line was found, as already shown in Fig. 8.10.
In Fig. 8.11 several terraces with alternating domains are shown. dI/dV maps are used to show the spatial variation of the surface state. Starting at 0.65 eV (inside the band gap) both domains show little conductivity. At 0.85 eV the surface state leads to an increase in conductivity, with one domain clearly reaching a higher conductivity, leading to the alternating red and green domains in the dI/dV map, corresponding to the "dark" and "bright" domains in the topographic image. These slight shifts in the position of the surface state are related to the different binding sites for interfacial Cu and O atoms with respect to the Au(111) surface.

8.3.3 Structure Models

After confirming the surface to be Cu_2O-(1×1) by HSE calculations checked with conductance spectroscopy, a structural model of the hexagonal phase was developed. According to HSE calculations Cu_{cus}-atoms are responsible for the bright contrast in STM images of thick Cu_2O films as shown in Fig. 8.12.
$Cu_2O(111)$-(1×1) consists of Cu_6O_6-rings with an unsaturated Cu_{cus} in the centre. The hexagonal unit cell (Fig. 8.12) shows an asymmetric arrangement of atoms. In one half

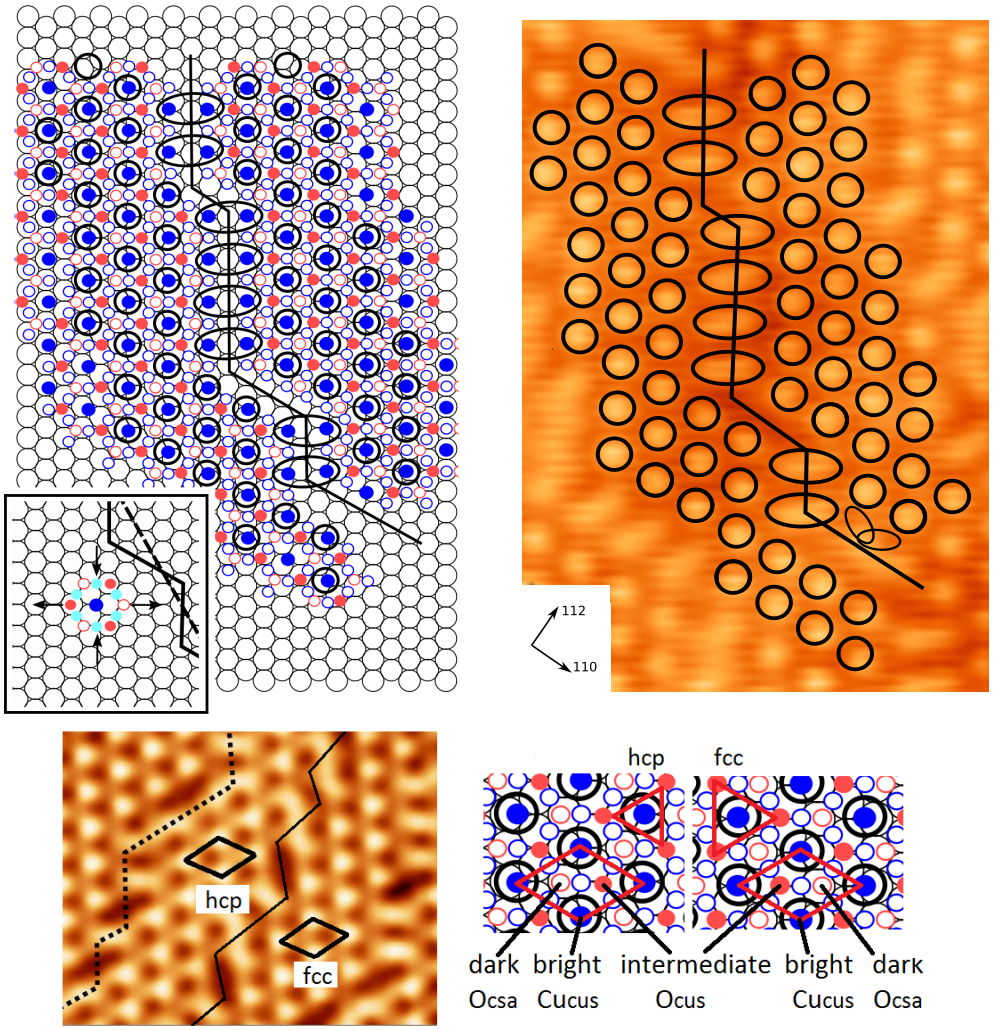
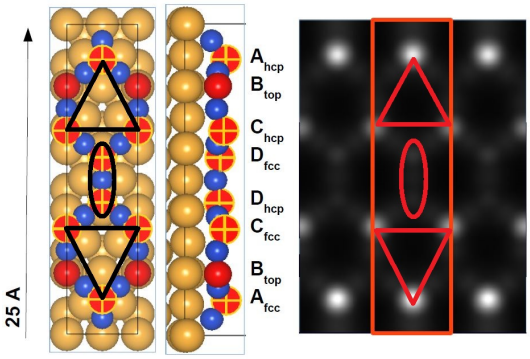


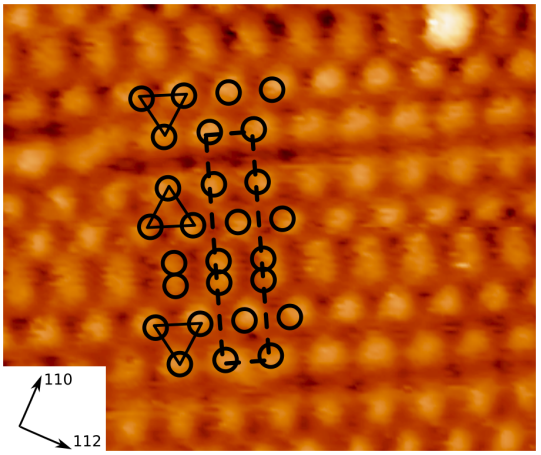
FIGURE 8.12: Unit Cell in derivative mode (bottom), topographic image (right) and structure model (left) of the hexagonal phase. blue solid: Cu_{cus}, blue hollow: Cu_{csa}, red solid: O_{cus}, red hollow: O_{csa}. The contrast stems from the Cu_{cus} and different tunneling conditions into nearby oxygen atoms. The domain border follows a zig-zag path along Au(110) with the mean direction along Au(112). The Cu_2O unit cell is elongated in the direction of Au(112) and squeezed in the direction of Au(110). Visible spots are Cu_{cus} (dark blue) matching the marked spots from the topographic image.

a Cu_{cus} ion is located. In the other half there is one O_{csa} surrounded by three Cu_{csa}. Because both are coordinatively saturated, a dark spot occurs at this position. At the corners of the unit cell O_{cus} are responsible for an intermediate contrast, which is only overridden by the diffuse Cu_{cus} spots.

Looking at larger STM topographic images, frequent domain boundaries separating elongated domains of 4 to 5 unit cells width along the short axis can be observed. The domain boundary runs along the Au[110] direction locally, but the zig-zag pattern results in a mean direction along Au[112]. Because of the lattice mismatch between Cu_2O(111) and Au(111) the favourable registry can only be established in a confined space before



(A) The contrast stems primarily from the O_{up} creating the triangles observed in STM. The central dimer feature is not as bright because the oxygen atoms are on an intermediate height. [163]



(B) Topographic image of the [110]I stripe phase. Each unit cell contains two triangles and a central dimer structure.

FIGURE 8.13: Topographic image, ball model and simulated STM image of the stripe [110]I phase

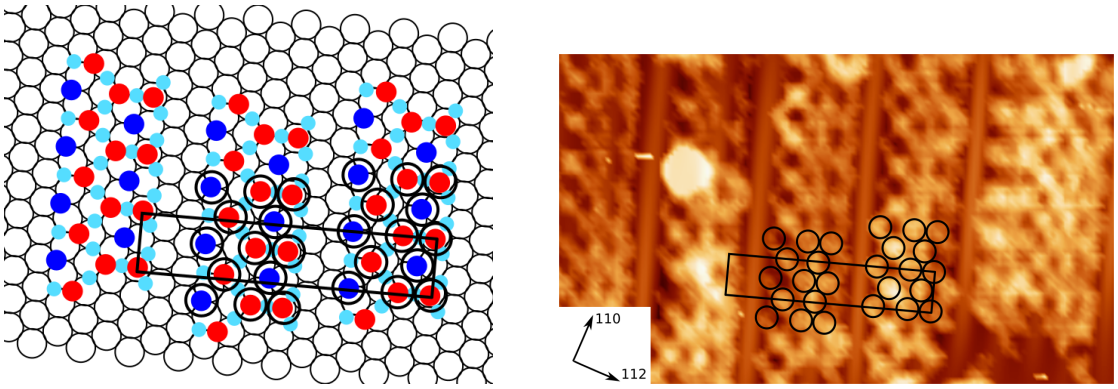
inserting a new domain boundary [183]. The hexagonal Cu-O rings are tetragonally distorted, i.e. elongated in one direction and squeezed in the other, as shown in the inset in Fig. 8.12.

Along the dislocation line the domains are separated by larger atomic distance ("empty" areas) and occasionally elongated protrusions. In the structure model both features are incorporated. At the dislocation line the Cu-O network terminates because too much mismatch between favourable positions and actual positions on the gold lattice has build up. Half a position is skipped before the next Cu_2O domain starts, resulting in a switch of the Cu_{cus} positions from hcp to fcc with respect to the gold substrate. This leads to the observed switch in dark and bright contrast best seen in STM images in derivative mode.

Another possible scenario to switch Cu_{cus} from hcp to fcc is by putting them close together, forming a Cu-dimer where usually only one Cu_{cus} would be situated in a Cu-O ring. This results in the elongated features found along the domain boundary. Another explanation would be a single Cu_{cus} picking up energy from the tip and thereby rapidly switching its position thus resulting in the elongated feature.

8.4 Stripe Phase along Au[110]

In addition to the bulk-like hexagonal phase more complex surface structures were observed. One group of structures comprises stripes oriented along the Au[110] direction. There are different variations probably due to different imaging contrasts of the tip or



(A) Structure model for the [110]II stripe phase. Both Cu_{cus} as well as oxygen atoms are used to generate the visible contrast.

(B) Topographic image of the [110]II stripe phase. A denser atomic arrangement than in the [110]I stripe phase is observed.

FIGURE 8.14: Topographic images and structure model of the stripe [110]II phase encountered in the annealed films.

slightly different growth conditions and post-growths treatment leading to (local) variations of the film thickness. Overall the stripes seem less like the bulk-like termination and are thus probably thinner than the hexagonal phase.

Two atomically resolved versions of the Stripe [110] phase, called [110]I and [110]II, are shown in Fig. 8.13 and Fig. 8.14 respectively. The stripe [110]I phase is build by rectangular unit cells $(6\times30)\,\text{Å}^2$ in size perpendicular to the direction of the stripes. The internal structure is composed of two triangles separated by an elongated feature. The overall hexagonal arrangement makes $Cu_2O(111)$ the preferred starting point. The stripe [110]II phase seems more complicated. Again a rectangular unit cell of about the same size was found. However the [110]II phase features a denser atomic arrangement, with probably more than one atomic species visible. DFT calculations and structural models for the stripe [110]I phase are not yet conclusive. The structure model is shown in Fig. 8.13. It uses a Cu-deficient unit cell $(6\times25)\,\text{Å}^2$ containing 13 copper and 8 oxygen atoms on a Au(111) support. This unit cell neglects the dislocation line between stripes, which could be simulated by extending the unit cell to $(6\times30)\,\text{Å}^2$ without adding further atoms. The unoccupied space of 5 Å reduces the formation energy of the stripes by 0.15 eV, effectively creating a repulsion between stripes [163] as observed in STM. The oxide film at the dislocation between stripes was found to be copper-terminated, i.e. complete hexagonal rings with added Cu atoms on the outside are favourable. Oxygen terminated rings or incomplete rings (CuO-termination) are less stable by -4.1 eV and -3 eV respectively. Respective STM images were simulated for the charge density from 0 to 1 V at 5 Å above the Au(111) surface. In this model, same as in the 1 ML hexagon phase, some oxygen atoms relax outwards (A,C) whereas others relax inward (B). Due to the finite width of the stripe structure the centre oxygen atoms (D) are found to be on intermediate height, with negligible difference between hcp and fcc positions. The

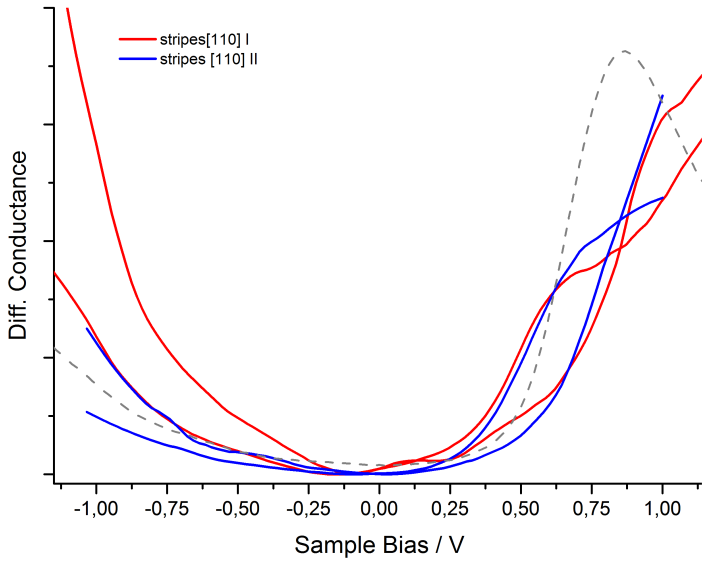


FIGURE 8.15: Differential conductance spectra of both instances of the stripe 110 phase. For comparison the differential conductance of the hexagonal phase (×2) is also shown. There is a certain variability in the spectra on both types, however, no surface state directly below 1 V could be found in the [110] phase.

calculated STM contrast is dominated solely by the vertical position of oxygen atoms. However the central elongated feature between the two triangles is not clearly resolved.

The denser atomic arrangement in the stripe[110]II phase makes a model with both Cu_{cus} and oxygen atoms necessary. The recorded contrast can be explained by a ball model shown in Fig. 8.14 where all oxygen atoms as well as unsaturated copper atoms are visible. Each stripe is composed of the already known Cu-O rings which are not closed in this case. The rings on the right side of the stripe are missing one oxygen atom, whereas the rings on the left half of the stripe miss three oxygen atoms. Still all broken rings contain one Cu_{cus}. So far there are no calculations on the theoretic stability of such a configuration.

With conductance spectroscopy no surface state between 0.8 V and 1 V was found for either version of the stripe [110] phase. DFT calculations (see section 8.3.1) have shown that Cu_{cus} is not stable in the 1 ML film. Therefore the contrast in one mono-layer is created by oxygen atoms whereas it stems from Cu_{cus} in thicker films. Different amounts of Cu_{cus} as well as different film thickness and thereby different contrast produced by oxygen atoms could account for a number of variations on the stripe phase.

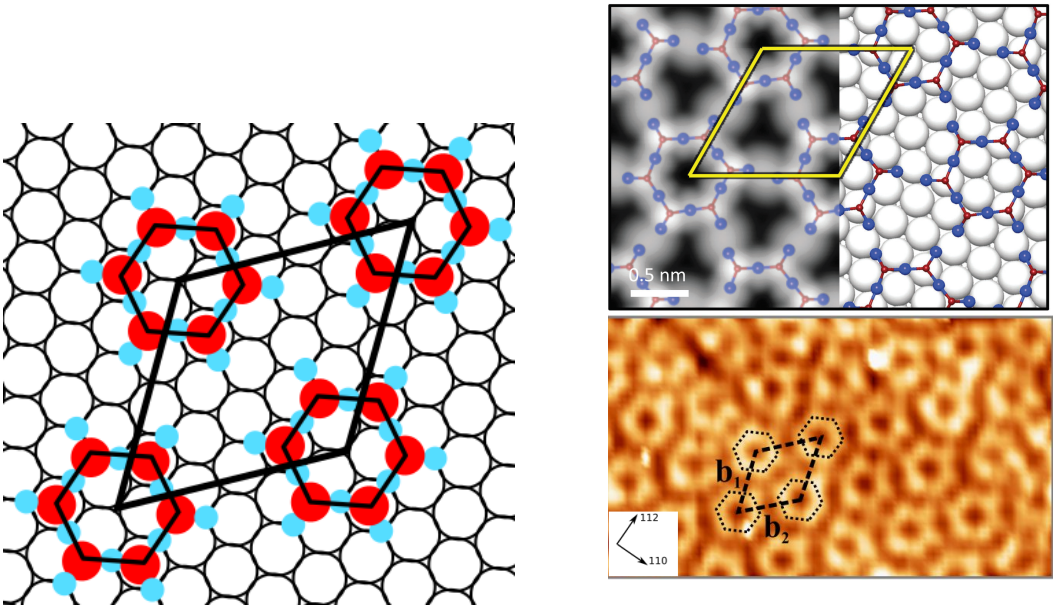


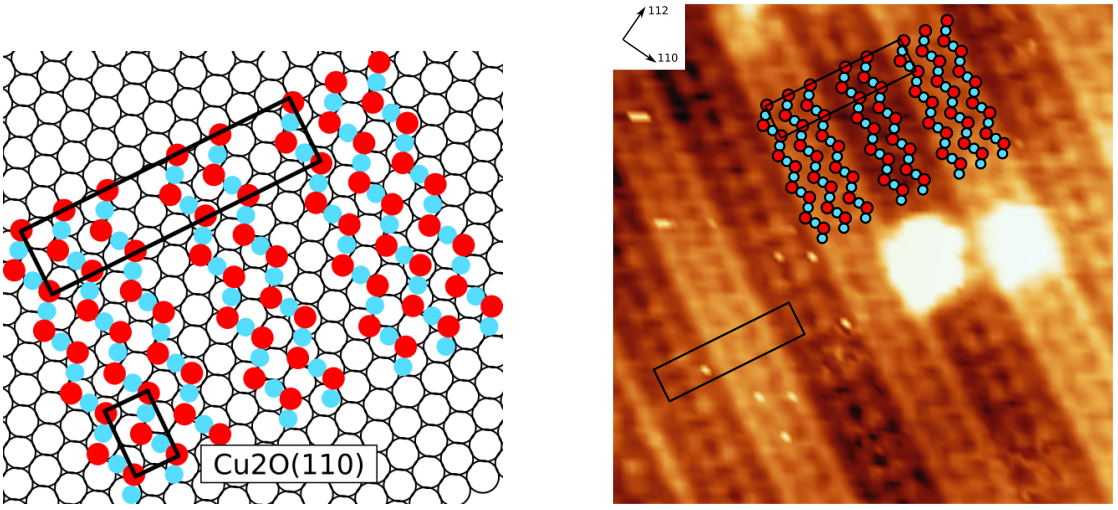
FIGURE 8.16: Right: Topographic image and structure model by Lee et. al of the donut phase. Left: Improved model with better match of the distance between the rings. The visible contrast comes from the oxygen atoms making up the six-membered rings which are interconnected by a hexagonal arrangement with 12.5 Å spacing. Bottom right [168], top right [177]

8.5 Stripe Phase along Au[112] and Donut phase

The as-grown films are the farthest from thermodynamic equilibrium, so the previously discussed structure models do not fit here. Observed structures in as-grown films are a stripe phase along Au[112] and a donut phase, characterized by its distinct six-membered rings. Again, structural models are derived from topological and electronic structures and supported by DFT calculations wherever possible.

The donut phase shows larger dimensions as already seen from LEED images in section 8.2.1 and is therefore less likely to be influenced by strain in the Cu_2O film. A very common way to achieve such strain reduction is by rotating main structural elements as for example shown for vanadium oxide in literature [184]. The unit vectors of the donut phase are indeed rotated by 12° towards the Au[110] directions. The observed values amount to b_1=b_2=12.5 Å and an angle of 60 °between them. Although the donut phase was found to be thermodynamically unlikely it could form due to kinetic hindrance or by statistical preference [177].

The six-membered rings of the donut phase make building blocks derived from Cu_2O(111) the most likely solution. Each "donut" is a six-membered O-Cu_{csa} ring as found in Cu_2O(111) with the centre Cu_{cus} missing. The measured 12.5 Å distance between the centres of adjacent donuts can be achieved by tilting 12° away from Au[110] where



(A) Structure model for the [112] stripe phase.

(B) (8×4.5)nm^2 -500mV

FIGURE 8.17: Topographic images and structure models of the stripe [112] phase encountered in as-grown films.

two hollow sites that are 13.05 Å apart can be found. The outer Cu atoms of the Cu-terminated Cu-O rings are embedded at three-fold hollow site of the Au(111) substrate stabilizing the structure. Due to the unique arrangement into separate rings, all oxygen atoms in the donut structure are located at similar height above the Au surface and higher than the copper atoms, unlike in the 1 ML Cu_2O(111). The resulting ball model shown in Fig. 8.16 is in excellent agreement with the STM topographic images.
Simulated STM images (Fig. 8.16) by Lee et al.[177] show all six oxygen to be visible with the outer copper atoms contributing to the contrast as well. Note that in the model proposed by Lee et al. the distance between the individual rings is too close, so the contrast from the outer Cu atoms might be enhanced too much.

In the stripe [112] phase the strain in the oxide lattice orthogonal to the stripes results in two different halves of the stripes. In the topographic image shown in Fig. 8.17b the stripes seem to be composed of alternating bright and dark sections. Within the dark stripe half a square building block of (4.3×4.3) Å^2 containing four atoms is visible.
For the stripe [112] phase a structure model starting from the Cu_2O(110) surface is proposed. The Cu_2O(110) surface features a rectangular unit cell and "zig-zag" rows of alternating Cu and O atoms. The herringbone reconstruction of the Au(111) surface could serve as a growth template here, matching the periodicity the O-Cu rows of Cu_2O(110). Shifting every second row by half a position, the square and rectangular details of the stripe [112] phase are achieved. The width of the dark stripe matches two Cu-O rows from Cu_2O(110) whereas the bright stripe matches three Cu-O rows from Cu_2O(110). Copper atoms in Cu_2O(110) are still coordinatively saturated with two oxygen neighbours in the same plane, fitting the experimental results from conductance

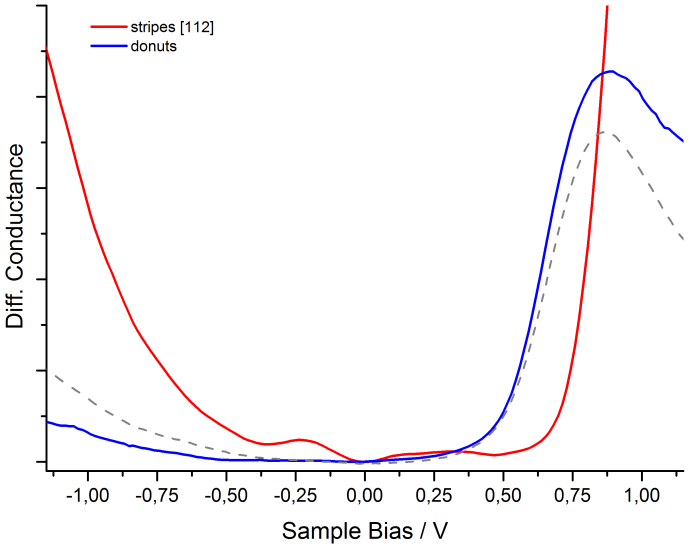


FIGURE 8.18: Differential conductance spectra of the stripe [112] and donut phase with the hexagonal phase (scaled $\times 4$) for comparison. The donut phase shows the same surface state below the CB (around 0.8 V) as the hexagonal phase whereas the stripe [112] phase only shows the CB onset at 1 V.

spectroscopy which suggest that no unsaturated copper atoms are present. Oxygen atoms on the other hand are only three-fold coordinated (to two copper atoms in the same plane and one in the layer below) instead of four-fold as in bulk Cu_2O, which makes oxygen the better candidate to explain the contrast.

Looking at the electronic properties (Fig. 8.18), the donut structure shows a surface state at 0.8 V very similar to the one observed in the hexagonal phase, but the 112 stripe phase shows no surface state but the conduction band onset at 1 eV is clearly visible. The absence of a surface state in the stripe [112] phase matches the structure model, as all Cu-ions in the Cu_2O[110] surface are coordinatively saturated. However the pronounced surface state in the donut phase seems to contradict the structure model, especially as Cu_{cus} was shown to be instable in a 1 ML Cu_2O film. At this stage, the dI/dV maximum is assigned to a remnant of the Au(111) surface state that shines through the holes in the donut phase, yet at an energy strongly shifted due to the copper-oxide film. A similar behaviour has been observed for Au(111) modified by ultrathin MgO films before [185].

Again, the spatial distribution of electronic states can be seen from dI/dV-maps. At very low bias voltage (close to the Fermi level) the dI/dV signal is generally low. A first conductance rise is observed at +0.55 V on the donut phase which translates to the onset of the aforementioned surface state in this region. At +0.75 V the contrast reverses and the stripe phase begins to dominate the images. Interestingly modulations inside the stripe phase could be measured showing the individual 1D building blocks even more pronounced than in the corresponding topographic images. The last contrast

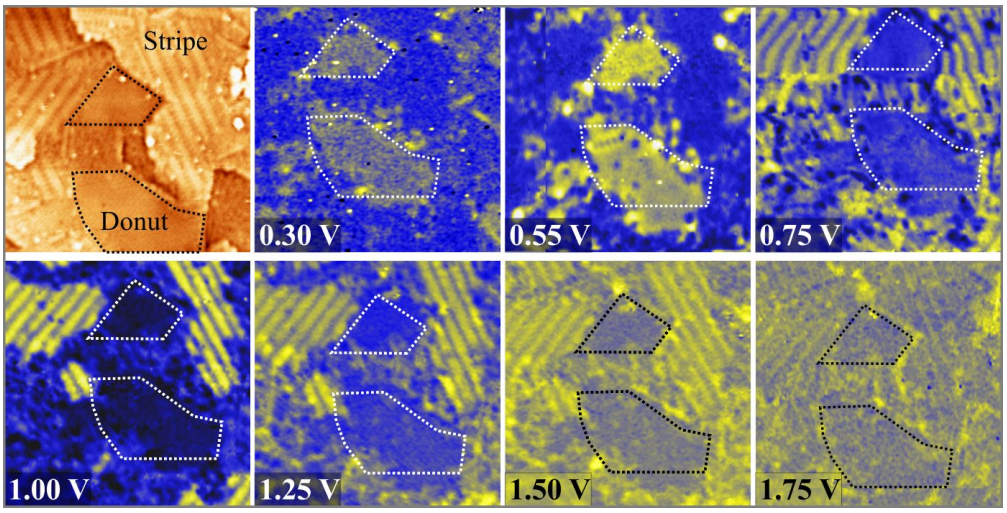


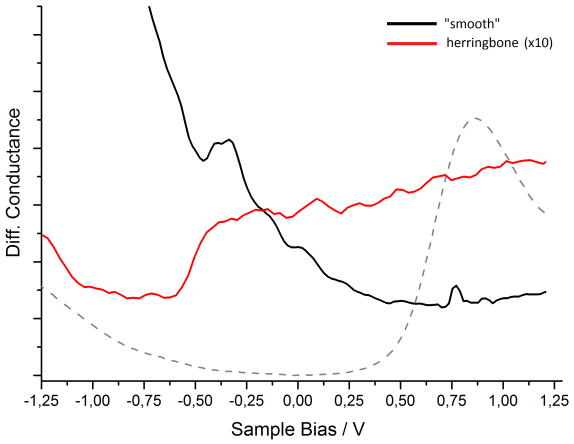
FIGURE 8.19: dI/dV maps of an as-grown film showing different electronic properties of donut and stripe(112) phase. The onset of a surface state in the donut phase at 0.55 V and in the stripe [112] phase at 0.75 V can be seen. At 1.5 V the conductance is more uniform as the conduction band is reached. [168]

regime starting at 1.5 V shows no more local variation instead the entire surface now has a high conductivity indicative for tunneling into the oxide conduction band.

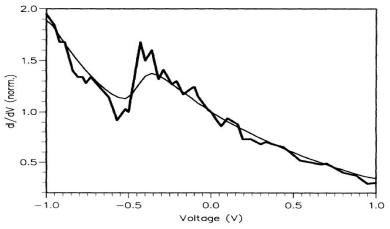
8.6 Smooth Areas and Herringbone Areas

I will finally discuss the appearance of so-called "smooth" areas and domains showing the herringbone reconstruction, being observed after annealing at high temperatures. Theoretical stability calculations for 1 ML $Cu_2O(111)$ on Au(111) [177] found the pristine gold surface to be the most stable until $\mu \leq$ -1.96 eV whereas [163] found (1x1)-O_{cus} to be favoured until $\mu \leq$ -2 eV . Both could indicate the reduction (loss of oxygen) and decomposition of the 1 ML oxide film at high temperatures. The so-called "smooth" areas (see Fig. 8.21) seem to be common after post-annealing. Herringbone areas show up in post-annealed samples as well. For some regions "holes" in the oxide film seem to develop. These might be due to decomposition of the oxide film by desorption of oxygen or alloying of copper atoms with the gold support or by dewetting of the film under certain conditions.

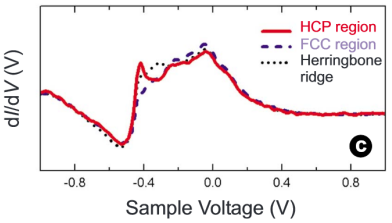
Conductance spectra (Fig. 8.20 left) on the herringbone areas show the expected step-like surface state onset of Au(111) at about -0.5 V whereas the spectrum taken on a "smooth" areas shows a surface state onset at -0.4 V compatible with the Shockley surface state of Cu(111). Furthermore the overall shape of both spectra matches the shape found in literature for noble metal and not for oxide surfaces (Fig. 8.20 right side).



(A) Spectra taken on a Herringbone area (red) and a "smooth" area (black)



(B) Surface State onset on Cu(111)[186]



(C) Surface State onset on Au(111)[166]

FIGURE 8.20: (A) Measured STS showing the surface state onset for the herringbone and smooth areas as well as the band gap of Cu_2O for comparison (not to scale). (B) and (C) references for gold and copper surface states from literature.

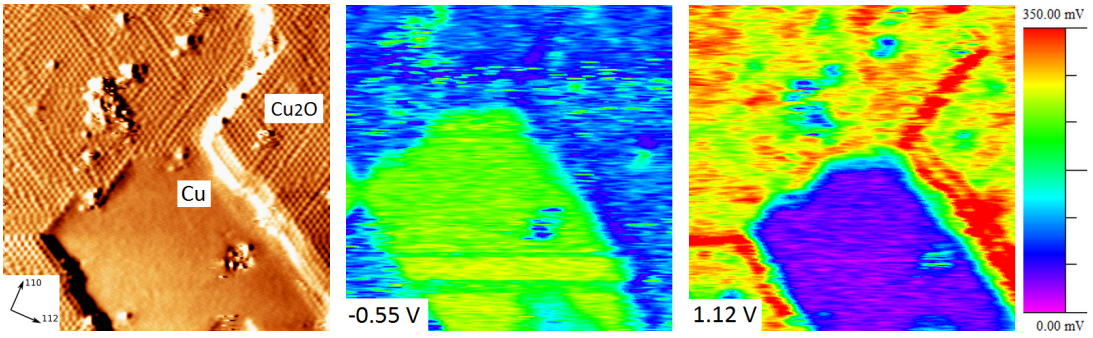


FIGURE 8.21: dI/dV maps $(30\times30)\,nm^2$ of a smooth area surrounded by $Cu_2O(111)$ easily distinguished by the hexagonal atomic pattern. $(30\times30)\,nm^2$ Red color corresponds to a high conductivity. At negative bias the smooth area has higher conductance than the Cu_2O although the difference is more pronounced at positive bias where the surrounding Cu_2O has the higher conductivity.

dI/dV images taken on a "smooth" area and surrounding Cu_2O hexagonal phase are shown in Fig. 8.21. They clearly show an inversion of the dI/dV contrast when going from negative to positive tunneling bias matching the spectra for Cu_2O and Cu as shown in Fig. 8.20. At -0.55 V sample bias Cu_2O is a poor conductor because of the band gap whereas it turns into a better conductor at 1.12 V because of the conduction band. Metallic copper on the other hand features an overall better conductivity at negative bias as seen from Fig. 8.20. Thus the "smooth" areas that arise from heavy heating of the Cu2O (111) film seem to be metallic copper. Apparently, copper oxides gets completely reduced at this conditions, leaving a bare Cu layer on the Au(111) surface.

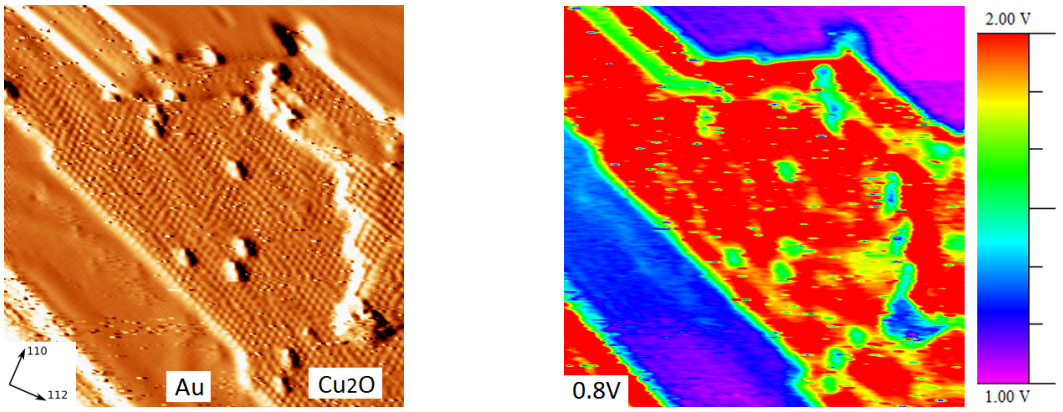


FIGURE 8.22: Topography and dI/dV image of a copper oxide film on a gold substrate $(30\times30)\,\mathrm{nm}^2$. Red color corresponds to a high conductivity. At 0.8 V the Cu_2O identified by the hexagonal atomic pattern has higher conductivity than the gold substrate identified by the herringbone reconstruction.

8.7 Phase Diagram

In this chapter, the appearance of the previously discussed surface structures depending on the preparation conditions is discussed. For this purpose 19 preparations (shown in Tab. 8.3) were evaluated. 13 samples were annealed after reactive copper deposition using electron bombardment to access thermal equilibrium state. 6 samples were not subjected to any further treatment after preparation, hence are "as-prepared". Post-annealing was done under UHV conditions or in oxygen partial pressures and generally took 5 to 10 minutes. The preparation conditions and the resulting surface structures are shown in Tab. 8.3. Based on this table, a pressure-temperature phase diagram on the stability of various Cu-O phases is proposed, as shown in Fig. 8.23.
The distribution of observed surface structures in as-prepared and post-annealed samples can be viewed from Tab. 8.2. Based on this table, it is evident that the donut and [112] phase are as-grown structures whereas the hexagonal, triangular, smooth and herringbone surface structures are more common in the annealed samples. The [110]

Structure	As-prepared (E)		Post-annealed (A)	
sum	6		13	
hexagonal	0	0%	8	61.5%
triangles	1	16.7%	4	30.8%
stripes [110]	2	33.3%	2	15.4%
donuts	2	33.3%	0	0%
smooth	0	0%	5	38.5%
herringbone	0	0%	2	21.4%
stripes [112]	3	50%	2	15.4%

TABLE 8.2: Number of as-prepared and post-annealed samples showing the respective surface structures.

Number	Date	Preparation	T / K	p_{O_2} / mbar	μ_{O_2} / eV	d / nm	d / ML	stripes	triangles	donuts	hexagonal	smooth	herringbone
A1	30.06.2014	E	378	1.00E-06	-0.68	1.8	6	112		x			
A2	04.07.2014	A	775	1.00E-08	-1.69	≤ 1.8	≤ 6				x		
D1	18.08.2014	E	417	1.00E-06	-0.71	1.8	6			x			
D3	18.08.2014	A	775	1.00E-08	-1.69	≤ 3.2	≤ 12				x	x	x
E1	22.09.2014	E	381	4.40E-06	-0.63	1.8	6	110					
E2	01.10.2014	A	825	1.00E-08	-1.80	≤ 1.8	≤ 6	110	x				
E4	08.10.2014	A	785	1.00E-08	-1.71	≤ 3.2	≤ 12				x	x	
G3	02.12.2014	A	665	1.00E-06	-1.19	≤ 0.68	≤ 2.25		x		x	x	
H1	08.12.2014	E	378	1.00E-05	-0.60	1.35	4,5	112					
H2	10.12.2014	A	688	5.00E-07	-1.27	≤ 1.35	$\leq 4,5$	112	x				
J3	16.02.2015	A	660	1.00E-07	-1.31	≤ 1.8	≤ 6		x				
J4	20.02.2015	A	700	1.00E-08	-1.53	≤ 1.8	≤ 6	110					
K4	20.04.2015	A	788	1.90E-06	-1.36	≤ 1.8	≤ 6				x	x	
K6	27.04.2015	A	836	6.00E-06	-1.37	≤ 1.8	≤ 6				x		x
L2	07.05.2015	A	727	1.00E-08	-1.59	≤ 1.8	≤ 6	112					
L4	08.05.2015	A	788	1.50E-06	-1.38	≤ 1.8	≤ 6				x	x	
Q1	01.12.2015	E	465	2.50E-05	-0.67	0.9	3	110	x				
Q2	07.12.2015	A	727	1.00E-05	-1.15	≤ 0.9	≤ 3				x		
R1	14.12.2015	E	486	1.00E-05	-0.74	1.8	6	112					

TABLE 8.3: Phase diagram of observed surface structures. *d*: nominal film thickness as calculated from the evaporation rate and time Annealing was done under UHV conditions or in oxygen partial pressures. The temperature was monitored via the pyrometer or calculated from the heating power.

stripes seem to be an intermediate feature common in annealed and as grown samples alike.

In the examined range of 5×10^{-7} mbar to 1×10^{-5} mbar O_2 pressure has less influence than the sample temperature. However, as preliminary experiments conducted at 0.1 to 5 mbar (in the HPC) have shown during XPS analysis a more complete oxidation takes place at higher O_2 pressures. In addition literature suggests CuO formation at higher temperature and oxidation pressure [24, 159]. Temperature on the other hand plays an important role in the formation of surface structures. In the following, the position of the surface structures in the P-T-diagram are discussed.

First, the donut phase is probably a minority phase. It appeared around 400 K and 1×10^{-6} mbar O_2 pressure. As it only appeared twice and in as-grown films it could occur due to kinetic hindrance or statistical preference. The [112] stripes often occurred in the as-grown films (350-450 K and 1×10^{-6} mbar to 5.5×10^{-5} mbar O_2). At these conditions the herringbone reconstruction is likely not lifted, thus the [112] stripes are probably very thin films with stabilization (or initial orientation) by the herringbone reconstruction. In some cases the [112] stripes survived annealing up to 727 K and thus appear at higher

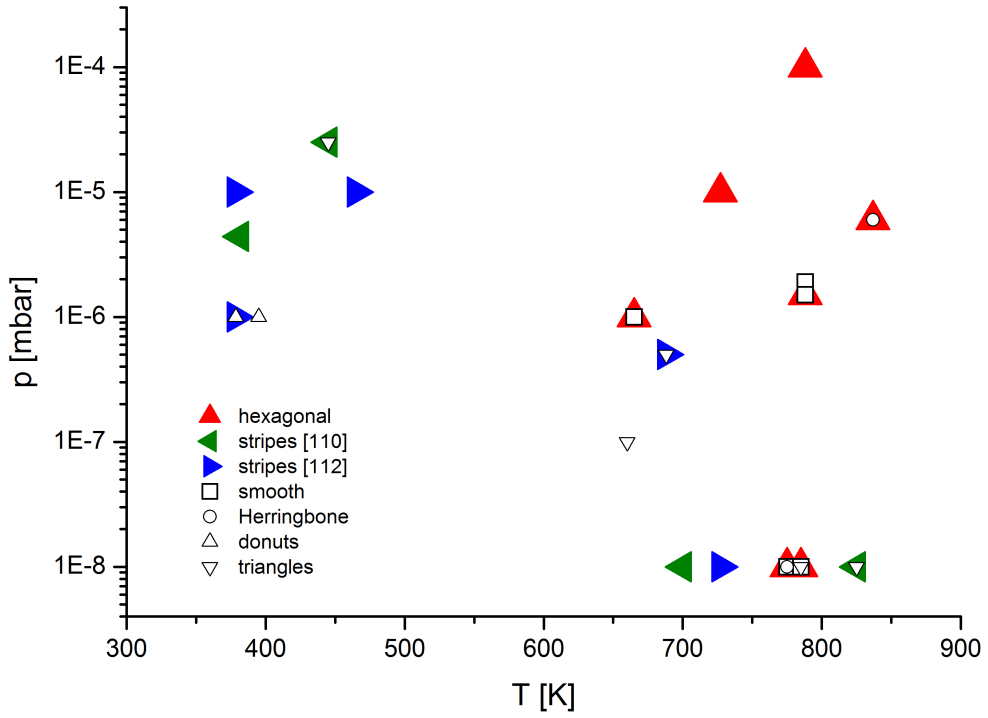


FIGURE 8.23: Phase diagramm of observed surface structures for Cu_2O on Au(111)

T in the P-T-diagram. Annealing at higher temperatures (775 K or more) led to the disappearance of the [112] stripes. More common after annealing are the [110] stripes. After annealing at higher temperatures the herringbone reconstruction is lifted and the [110] stripes are probably a result of re-ordering into the Cu_2O(111) film as the (111) surface is more stable than the Cu_2O(110) and the lattice mismatch is smaller. The [110] stripes survived annealing up to 825 K. The remaining lattice mismatch with the gold support in this temperature range results in tetragonal distortion and the appearance of the observed stripes. Also after annealing at elevated temperatures the triangular domain appears. The internal hexagonal arrangement of the triangular domains points to a close relationship with the hexagonal phase. The triangles are probably an intermediate step when changing from the stripe phase to the hexagonal phase during annealing. The bulk-like hexagonal phase was encountered in the temperature range from 650 K to 800 K and over the entire p_{O2} range from 1×10^{-8} to 1×10^{-4}. This phase seems the most stable, as the lattice mismatch between Au(111) and Cu_2O(111) is the smallest. Additionally the hexagonal phase was only reached after annealing, whereas the striped phases occurred in as-prepared samples as well. In about the same temperature regime, but at lower p_{O2} (only up to 1×10^{-6} the so-called "smooth" areas are found alongside the hexagonal phase. As these are assigned to metallic Cu according to STS results,

they indicate the loss of oxygen from the surface and subsequent reduction of Cu_2O so that their appearance at lower p_{O2} seems reasonable. At elevated temperatures (750 K to 850 K) the herringbone reconstruction of Au(111) reappears in small domains. As Cu is unlikely to desorb from the surface, Cu-Au alloying and diffusion into the gold substrate seems the likely pathway at these conditions.

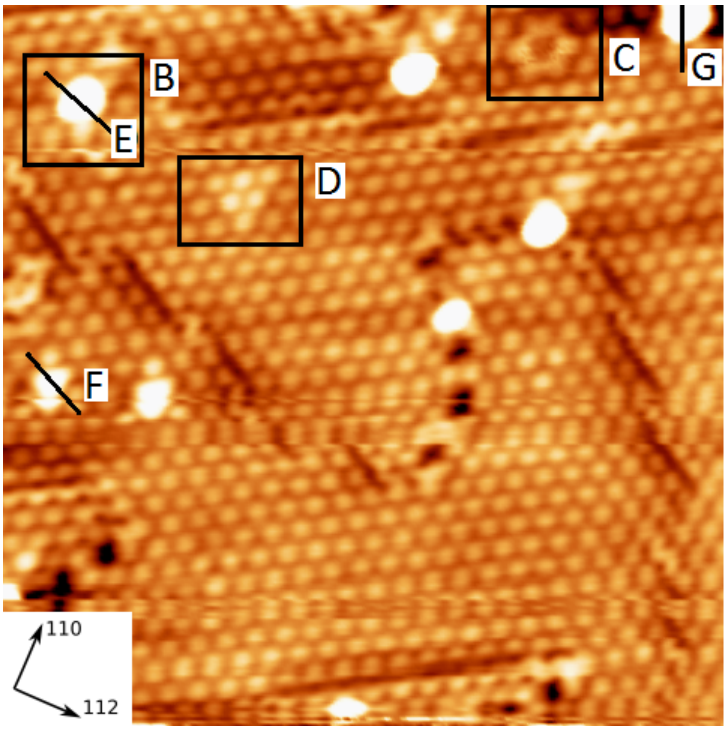
8.8 Ad-Particles

Finally, the often observed appearance of ad-particles is discussed in this section. The prepared and annealed Cu_2O films are never entirely flat but always show a number of molecular-sized ad-particles on almost all surface structures (triangles, hexagonal, stripes [110] and [112]). Exceptions are "smooth" Cu areas and herringbone Au areas where no ad-particles were found (see Figs. 8.6b, 8.21 and 8.6a, 8.22 respectively). Also the donut phase seems to show no or only little ad-particles as in Fig. 8.3. The positions of these ad-particles always correspond to fixed positions on the hexagonal or stripe phase. As nothing else has been dosed, the ad-particles likely consist of Cu_2O species. The fixed lattice positions suggest that they occur at distinct sites of the Cu_2O lattice and probably constitute the first building blocks of the next layer.
Four preparation will be discussed more closely as examples for the appearance of ad-particles. Those are:

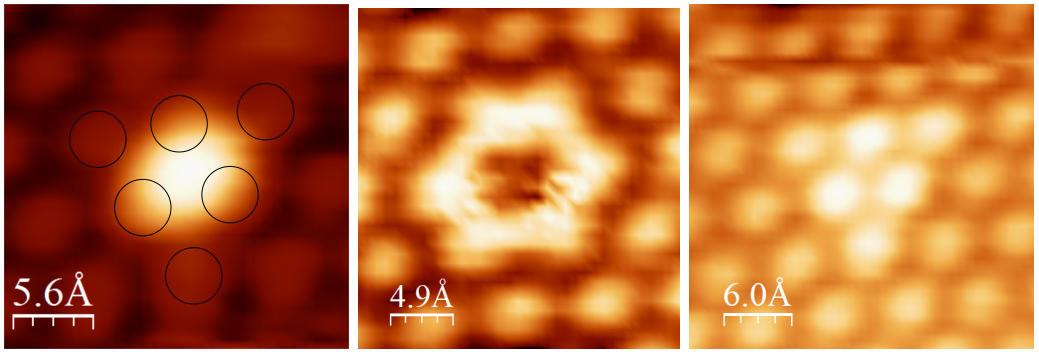
No.	Date		T / K	p_{O2} / mbar	μ / eV	structure
K4	20.04.2015	A	788	1.90E-06	-1.36	hexagonal phase
H2	10.12.2014	A	688	5.00E-07	-1.27	110 stripes
L2	07.05.2015	A	727	1.00E-08	-1.59	112 stripes
R1	14.12.2015	E	486	1.00E-05	-0.74	112 stripes

TABLE 8.4: Four preparations showing the ad-particles on different surface structures. The preparations are either "as-grown" (E) or "post-annealed" (A) at the given temperature and oxygen pressure.

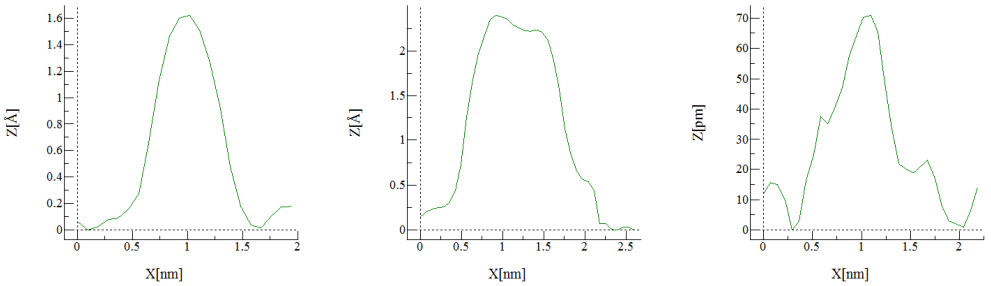
Figure 8.24 shows the hexagonal phase with several ad-particles. As the image was acquired at -700 mV bias voltage, hence probing the occupied states, the ad-particles cannot be assigned to simple Cu vacancies that should appear as depressions and not as protrusions, as found here. In fact, a geometric interpretation of the protrusions is more plausible and they should be assigned to true ad-particles localized at the surface. Some details are shown in Fig. 8.24 (B-D). The structure shown in (C) consists of a Cu_{cus}-6-ring with the central Cu_{cus} missing. The surrounding Cu_{cus} relax towards the vacancy thus creating the brighter contrast. Another structure (D) shows a triangle of 6 Cu_{cus} that are closer together and brighter than the surrounding Cu_{cus}. This feature



(A) (16×16) nm at -700 mV



(B) (C) (D)

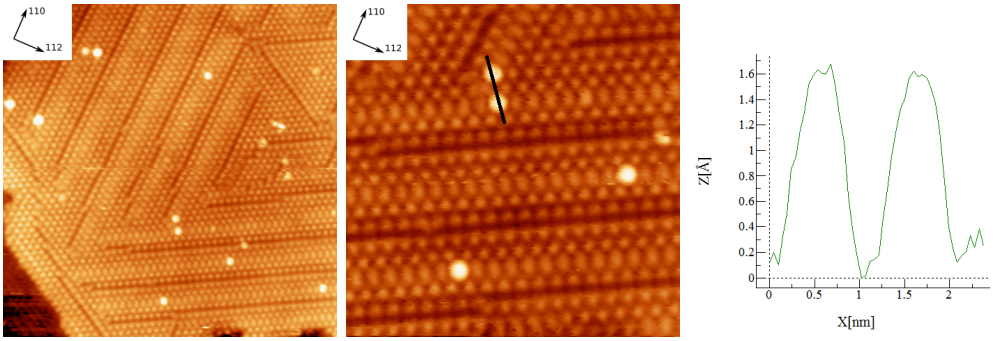


(E) (F) (G)

FIGURE 8.24: Native defects and ad-particles on the hexagonal phase. (B) Ad-particle on top of a O_{cus} site (in the three-fold hollow Cu_{cus} place). This is a first building block of the next $Cu_2O(111)$ layer. (C) Defect structure that may possibly be assigned to a Cu_{cus} vacancy with surrounding Cu_{cus} relaxing towards the vacancy. (D) 6 Cu_{cus} in an unusually close configuration, creating a brighter contrast. (E-G) hight profile of three different particle sizes

could be due to geometric or electronic structures. The first would indicate a local "bump" in the gold support whereas the latter would probably show a local variation in the electronic structure. Note, that this structures are rarely observed at the surface and are no common defect features in Cu_2O.

More common are the type of ad-particles as shown in Fig. 8.24 (B). It sits in between a three-fold hollow site of the Cu_{cus} lattice, corresponding to the position of an O_{cus}-ion. Apparently, an isolated Cu atom binds directly on top of the O_{cus} sites, forming the kind of protrusions observed in STM. This Cu adatom can be assumed to form the nucleation centre of the next Cu_2O layer that would grow at further Cu+O exposure. This type of ad-particle exists in different sizes, as shown in (E-G). Most particles are 1 nm wide and appear in two hights (0.7 nm and 1.6 nm) (E,F). The particle in (F) is 1.5 nm wide and 2 nm high. A plausible explanation of these ad-particles are larger building blocks of the new Cu_2O layers, such as Cu-O, Cu-O_3 or Cu_3-O_3 elements. Note that bigger 2D islands have never been observed, most likely because they always nucleate at step edges of the existing film.



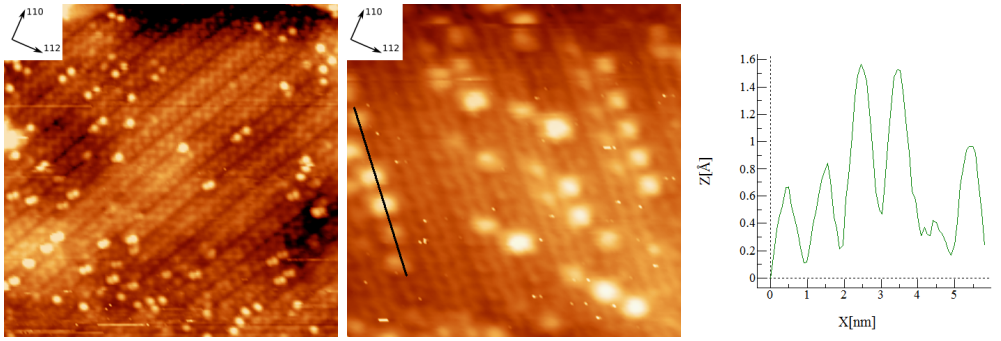
(A) (30×30) nm^2 at 1 V (B) (12×12) nm^2 at 1 V (C) line profile from (B)

FIGURE 8.25: Ad-particles on the [110] stripe phase appear on fixed positions on the site of the elongated feature. They could mark an isolated Cu adatom or a Cu-trimer or more likely a O-Cu_3 building block attached to the Cu_{cus}.

Ad-particles were also found on the [110] and [112] stripe phases.
On the [110] stripes ad-particles are rather uniform, as can be seen from Fig. 8.25. They always appear on the elongated feature in the centre of the stripe. As seen from (C) the most common particles are again 1 nm wide and 1.6 nm high. This dimension would match the size of an extra Cu adatom sitting on top of the Cu dimer located already in the film beneath. The resulting Cu-trimers would indeed be energetically favourable, as shown from DFT calculations [163]. A layer-by-layer Cu_2O growth is hard to explain with the growth of Cu-clusters. However, this situation changes immediately if the ad-particles consist of both Cu and oxygen and constitute for instance O-Cu_3 building block attached to the Cu_{cus}.

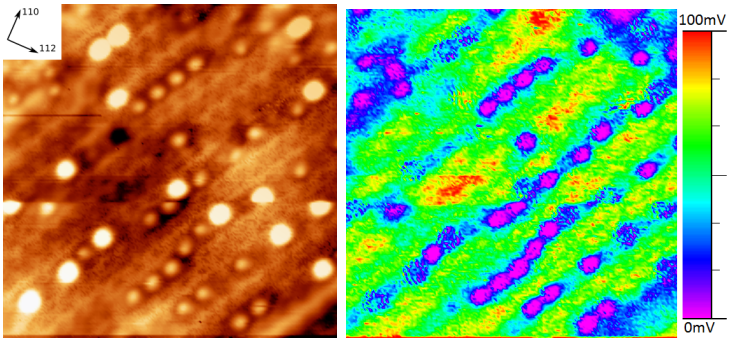
On the [112] stripes the ad-particles are located on the triangular features and in between the stripes. Unfortunately, as the structure model of the [112] stripes is less reliable, a detailed discussion of the binding site of ad-particles is not yet possible. Still, the size of the ad-particles can be seen from Figs. 8.26 (B,C) and 8.27 (C,D). Again the ad-particles are about 1 nm wide and either 0.7 nm or 1.6 nm high. Also the spacing between the ad-particles is very regular with 1 nm distance. This points to a distinct binding site on the Cu_2O lattice.
In Fig. 8.27 (B) a dI/dV image of the [112] phase showing both sizes of ad-particles is shown. Surprisingly, both sizes show very different conductivity at positive bias voltage. The bigger particles show the same conductivity as the surrounding Cu_2O, whereas the smaller particles show a lower conductivity. Thus at the small particles more electrons are expected, leading to a local decrease in the empty density of states. An adsorbed oxygen atom could account for this. In building the next layer, up to three Cu would bind to the oxygen, thereby making the ad-particle more Cu_2O-like.

In conclusion, the ad-particles observed on all Cu_2O films are interpreted as Cu-O elements that most likely mark the nucleation centres of the following Cu_2O plane.



(A) $(27\times27)\,nm^2$ at negative bias (B) $(11\times11)\,nm^2$ at 1.7V (C) line profile from (B)

FIGURE 8.26: Ad-particles on the [112] stripe phase, commonly on the triangular features or in between the stripes.



(A) $(15\times15)\,nm^2$ at 1.8V (B) dI/dV image of (A)

FIGURE 8.27: Ad-particles on the 122 stripe phase and corresponding dI/dV image showing the difference in conductivity for the different particle sizes.

Chapter 9

Cu_2O-films on Mo(001) - Role of the support

9.1 Introduction

To study the influence of the support on the oxidation behaviour of copper a support that differs in terms of chemical inertness and possible interface interactions has been used as a second substrate. In the previous section an Au(111) single crystal was used that is known to be chemically inert. Here, a molybdenum single crystal Mo(001) is used as chemically reactive substrate.
Molybdenum crystallizes in a body-centred cubic lattice with a unit cell length of 3.147 Å and three atoms per unit cell. Thus on the 001-surface a square atomic pattern with 3.147 Å spacing between atoms of the topmost layer and 2.73 Å spacing between atoms of the topmost and second layer occurs. From the electronic perspective Mo(001) features dominant 3d states at the Fermi level.
Mo(001) still serves as a template for Cu_2O growth although it has a square symmetry instead of the hexagonal symmetry found in Cu_2O(111) and Au(111). However the atomic distance of 3.147 Å still matches the Cu-Cu distance in Cu_2O of 3.02 Å with a lattice mismatch of 4%. Furthermore molybdenum is highly reactive in contrast to the chemically inert gold . The reactivity might also help to dissociate the O_2 molecules during reactive copper deposition. Finally molybdenum is widely used as a substrate in solar cell applications [52].

After the usual cleaning procedure copper is evaporated in an oxygen atmosphere as specified in chapter 6. From XPS Measurements detailed in chapter 7 a high binding energy shoulder of the Mo 3d peaks after copper deposition in oxygen atmosphere was observed. This indicates formation of MoO_x possibly MoO_3 because of its naturally low

surface energy and thus ease of formation. Furthermore the position and shape of Cu 2p and Cu LMM spectra fit Cu^0 thus showing a hindered oxidation of copper. Measured O 1s peaks are more likely to belong to MoO_x. After reactive copper deposition LEED is used to check for long-range order of the copper films, however no discernable pattern is revealed in LEED suggesting the absence of any long-range order. Apparently, the Cu does not oxidise on the Mo(001) surface but metallic Cu structures are formed instead.

9.2 Structure and Morphology

Insight into the morphology of the copper thin films is obtained with the Scanning Tunneling Microscope. Despite the identical preparation procedure strong differences are found comparing to Cu_2O on Au(111), in line with the XPS results.

Contrary to the film morphology on Au(111) shown in the previous chapter 8 no continuous film seems to grow on Mo(001). Instead well-shaped particles are found which, following the results from XPS are mainly comprised of metallic Cu. With a nominal film thickness of ≈3 ML the particle size can be estimated to be laterally (8±4) nm and vertically (2.5±1) nm. This gives an aspect ratio of 0.3 which should be handled as a lower bound because no tip convolution effects were considered. The granular structure increases the surface roughness to 8 nm, one order of magnitude larger than on Au(111).

Several distinct particle shapes can be found repeatedly in all measurements. The most abundant has the shape of a truncated octahedron with a square top facet as seen in Fig. 9.2. The main side facets are of hexagonal shape and inclined by ≈ 50° against

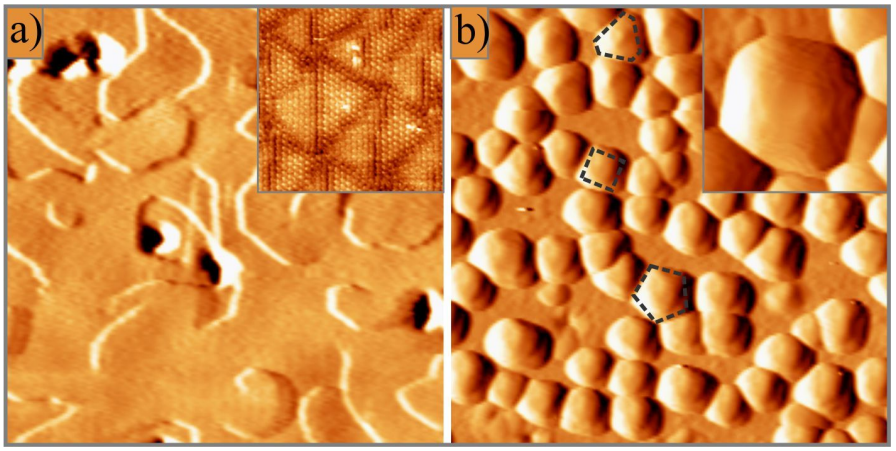


FIGURE 9.1: Typical STM images ((100×100) nm^2, derivative mode) showing the topography of samples obtained via reactive Cu deposition in oxygen atmosphere on (a) Au(111) and (b) Mo(001). (a) A homogeneous film develops on gold. The inset ((15×15) nm^2) shows the Cu_2O-surface with atomic resolution. (b) Cu nano-particles are found on Mo(001). Typical shapes are marked by dashed polygons. [160]

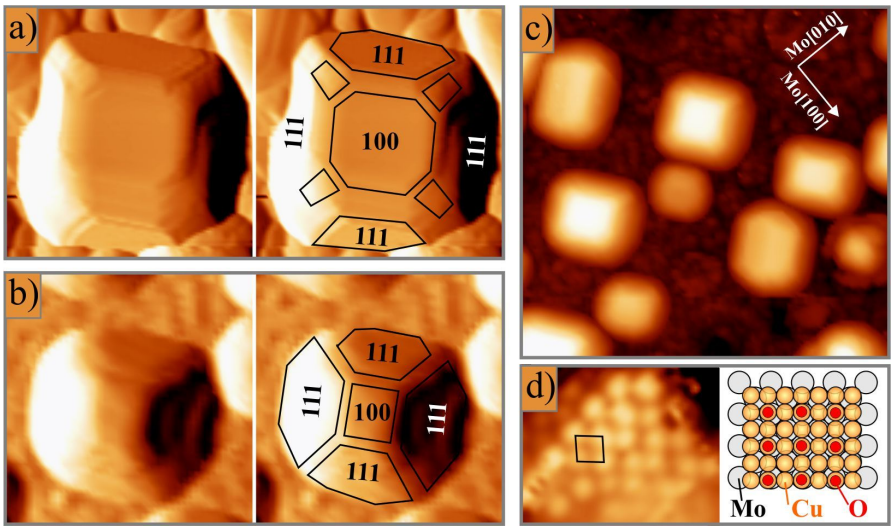


FIGURE 9.2: Different particle shapes on Mo(001) after reactive copper deposition as seen in STM images (derivative mode). (a+b) large and small (100) terminated octahedron ($(10\times10)\,nm^2$) (c) Several (100)-type particles with identical orientation ($(30\times30)\,nm^2$) (d) Atomically resolved top facet ($(3.5\times3.5)\,nm^2$) with a O(2×2) superstructure as illustrated in the ball model. [160]

the sample surface. The top facet is tentatively assigned to be Cu(100) the big side facet to Cu(111) and the smaller side facets to Cu(110). Thus the particle matches the equilibrium shapes of Cu particles found in literature [187, 188]. Most 100-terminated particles share a comparable orientation. This points to a fixed registry with the underlying molybdenum support. Hereby the [110] particle edges align with Mo[110] direction resulting in a (1×1) registry with 11% lattice mismatch as seen in Fig. 9.2d. The rather large compression of the Cu lattice makes this configuration unlikely to occur over larger areas. However it could account for the initial orientation of the particles.

Atomically resolved images of the Cu nano particles show a square arrangement with approximately 5 Å periodicity for the top facet. This would fit a (2×2) superstructure of O-atoms on metallic Cu(100). According to DFT calculations [189] oxygen atoms tend to occupy the fourfold hollow sites in Cu(100) which at a 0.25 ML oxygen coverage shows a (2×2) superstructure in agreement with the experiment. The oxygen termination of Cu particles seems to be all that remained from the massive amounts of oxygen during evaporation. This again confirms the results found with XPS.
Other particle shapes (see Fig. 9.3a) are rotated by 45°. The edges now aline with the Mo[100] direction and all planes are of rectangular shape matching Cu(110). The inclination of 30° between (110)-top facet and (111)-side facet is in agreement with the Wulff picture for (110)-terminated deposits.
A more exotic shape looks like a roof with hexagonal facets on both sides of the ridge which can tentatively be assigned to the Cu(111) plane (see Fig. 9.3b) . Occasionally

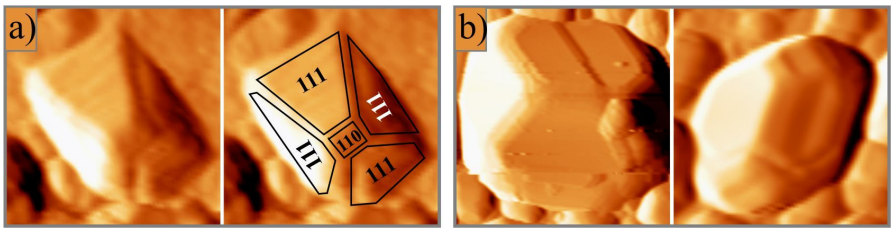


FIGURE 9.3: Other Cu particle shapes found on Mo(001) (a) (110)-terminated Cu particle ($(10\times10)\,\mathrm{nm}^2$) (b) toppled configuration ($(15\times15)\,\mathrm{nm}^2$) [160]

particles with five-fold (dodecahedron) and three-fold ((111)-terminated octahedron) top facets are observed.

9.3 Comparison of Cu+O deposition onto Au and Mo support

The observed difference in growth behaviour (a homogeneous film on Au(111) and small nano particles on Mo(001)) is rather surprising at a first glance.
Molybdenum, being the more reactive support, is able to interact with oxygen [190, 191] and has previously been shown to promote the oxidation of ad-metals [192]. Gold on the other hand shows the inertness of noble metals and should thus be unable to catalyze the copper oxidation because of the lack of oxygen dissociation.
To explain the role of the support the two major qualities of the support in oxidation reactions should be analysed in more detail. These are (i) the efficiency in supplying oxygen for the reaction and (ii) the occurrence of interfacial interactions which can stabilize the emerging oxide film.

(i) Because of the rather different oxidation enthalpies of Mo(001) (-720 kJ/mol) (cite) and Au(111) (-50 kJ/mol) [193] molybdenum interacts with O_2 even at room temperature [190, 194] whereas gold is unable to bind or dissociate O_2 at 300 K due to the large activation barrier [195]. Thus only Mo(001) should be able to provide active oxygen species for the incoming Cu atoms.
In reality the large thermodynamic stability of the Mo-O compound could prevent the oxidation of copper. The incoming O_2 molecules are immediately trapped by the Mo-surface and hence unable to interact with the Cu-atoms. At a prolonged stay in the O_2-atmosphere a passivating MoO_x surface forms which is likely even more inert than the gold surface. This explains the suppressed formation of any Cu_2O on the Mo-support. For the Cu+O/Au(111) system on the other hand a finite albeit small reactivity leads to the growth of Cu_2O.

(ii) The stability of a surface oxide is governed by attractive interactions at the metal-oxide interface. If the surface free energy of the metal is reduced by covering with an oxide layer one would expect wetting growth [196] whereas a larger oxide or interface energy will result in island growth.

$$\gamma_{\text{oxide}} + \gamma_{\text{interface}} < \gamma_{\text{metal}} \quad \text{wetting growth} \tag{9.1}$$

$$\gamma_{\text{oxide}} + \gamma_{\text{interface}} > \gamma_{\text{metal}} \quad \text{island growth} \tag{9.2}$$

All surface free energies relevant for the system of Cu+O on Au(111) and Mo(001) can be found in Tab. 9.1. With the surface free energy of Au(111) about 1eV larger than that of Cu_2O(111) as well as a reasonably small interface energy due to the good lattice match wetting growth is expected for Cu_2O(111) on Au(111) in agreement with the experiment. Recent DFT calculations [163] show that the Au(111)/Cu_2O(111) interface is formed by Cu atoms either in Au fcc or hcp hollow sites, above which bulk-like Cu_2O-trilayers pile up with little distortion.

The surface energy of the Mo(001)-support is considerably higher than that of gold and therefore even more likely to initiate a wetting growth. However, also the interface energy is higher with the only reasonably good lattice match being between Cu_2O(100) and Mo(001). This results in the given square symmetry with a mismatch of about 14%. The surface energy of Cu_2O(100) is slightly higher than that of Cu_2O(111) because of the open and polar nature [3, 140] but still lower than that of Mo(001). Calculated values of the surface energy of Cu_2O(100) depend on the applied surface configurations, oxygen chemical potential and the applied mechanism for polarity compensation.

However with the formation of an Mo-oxide layer during reactive Cu deposition the surface free energy of Mo(001) (2.5 [197] – 3.837 [198] J/m^2) is likely lowered. The resulting surface free energy depends on the composition of the molybdenum oxides. The molybdenum oxide with the lowest surface free energy is MoO_3(010) with (0.2-0.3)J/m^2 [199, 200]. This is because MoO_3 is made up of adjacent bilayers along [010] that are only linked by weak van der Waals forces thus making the (010) plane a natural cleaving plane. XPS suggests the presence of a molybdenum oxide film, probably MoO_2 + MoO_3. Because of the very small surface energy of MoO_3 it should make up for a major part of the oxide layer. The considerably lowered surface free energy of the oxidized support thus is largely responsible for the particle growth.

Post annealing drives the Cu-Mo-O system further towards thermodynamic equilibrium which in this case promotes particle growth and possibly decomposes Cu_2O given the

Lattice Mismatch [%]

$Cu_2O(111)$	Au(111)	3.8
$Cu_2O(100)$	Mo(100)	14

Oxidation Enthalpy [kJ/mol] [193]

Au	-50
Cu	-150
Mo	-720

Surface Free Energy [J/m^2]

$MoO_3(010)$	0.2 - 0.3	[199, 200]
$Cu_2O(111)$	< 0.6	[3, 5, 140]
Au(111)	1.3 - 1.6	[197, 198]
$Cu_2O(100)$	1 - 2	[3, 5, 140]
Mo(001)	2.5 - 3.8	[197]

TABLE 9.1: Lattice mismatch, oxidation enthalpies and surface free energies of copper, molybdenum and gold define the growths mechanisms for Cu+O on Au(111) and Mo(001).

elevated temperatures. As-grown Cu+O films on the Mo-support where not studied with the STM because of the large surface roughness. However XPS clearly reveals a dominance of Cu^0 over Cu^+ prior to annealing so reduction of copper oxide does not take place during post-annealing alone.

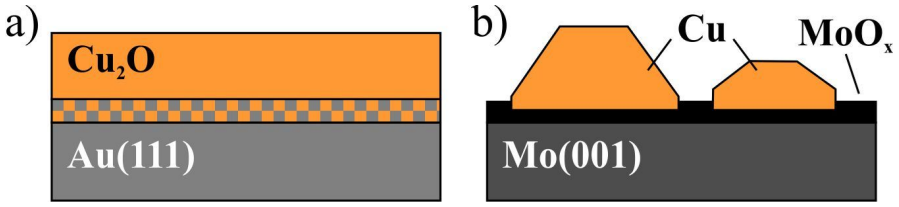


FIGURE 9.4: Different growth models for Cu+O on (a) Au(111) and (b) Mo(001). [160]

Finally, the Cu particle shapes on Mo(001) can be connected to the Wulff theorem to estimate the interfacial work of adhesion. The Wulff theorem states that for a particle in equilibrium shape the real space distance d from the particles' centre to the respective facet is proportional to the facets' surface free energy [124].

$$d_i/\gamma_i = \text{const} \tag{9.3}$$

The work of adhesion can be written as a function of surface und interface energies.

$$W_{\text{adh}} = \gamma_{\text{sub}} + \gamma_{\text{Cu}} - \gamma_{\text{interface}} \tag{9.4}$$

By connecting the former two relations for a cubic lattice with (100) interface plane one gets [201, 202]

$$W_{\text{adh}} = 2\gamma \left[1 - \left(\frac{h \cdot \gamma_{100}}{l \cdot \gamma_{111} \cdot \sin\Theta}\right)\right] \tag{9.5}$$

with Θ being the angle between (111) and (100) planes (Θ=54.7°). The most relevant particle shape (Fig. 9.2) in this work has an aspect ratio of $h/l = 0.3$. With the surface energies of different copper planes from [197, 198] a work of adhesion of $2.5\,J/m^2$ can be calculated.

Comparing to values from literature one finds a good agreement with transition metals bound to semiconducting oxides e.g. Cu/ZnO $3.1\,J/m^2$ [203] and thin film oxids e.g. Pd/alumina $2.8\,J/m^2$ [188, 202] but a big difference to metals on wide-gap bulk oxides e.g. Ag/MgO $0.8\,J/m^2$ [204, 205] and Pd/MgO $0.9\,J/m^2$ [206].

The work of adhesion for the Cu/MoO_x system found in this work is therefore compatible with the typical adhesion strength of metals on oxides with small band gaps and chemically unsaturated surfaces. On the other hand it is to small to account for direct Cu interaction with a metallic Mo(001) surface. This again fosters the idea of a formation of an interfacial MoO_x layer upon reactive Cu deposition.

Part III

Summary and Outlook

Chapter 10

Summary

$Cu_2O(111)$ thin films ($\approx 5\,nm$) were successfully prepared on an Au(111) and a Mo(001) single crystal. Structural and electronic analysis of the oxide films was done using an STM setup. Chemical analysis was conducted using XPS.

On the Au(111) crystal a variety of surface structures was observed. After annealing to 650 K or higher the bulk-like hexagonal phase was the most common. Because of the lattice mismatch between the support and the $Cu_2O(111)$ the film experiences strain, resulting in dislocation lines. Also various stripe structures were found indicating strain relaxation of the film. Two major stripe phases were found, one aligned along the Au[112] direction and the other along Au[110]. Both stripe phases show a number of different internal atomic configurations, being accounted for by different structure models. Also conduction spectroscopy and DFT calculations were used to better understand the nature of both stripe phases. A minority phase characterized by six-membered rings (called donut phase) was found in as-grown films.

Additionally, many protrusions at fixed lattice positions were found on top of the oxide layer, representing the first building blocks of the next $Cu_2O(111)$ layer. So in principle it should be feasible to grow oxide films of arbitrary thickness, exhibiting specific morphological and electronic properties. The band gap for thin films differs from the bulk value as shown by scanning tunneling spectroscopy. The measurements yielded a band gap of about 1.8 eV; slightly smaller than the bulk band gap of 2.1 eV.
Within the unoccupied half of the band gap a previously unknown surface state has be identified. With the help of improved DFT calculations these are attributed to Cu_{cus}, which are only present in the stoichiometric surface. The level of theoretical description could be improved by using hybrid calculations, which reproduce the band gap quite well. Contrary to previous studies the stoichiometric $Cu_2O(111)$ surface is predicted in the entire range of relevant oxygen chemical potentials.

Using XPS a non-negligible amount of metallic copper was detected. The new hybrid calculations show a loss of oxygen at the interface layer, showing that a metallic layer at the gold-oxide interface is not excluded. For photovoltaic devices a control of the interface chemical and electronic properties is decisive. Better theoretical stability calculations can help drive the experiments into the right direction.

In the case of the Mo(001) support no closed Cu_2O film but rather small nano-particles with distinct shapes were found. XPS analysis shows oxidation of the molybdenum substrate while no sign of copper oxidation could be found. Comparison of surface free energies utilizing the Gibbs-Curie-Wulff Theorem on particle growth shows that indeed metallic nano-particles grow on a layer of molybdenum oxide. While this is not useful in photovoltaic applications, the particles might be able to bind and dissociate molecules making the system interesting for heterogeneous catalysis. Growth of well-ordered, uniform nano-particles might also be useful in other applications for instance as optically active centres.

With higher oxygen pressures, such as in the new high pressure cell, the growth of CuO or mixed oxide becomes accessible [128] . Tuning the oxidation level is an additional way of tuning the band gap in an even wider range. The bulk band gap for CuO is 1.4 eV hence much smaller than for Cu_2O. This gives a lot of possibilities for tailoring the properties of the film. Being able to select the film thickness as well as the electric qualities is a main condition to improve Cu_2O based photovoltaics.

This work provides atomic scale insight into the nature of Cu_2O surfaces, which have not been presented in other works so far. By deepening the understanding of the structural, electronical and chemical properties of cuprous oxide thin films, as well as the role of growth conditions and choice of substrate this work helps to develop copper oxides based devices and technologies e.g. for photovoltaics.

Chapter 11

Outlook

As with most scientific works, this thesis not only answers questions it also poses new ones.

A closer look on the layer-by-layer growth of $Cu_2O(111)$ and the internal structure would be of interest. The observed ad-particles could hereby serve as the first building blocks of the new layer. The Cu_{cus} ions together with the O_{cus} of the stoichiometric $Cu_2O(111)$ surface are presumably the reactive sites as they are the points where the interwoven sub-lattices continue. A closer look at these sites and their electronic properties could be of interest to grow various film structures and stoichiometries systematically. Also, the observed Cu vacancies are a good starting point to explore the defect structures and the p-type conductivity in the future.
Moreover, XPS data suggests that there is still a noticeable amount of metallic copper on the sample probably at the interface. Refractive methods as for example XRD could help to understand the interface better and find ways of minimizing metallic copper and increase the thickness of the oxide layer.

Also the preparation of thicker oxide films would be beneficial to close the gap between the bulk and thin film limits. In parts this has already been done by a Master Thesis currently in development [128]. The new high pressure cell has been used to access higher oxygen pressures and thus to prepare thicker oxide films. Unfortunately these turned out to be too rough for reasonable analysis in the STM. However chemical analysis using the XPS characterized the films as Cu_2O and CuO depending on the exact preparation conditions. Using an optical spectrometer the optical characteristics and band gap depending on the oxidation level have been determined [128].

The missing link are thick copper oxide films being flat enough for a STM analysis to look at the structural and electronic properties. This might be feasible using a plasma source

so that atomic instead of molecular oxygen can be used for reactive copper deposition in the preparation chamber. This should facilitate Cu oxidation and help in creating thick, but sufficiently ordered oxide films.
Finally looking at the local optical properties, can help to understand the local oxidation level and the atomic process of oxidation or reduction in a copper oxide film. This type of investigation could be done with a STM-SNOM hybrid using sharp metal-coated optical fibres as tips, which is currently in development in the AG Raspe.
Additionally, the well-ordered and uniform Cu nano-particles found on the molybdenum support can probably be used in nano-catalysis or optics. For this, research on how to tune the density, size and shape (hence surface termination) of the particles as well as the chemical reactivity and optical properties is required. The latter can probably be done using the STM-SNOM hybrid as well.

Overall Cu_2O is interesting as a p-type conductor for photovoltaics, electronic devices, optoelectronics as well as high-temperature superconductivity which makes it a fascinating subject to study.

Bibliography

[1] B. P. Rai. *Cu_2O solar cells: A review.* Sol. Cells **25**, 265-272, (1988).

[2] T. Minami, Y. Nishi and T. Miyata. *High-efficiency Cu_2O-based heterojunction solar cells fabricated using a Ga_2O_3 thin film as n-type layer.* Appl. Phys. Express **6**, 044101, (2013).

[3] A. Soon, M. Todorova, B. Delley and C. Stampfl. *Thermodynamic stability and structure of copper oxide surfaces: A first-principles investigation.* Phys. Rev. B **75**, 125420, (2007).

[4] A. Soon, M. Todorova, B. Delley and C. Stampfl. *Surface oxides of the oxygen-copper system: Precursors to the bulk oxide phase?.* Surf. Sci. **601**, 5809–5813, (2007).

[5] A. Soon, M. Todorova, B. Delley and C. Stampfl. *Thermodynamic stability and structure of copper oxide surfaces: A first-principles investigation.* Phys. Rev. B **75**, 129902(E), (2007).

[6] F. Dimroth, W. Guter, J. Schöne, E. Welser, M. Steiner, E. Oliva, A. Wekkeli, G. Siefer, S. Philipps and A. Bett, *Metamorphic GaInP/GaInAs/Ge triple-junction solar cells with <41 % efficiency* in *34th IEEE photovoltaic specialists conference* (2009).

[7] T. Takamoto, T. Agui, A. Yoshida, K. Nakaido, H. Juso, K. Sasaki, K. Nakamura, H. Yamaguchi, T. Kodama, H. Washio, M. Imazumi and M. Takahashi, *World's highest efficiency triple-junction solar cells fabricated by inverted layers transfer process* in *35 IEEE photovoltaic specialist conference* (2010).

[8] M. A. Green, K. Emery, Y. Hishikawa and W. Warta. *Solar cell efficiency tables (version 35).* Progress in Photovoltaics: Research and Applications **18**, 144-150, (2010).

[9] K. L. Chopra, P. D. Paulson and V. Dutta. *Thin-film solar cells: an overview.* Prog. Photovoltaics Res. Appl. **12**, 69–92, (2004).

[10] URL `http://www.pveducation.org/pvcdrom/appendices/solar-cell-efficiency-results2`.

[11] L. C. Olsen, R. C. Bohara and M. W. Urie. *Explanation for low-efficiency Cu_2O schottky-barrier solar cells*. Appl. Phys. Lett. **34**, 47–49, (1979).

[12] J. Herion, E. Niekisch and G. Scharl. *Investigation of metal oxide/cuprous oxide heterojunction solar cells*. Sol. Energy Mater. **4**, 101–112, (1980).

[13] S. S. Jeong, A. Mittiga, E. Salza, A. Masci and S. Passerini. *Electrodeposited ZnO/Cu_2O heterojunction solar cells*. Electrochim. Acta **53**, 2226–2231, (2008).

[14] T. Minami, Y. Nishi, T. Miyata and J. I. Nomoto. *High-efficiency oxide solar cells with ZnO/Cu_2O heterojunction fabricated on thermally oxidized Cu_2O sheets*. Appl. Phys. Express **4**, 062301, (2011).

[15] B. Kramm, A. Laufer, D. Reppin, A. Kronenberger, P. Hering, A. Polity and B. K. Meyer. *The band alignment of Cu_2O/ZnO and Cu_2O/GaN heterostructures*. Appl. Phys. Lett. **100**, 094102, (2012).

[16] Y. Ievskaya, R. L. Z. Hoye, A. Sadhanala, K. P. Musselman and J. L. MacManus-Driscoll. *Fabrication of ZnO/Cu_2O heterojunctions in atmospheric conditions: Improved interface quality and solar cell performance*. Sol. Energy Mater. Sol. Cells **135**, 43–48, (2015).

[17] T. Tohyama and S. Maekawa. *Physical parameters in copper oxide superconductors*. Journal of the Physical Society of Japan **59**, 1760-1770, (1990).

[18] A. Önsten, M. Göthelid and U. O. Karlsson. *Atomic structure of $Cu_2O(111)$*. Surf. Sci. **603**, 257–264, (2009).

[19] D. Tahir and S. Tougaard. *Electronic and optical properties of Cu, CuO and Cu_2O studied by electron spectroscopy*. J. Phys. Condens. Matter **24**, 175002, (2012).

[20] S. Poulston, P. M. Parlett, P. Stone and M. Bowker. *Surface oxidation and reduction of cuo and Cu_2O studied with XPS and XAES*. Surf. Interface Anal. **24**, 811–820, (1996).

[21] S. B. Ogale, P. G. Bilurkar, N. Mate, S. M. Kanetkar, N. Parikh and B. Patnaik. *Deposition of copper oxide thin films on different substrates by pulsed excimer laser ablation deposition of copper oxide thin films on different excimer laser ablation substrates by puked*. J. Appl. Phys. **72**, 3765–3769, (1992).

[22] K. Ozawa, Y. Oba and K. Edamoto. *Formation and characterization of the Cu_2O overlayer on zn-terminated $ZnO(0001)$*. Surf. Sci. **603**, 2163–2170, (2009).

[23] A. von Richthofen, R. Domnick and R. Cremer. *Preparation of cuprite (Cu_2O), paramelaconite ($Cu_3^{2+}Cu_2^{1+}O_4$) and tenorite (CuO) with magnetron sputtering ion plating characterization by EPMA , XRD , HEED and SEM.* Fresenius J. Anal. Chem. **358**, 312–315, (1997).

[24] T. Ito, H. Yamaguchi, K. Okabe and T. Masumi. *Single-crystal growth and characterization of Cu_2O and CuO.* J. Mater. Sci. **33**, 3555–3566, (1998).

[25] J. P. Hu, D. J. Payne, R. G. Egdell and J. Guo. *On-site interband excitations in resonant inelastic x-ray scattering from Cu_2O.* Phys. Rev. B **77**, 155115, (2008).

[26] F. Jensen, F. Besenbacher and I. Stensgaard. *Two new oxygen induced reconstructions on Cu(111).* Surf. Sci. **270**, 400–404, (1992).

[27] T. Matsumoto, R. A. Bennett, P. Stone, T. Yamada, K. Domen and M. Bowker. *Scanning tunneling microscopy studies of oxygen adsorption on Cu(111).* Surf. Sci. **471**, 225–245, (2001).

[28] A. Önsten, J. Weissenrieder, D. Stoltz, S. Yu, M. Göthelid and U. O. Karlsson. *Role of defects in surface chemistry on $Cu_2O(111)$.* J. Phys. Chem. C **117**, 19357–19364, (2013).

[29] D. M. Chapin, C. S. Fuller and G. L. Pearson. *A new silicon p-n junction photocell for converting solar radiation into electrical power.* J. Appl. Phys. **25**, 676-677, (1954).

[30] W. E. Spear and P. G. Le Comber. *Substitutional doping of amorphous silicon.* Solid State Commun. **17**, 1193–1196, (1975).

[31] W. R. Birkmire. *Compound polycrystalline solar cells: Recent progress and Y2K perspective.* Sol. Energy Mater. Sol. Cells **65**, 17–28, (2001).

[32] K. Ramanathan, M. A. Contreras, C. L. Perkins, S. Asher, F. S. Hasoon, J. Keane, D. Young, M. Romero, W. Metzger and R. Noufi. *Properties of 19.2% efficiency ZnO/CdS/$CuInGaSe_2$ thin-film solar cells.* Progress in Photovoltaics: Research and Applications **11**, 225-230, (2003).

[33] K. Chopra. *Thin film phenomena.* McGraw-Hill, (1969).

[34] S. E. Shaheen, C. J. Brabec, N. S. Sariciftci, F. Padinger, T. Fromherz and J. Hummelen. *2.5% efficient organic plastic solar cells.* Appl. Phys. Lett. **78**, 841–843, (2001).

[35] C. J. Brabec, N. S. Sariciftci and J. C. Hummelen. *Plastic solar cells.* Adv. Funct. Mater. **11**, 15–26, (2001).

[36] D. Bartesaghi, I. d. C. Pérez, J. Kniepert, S. Roland, M. Turbiez, D. Neher and L. J. A. Koster. *Competition between recombination and extraction of free charges determines the fill factor of organic solar cells.* Nat. Commun. **6**, 7083, (2015).

[37] P. Würfel, *Limitations on energy conversion in solar cells* in *Physics of solar cells* pages 137–153. Wiley-VCH Verlag GmbH, (2007).

[38] URL `https://en.wikipedia.org/wiki/P-n_junction`.

[39] URL `https://en.wikipedia.org/wiki/Metal-semiconductor_junction`.

[40] URL `https://en.wikipedia.org/wiki/Heterojunction`.

[41] W. Tress. *Organic solar cells.* Springer Series in Material Science, (2014).

[42] A. De Vos. *Endoreversible thermodynamics of solar energy conversion.* Oxford University Press on Demand, (1992).

[43] A. De Vos. *Thermodynamics of solar energy conversion.* John Wiley & Sons, (2008).

[44] W. Shockley and H. J. Queisser. *Detailed balance limit of efficiency of p-n junction solar cells.* J. Appl. Phys. **32**, 510–519, (1961).

[45] URL `https://en.wikipedia.org/wiki/Solar_cell_efficiency`.

[46] K. Chopra, S. Major and D. Pandya. *Transparent conductors—a status review.* Thin Solid Films **102**, (1983).

[47] R. G. Gordon. *Criteria for choosing transparent conductors.* MRS Bull. **25**, 52–57, (2000).

[48] D. S. Ginley and C. Bright. *Transparent conducting oxides.* MRS Bull. **25**, 15–18, (2000).

[49] N. Romeo, A. Bosio, V. Canevari, M. Terheggen and L. Vaillant Roca. *Comparison of different conducting oxides as substrates for CdS/CdTe thin film solar cells.* Thin Solid Films **431-432**, 364–368, (2003).

[50] H. S. Jung and N.-G. Park. *Perovskite solar cells: From materials to devices.* Small **11**, 10–25, (2015).

[51] D. L. Staebler and C. R. Wronski. *Reversible conductivity changes in discharge-produced amorphous Si.* Appl. Phys. Lett. **31**, 292–294, (1977).

[52] B. K. Meyer, A. Polity, D. Reppin, M. Becker, P. Hering, P. J. Klar, T. Sander, C. Reindl, J. Benz, M. Eickhoff, C. Heiliger, M. Heinemann, J. Bläsing, A. Krost, S. Shokovets, C. Müller and C. Ronning. *Binary copper oxide semiconductors: From materials towards devices*. Phys. Status Solidi **249**, 1487–1509, (2012).

[53] L. Grondahl, *Locking device*. 1925, patent.

[54] L. Grondahl and P. H. Geiger. *A new electronic rectifier*. American Institute of Electrical Engineers, Transactions of the **46**, 357–366, (1927).

[55] L. O. Grondahl. *The copper-cuprous-oxide rectifier and photoelectric cell*. Rev. Mod. Phys. **5**, 141–168, (1933).

[56] W. H. Brattain. *The copper oxide rectifier*. Rev. Mod. Phys. **23**, 203–212, (1951).

[57] E. Abbe. *Beiträge zur Theorie des Mikroskops und der mikroskopischen Wahrnehmung*. Archiv für Mikroskopische Anatomie **9**, 413–468, (1873).

[58] E. Ruska. *The development of the electron-microscope and of electron-microscopy*. Reviews of Modern Physics **59**, 627–638, (1987).

[59] R. Young, J. Ward and F. Scire. *Topografiner - instrument for measuring surface microtopography*. Review of Scientific Instruments **43**, 999, (1972).

[60] H. M. Benia. *Spatially resolved optical measurements on supported metal particles and oxide surfaces with the STM*. Phd thesis, Humboldt-Universität zu Berlin, (2008).

[61] G. Binnig, H. Rohrer, C. Gerber and E. Weibel. *Tunneling through a controllable vacuum gap*. Applied Physics Letters **40**, 178–180, (1982).

[62] E. Lægsgaard, L. Osterlund, P. Thostrup, P. B. Rasmussen, I. Stensgaard and F. Besenbacher. *A high-pressure scanning tunneling microscope*. Rev. Sci. Instrum. **72**, 3537, (2001).

[63] Z. Zhu, F. Tao, F. Zheng, R. Chang, Y. Li, L. Heinke, Z. Liu, M. Salmeron and G. A. Somorjai. *Formation of nanometer-sized surface platinum oxide clusters on a stepped Pt(557) single crystal surface induced by oxygen: A high-pressure STM and ambient-pressure XPS study*. Nano Lett. **12**, 1491–1497, (2012).

[64] J.-F. K. Jerratsch. *Investigation and manipulation of thin oxide films supported on metal single crystals*. Phd thesis, Fachbereich Physik der Freien Universität Berlin, (2011).

[65] J. Bardeen. *Tunnelling from a many-particle point of view*. Phys. Rev. Lett. **6**, 57–59, (1961).

[66] J. Tersoff and D. R. Hamann. *Theory and application for the scanning tunneling microscope*. Phys. Rev. Lett. **50**, 1998, (1983).

[67] J. Tersoff and D. R. Hamann. *Theory of the scanning tunneling microscope*. Phys. Rev. B **31**, 805–813, (1985).

[68] A. Selloni, P. Carnevalie, E. Tosatti and C. D. Chen. *Voltage-dependent scanning-tunneling microscopy of a crystal surface: Graphite*. Phys. Rev. B **31**, 2602–2605, (1985).

[69] C. J. Chen. *Introduction to scanning tunneling microscopy*. Oxford University Press, 2nd, (2008).

[70] N. Nilius. *Properties of oxide thin films and their adsorption behavior studied by scanning tunneling microscopy and conductance spectroscopy*. Surf. Sci. Rep. **64**, 595–659, (2009).

[71] S. Schintke, S. Messerli, M. Pivetta, F. Patthey, L. Libioulle, M. Stengel, A. De Vita and W.-D. Schneider. *Insulator at the ultrathin limit: MgO on Ag(001)*. Phys. Rev. Lett. **87**, 276801, (2001).

[72] M. C. Gallagher, M. S. Fyfield, J. P. Cowin and S. A. Joyce. *Imaging insulating oxides: Scanning tunneling microscopy of ultrathin MgO films on Mo(001)*. Surf. Sci. **339**, 5–9, (1995).

[73] G. Doyen, *The scattering theoretical approach to the scanning tunneling microscope* in *Scanning tunneling microsc. III theory STM relat. scanning probe methods* pages 23–50. Springer, Berlin, Heidelberg, (1993).

[74] S. Ulrich. *Design and construction of a low-temperature scanning tunneling microscope for spectroscopic applications on model catalysts*. Phd thesis, Technischen Universität Berlin, (2011).

[75] Y. Cui, C. Stiehler, N. Nilius and H. J. Freund. *Probing the electronic properties and charge state of gold nanoparticles on ultrathin MgO versus thick doped CaO films*. Phys. Rev. B **92**, 075444, (2015).

[76] K. H. Gundlach. *Zur Berechnung des Tunnelstroms durch eine trapezförmige Potentialstufe*. Solid. State. Electron. **9**, 949–957, (1966).

[77] J. H. Coombs and J. K. Gimzewski. *Fine structure in field emission resonances at surfaces*. Journal of Microscopy **152**, 841–851, (1988).

[78] R. S. Becker, J. A. Golovcheno and B. S. Schwartzentruber. *Electron interferometry at crystal surfaces*. Phys. Rev. Lett. **55**, 987–990, (1985).

[79] G. Binnig, K. H. Frank, H. Fuchs, N. Garcia, B. Reihl, H. Rohrer, F. Salvan and a. R. Williams. *Tunneling spectroscopy and inverse photoemission: Image and field states*. Phys. Rev. Lett. **55**, 991–994, (1985).

[80] J. I. Pascual, N. Lorente, Z. Song and H. P. Conrad. *Selectivity in vibrationally mediated single-molecule chemistry*. Nature **423**, 525–528, (2003).

[81] B. C. Stipe, M. A. Rezaei and W. Ho. *Single-molecule vibrational spectroscopy and microscopy*. Science **280**, 1732–1735, (1998).

[82] F. Forstmann. *The concepts of surface states*. Prog. Surf. Sci. **42**, 21–31, (1993).

[83] W. Shockley. *On the surface states associated with a periodic potential*. Phys. Rev. **56**, 317–323, (1939).

[84] URL `https://en.wikipedia.org/wiki/Surface_states`.

[85] I. E. Tamm. Phys. Z. Soviet Union **1**, 732, (1932).

[86] K. Siegbahn and K. Edvarson. *β-ray spectroscopy in the precision range of 1:10^5*. Nucl. Physic **1**, 137–159, (1956).

[87] J. C. Carver, G. K. Schweitzer and T. A. Carlson. *Use of x-ray photoelectron spectroscopy to study bonding in Cr, Mn, Fe, and Co compounds*. J. Chem. Phys. **57**, 973, (1972).

[88] M.-J. Kim, H.-J. Na, K. C. Lee, E. A. Yoo and M. Lee. *Preparation and characterization of Au-Ag and Au-Cu alloy nanoparticles in chloroform*. J. Mater. Chem. **13**, 1789-1792, (2003).

[89] L. J. Salvatl, L. E. Makovsky, J. M. Stencel, F. R. Brownls and D. M. Hercules. *Surface spectroscopic study of tungsten-alumina catalysts using x-ray photoelectron, ion scattering, and Raman spectroscopies*. J. Phys. Chem. **85**, 3700–3707, (1981).

[90] A. F. Lee, J. N. Naughton, Z. Liu and K. Wilson. *High-pressure XPS of crotyl alcohol selective oxidation over metallic and oxidized Pd(111)*. ACS Catal. **2**, 2235–2241, (2012).

[91] T. L. Alford, L. C. Feldman and J. W. Mayer. *Fundamentals of nanoscale film analysis*. Springer, (2007).

[92] URL `https://en.wikipedia.org/wiki/X-ray_photoelectron_spectroscopy`.

[93] S. Hofmann. *Auger- and x-ray photoelectron spectroscopy in materials science: A user-oriented guide*. Springer Series in Surface Science, (2013).

[94] URL
`http://www.virginia.edu/ep/SurfaceScience/electron_interactions.htm`.

[95] M. T. Greiner, L. Chai, M. G. Helander, W.-M. Tang and Z.-H. Lu. *Metal/metal-oxide interfaces: How metal contacts affect the work function and band structure of MoO_3*. Advanced Functional Materials **23**, 215–226, (2013).

[96] URL `http://srdata.nist.gov/XPS/Default.aspx`.

[97] J. Ghijsen, L. Tjeng, J. Elp, H. Eskes, J. Westerink, G. Sawatzky and M. Czyzyk. *Electronic structure of Cu_2O and CuO*. Physical Review B **38**, 11322–11330, (1988).

[98] S. W. Gaarenstroom and N. Winograd. *Initial and final state effects in the ESCA spectra of cadmium and silver oxides*. J. Chem. Phys. **67**, 3500–3506, (1977).

[99] G. Deroubaix and P. Marcus. *X-ray photoelectron spectroscopy analysis of copper and zinc oxides and sulphides*. Surf. interface Anal. **18**, 39–46, (1992).

[100] G. Liu, T. P. S. Clair and D. W. Goodman. *An XPS study of the interaction of ultrathin Cu films with Pd(111)*. J. Phys. Chem. B **103**, 8578–8582, (1999).

[101] P. S. Bagus, H. Freund, H. Kuhlenbeck and E. S. Ilton. *A new analysis of x-ray adsorption branching ratios: Use of Russell-Saunders coupling*. Chem. Phys. Lett. **455**, 331–334, (2008).

[102] P. S. Bagus, C. J. Nelin, E. S. Ilton, M. Baron, H. Abbott, E. Primorac, H. Kuhlenbeck, S. Shaikhutdinov and H. J. Freund. *The complex core level spectra of CeO_2: An analysis in terms of atomic and charge transfer effects*. Chem. Phys. Lett. **487**, 237–240, (2010).

[103] W. E. Kaden, C. Büchner, L. Lichtenstein, S. Stuckenholz, F. Ringleb, M. Heyde, M. Sterrer, H.-J. Freund, L. Giordano, G. Pacchioni, C. J. Nelin and P. S. Bagus. *Understanding surface core-level shifts using the Auger parameter: A study of Pd atoms adsorbed on ultrathin SiO_2 films*. Phys. Rev. B **89**, 115436, (2014).

[104] R. Gunawardane and C. Arumainayagam, *Chapter 10, auger electron spectroscopy* in *Handbook of applied solid state spectroscopy* pages 451–483. Springer, (2006).

[105] J. H. Scofield. *Hartree-Slater subshell photoionization cross-sections at 1254 and 1487 eV*. J. Electron Spectros. Relat. Phenomena **8**, 129–137, (1976).

[106] M. Repoux. *Comparison of background removal methods for XPS*. Surf. Interface Anal. **18**, 567–570, (1992).

[107] S. Tougaard and P. Simund. *Elastic and inelastic scattering of electrons reflected from solids: Effects on energy spectra.* Physical Review B **25**, 4452–4466, (1982).

[108] S. Tougaard and B. Jorgensen. *Absolute background determination in XPS.* Surf. Interface Anal. **7**, 17–21, (1985).

[109] M. P. Seah. *Background subtraction I. general behaviour of tougaard-style backgrounds in AES and XPS.* Surface Science **420**, 285–294, (1999).

[110] A. L. Tofterup. *Inelastic background substraction formulas and energy spectra in XPS and AES.* Surface Science **227**, 157–166, (1990).

[111] P. Auger. *The Auger effect.* Surface Science **48**, 1–8, (1975).

[112] E. Antonides, E. C. Janse and G. A. Sawatzky. *LMM Auger spectra of Cu, Zn, Ga, and Ge, II. relationship with the L_{23} photoelectron spectra via the $L_2L_3M_{45}$ coster-kronig process.* Phys. Rev. B **15**, 4596–4601, (1977).

[113] D. Coster and R. D. L. Kronig. *New type of Auger effect and its influence on the x-ray spectrum.* Physica **2**, 13–24, (1935).

[114] S. Doniach and M. Sunjic. *Many-electron singularity in x-ray photoemission and x-ray line spectra from metals.* Journal of Physics C: Solid State Physics **3**, 285–291, (1970).

[115] G. Moretti. *Auger parameter and Wagner plot in the characterization of chemical states by x-ray photoelectron spectroscopy: a review.* J. Electron Spectros. Relat. Phenomena **95**, 95–144, (1998).

[116] C. D. Wagner. *Auger lines in x-ray photoelectron spectrometry.* Anal. Chem. **44**, 967–973, (1972).

[117] E. Mazzotta, S. Rella, A. Turco and C. Malitesta. *XPS in development of chemical sensors.* RSC Adv. **5**, 83164–83186, (2015).

[118] L. de Broglie. *Waves and quanta.* Nature **112**, 540-540, (1923).

[119] C. Davisson and L. H. Germer. *Diffraction of electrons by a crystal of nickel.* Phys. Rev. B **30**, 705–741, (1927).

[120] URL `https://en.wikipedia.org/wiki/Low-energy_electron_diffraction`.

[121] C. Kittel. *Einführung in die Festkörperphysik.* Oldenbourg, (2006).

[122] P. P. Ewald. *Introduction to the dynamical theory of x-ray diffraction.* Acta Crystallographica Section A **103**, (1969).

[123] URL `https://en.wikipedia.org/wiki/Ewald's_sphere`.

[124] G. Wulff. Z. Kristall **34**, 449, (1901).

[125] URL `https://de.wikipedia.org/wiki/Wulff-Konstruktion`.

[126] URL `http://what-when-how.com/nanoscience-and-nanotechnology/metal-clusters-on-oxides-nanotechnology/`.

[127] I. Horcas, R. Fernandez, J. M. Gomez-Rodriguez, J. Colchero, J. Gomez-Herrero and A. M. Baro. *WSXM: A software for scanning probe microscopy and a tool for nanotechnology*. Rev. Sci. Instrum. **78**, 013705, (2007).

[128] B. Maack. *Druck- und Temperaturabhängigkeit des Oxidationsverhaltens dünner Kupferfilme: untersucht mit optischer Spektroskopie im Vergleich zu Simulationen*. Master thesis, Fachbereich Physik der Universität Bremen, (2016, to be published).

[129] A. Wells. *Structural inorganic chemistry*. Clarendon Press, Oxford, 3, (1984).

[130] A. Soon, T. Söhnel and H. Idriss. *Plane-wave pseudopotential density functional theory periodic slab calculations of co adsorption on $Cu_2O(111)$ surface*. Surf. Sci. **579**, 131–140, (2005).

[131] P. E. de Jongh, D. Vanmaekelbergh and J. J. Kelly. *Cu_2O: Electrodeposition and characterization*. Chem. Mater. **11**, 3512–3517, (1999).

[132] W.-Y. Yang, W.-G. Kim and S.-W. Rhee. *Radio frequency sputter deposition of single phase cuprous oxide using Cu_2O as a target material and its resistive switching properties*. Thin Solid Films **517**, 967–971, (2008).

[133] Z. G. Yin, H. T. Zhang, D. M. Goodner, M. J. Bedzyk, R. P. H. Chang, Y. Sun and J. B. Ketterson. *Two-dimensional growth of continuous Cu_2O thin films by magnetron sputtering*. Appl. Phys. Lett. **86**, 061901, (2005).

[134] A. S. Reddy, P. S. Reddy, S. Uthanna and G. V. Rao. *Effect of substrate temperature on the physical properties of dc magnetron sputtered Cu_2O films*. Phys. Status Solidi **203**, 844–853, (2006).

[135] K. Kawaguchi, M. Nishiyama and T. Morishita. *Molecular beam epitaxy growth of CuO and Cu_20 films with controlling the oxygen content by the flux ratio of Cu/O^+*. J. Cryst. Growth **143**, 221–226, (1994).

[136] M. Ottosson, J. Lu and J.-O. Carlsson. *Chemical vapour deposition of Cu_2O on $MgO(100)$ from CuI and N_2O: aspects of epitaxy*. J. Cryst. Growth **151**, 305–311, (1995).

[137] I. Pallecchi, E. Bellingeri, C. Bernini, C. Pellegrino, A. Siri and D. Marre. *Epitaxial copper oxide thin films deposited on cubic oxide substrates*. J. Phys. D. Appl. Phys. **41**, 125407, (2008).

[138] F. P. Koffyberg and F. A. Benko. *A photoelectrochemical determination of the position of the conduction and valence band edges of p-type CuO*. J. Appl. Phys. **53**, 1173, (1982).

[139] F. Marabelli, G. B. Parravicini and F. Salghetti-Drioli. *Optical gap of CuO*. Phys. Rev. B **52**, 1433–1436, (1995).

[140] M. M. Islam, B. Diawara, V. Maurice and P. Marcus. *First principles investigation on the stabilization mechanisms of the polar copper terminated Cu_2O(111) surface*. Surf. Sci. **603**, 2087–2095, (2009).

[141] J. P. Dahl and A. C. Switendick. *Energy bands in cuprous oxide*. J. Phys. Chem. Solids **27**, 931–942, (1966).

[142] D. O. Scanlon, B. J. Morgan and G. W. Watson. *Modeling the polaronic nature of p-type defects in Cu_2O : The failure of GGA and GGA + U*. J. Chem. Phys. **131**, 124703, (2009).

[143] R. Laskowski, P. Blaha and K. Schwarz. *Charge distribution and chemical bonding in Cu_2O*. Phys. Rev. B **67**, 075102, (2003).

[144] S. Lany. *Band-structure calculations for the 3d transition metal oxides in GW*. Phys. Rev. B - Condens. Matter Mater. Phys. **87**, 085112, (2013).

[145] M. Heinemann, B. Eifert and C. Heiliger. *Band structure and phase stability of the copper oxides Cu_2O, CuO, and Cu_4O_3*. Phys. Rev. B - Condens. Matter Mater. Phys. **87**, 115111, (2013).

[146] M. Nolan and S. D. Elliott. *The p-type conduction mechanism in Cu_2O: a first principles study.*. Phys. Chem. Chem. Phys. **8**, 5350–5358, (2006).

[147] G. K. Paul, Y. Nawa, H. Sato, T. Sakurai and K. Akimoto. *Defects in Cu_2O studied by deep level transient spectroscopy*. Appl. Phys. Lett. **88**, 141901, (2006).

[148] H. Raebiger, S. Lany and A. Zunger. *Origins of the p-type nature and cation deficiency in Cu_2O and related materials*. Phys. Rev. B **76**, 045209, (2007).

[149] B. Yang, J. Tranquada and G. Shirane. *Neutron scattering studies of the magnetic structure of cupric oxide*. Phys. Rev. B **38**, 174–178, (1988).

[150] D. Wu and Q. Zhang. *LSDA + U study of cupric oxide: Electronic structure and native point defects*. Phys. Rev. B **73**, 235206, (2006).

[151] M. H. Whangbo and H. J. Koo. *Spin dimer analysis of the spin exchange interactions in paramelaconite Cu_4O_3 and its analogue $Ag_2Cu_2O_3$ and the spin ordering of the Cu_2O_3 spin lattice leading to their magnetic phase transitions.* Inorg. Chem **41**, 3570–3577, (2002).

[152] D. O. Scanlon, B. J. Morgan, G. W. Watson and A. Walsh. *Acceptor levels in p-type Cu_2O: Rationalizing theory and experiment.* Phys. Rev. Lett. 096405, (2009).

[153] C. Carel, M. Mouallem-Bahout and J. Gaude. *Re-examination of the non-stoichiometry and defect structure of copper (II) oxide or tenorite, $Cu_{1\pm z}$ or $CuO_{1\pm\epsilon}$ a short review.* Solid State Ionics **117**, 47–55, (1999).

[154] A. F. Wright and J. S. Nelson. *Theory of the copper vacancy in cuprous oxide.* J. Appl. Phys. **92**, 5849–5851, (2002).

[155] D. O. Scanlon and G. W. Watson. *Undoped n-type Cu_2O: Fact or fiction?.* J. Phys. Chem. Lett. **1**, 2582–2585, (2010).

[156] O. Porat and I. Riess. *Defect chemistry of Cu_2O at elevated temperatures. part I: Non-stoichiometry, phase width and dominant point defects.* Solid State Ionics **74**, 229–238, (1994).

[157] K. H. Schulz and D. F. Cox. *Propene adsorption on Cu_2O single-crystal surfaces.* Surf. Sci. **262**, 318–334, (1992).

[158] J. Deuermeier, J. Gassmann, J. Broetz and A. Klein. *Reactive magnetron sputtering of Cu_2O: Dependence on oxygen pressure and interface formation with indium tin oxide.* J. Appl. Phys. **109**, 113704, (2011).

[159] R. D. Schmidt-Whitley, M. Martinez-Clemente and A. Revcolevschi. *Growth and microstructural control of single crystal cuprous oxide Cu_2O.* J. Cryst. Growth **23**, 113–120, (1974).

[160] H. Fedderwitz, B. Groß, H. Sträter and N. Nilius. *Reactive copper deposition on Au(111) and Mo(001): Role of the support in the oxidation process.* J. Phys. Chem. C **120**, 7591–7596, (2016).

[161] J. P. Tobin, W. Hirschwald and J. Cunningham. *XPS and XAES studies of transient enhancement of Cu1 at CuO surfaces during vacuum outgassing.* Appl. Surf. Sci. **16**, 441–452, (1983).

[162] C. D. Wagner and G. E. Muilenberg. *Handbook of x-ray photoelectron spectroscopy: a reference book of standard data for use in x-ray photoelectron spectroscopy.* Physical Electronics Division, Perkin-Elmer Corp., (1979).

[163] J. Goniakowski, *1ML $Cu_2O(111)/Au(111)$ stripes*. May 2016, personal communication.

[164] W. Chen, V. Madhavan, T. Jamneala and M. F. Crommie. *Scanning tunneling microscopy observation of an electronic superlattice at the surface of clean gold*. Phys. Rev. Lett. **80**, 1469–1472, (1998).

[165] F. Hanke and J. Björk. *Structure and local reactivity of the Au(111) surface reconstruction*. Phys. Rev. B **87**, 235422, (2013).

[166] K. Schouteden, P. Lievens and C. Van Haesendonck. *Fourier-transform scanning tunneling microscopy investigation of the energy versus wave vector dispersion of electrons at the Au(111) surface*. Phys. Rev. B - Condens. Matter Mater. Phys. **79**, 195409, (2009).

[167] Z.-X. Xie, Z.-F. Huang and X. Xu. *Influence of reconstruction on the structure of self-assembled normal-alkane monolayers on Au(111) surfaces*. Phys. Chem. Chem. Phys. **4**, 1486–1489, (2002).

[168] H. Sträter, H. Fedderwitz, B. Groß and N. Nilius. *Growth and surface properties of cuprous oxide films on Au(111)*. J. Phys. Chem. C **119**, 5975–5981, (2015).

[169] K. H. Schulz and D. F. Cox. *Photoemission and low-energy-electron-diffraction study of clean and oxygen-dosed $Cu_2O(111)$ and (100) surfaces*. Physical Review B **43**, (1991).

[170] C. Li, F. Wang, S. F. Li, Q. Sun and Y. Jia. *Stability and electronic properties of the o-terminated $Cu_2O(111)$ surfaces: First-principles investigation*. Phys. Lett. Sect. A Gen. At. Solid State Phys. **374**, 2994–2998, (2010).

[171] L. I. Bendavid and E. A. Carter. *First-principles predictions of the structure, stability, and photocatalytic potential of Cu_2O surfaces*. The Journal of Physical Chemistry B **117**, 15750-15760, (2013).

[172] G. Kresse and J. Hafner. *Ab initio molecular-dynamics simulation of the liquid-metal amorphous-semiconductor transition in germanium*. Phys. Rev. B **49**, 14251–14269, (1994).

[173] J. P. Perdew, J. A. Chevary and S. H. Vosko. *Atoms, molecules, solids and surfaces: Applications of generalized gradient approximation for exchange and correlation*. Phys. Rev. B **46**, 6671, (1992).

[174] J. Heyd, G. E. Scuseria and M. Ernzerhof. *Hybrid functionals based on a screened coulomb potential*. J. Chem. Phys. **118**, 8207–8215, (2003).

[175] G. Kresse and D. Joubert. *From ultrasoft pseudopotentials to the projector augmented-wave method*. Phys. Rev. B **59**, 1758–1775, (1999).

[176] J. D. Pack and H. J. Monkhorst. *Special points for Brillouin-zone integrations*. Phys. Rev. B **13**, 5188, (1976).

[177] T. Lee, Y. Lee, K. Kang and A. Soon. *In search of non-conventional surface oxidic motifs of Cu on Au(111)*. Phys. Chem. Chem. Phys. **18**, 7349–7358, (2016).

[178] L. Y. Isseroff and E. A. Carter. *Importance of reference hamiltonians containing exact exchange for accurate one-shot GW calculations of Cu_2O*. Phys. Rev. B - Condens. Matter Mater. Phys. **85**, 235142, (2012).

[179] N. Nilius, H. Fedderwitz, B. Groß, C. Noguera and J. Goniakowski. *Incorrect DFT-GGA predictions of the stability of non-stoichiometric/polar dielectric surfaces: the case of $Cu_2O(111)$*. Phys. Chem. Chem. Phys. **18**, 6729–6733, (2016).

[180] P. W. Tasker. *The stability of ionic crystal surfaces*. J. Phys. C Solid State Phys. **12**, 4977–4984, (1979).

[181] J. Goniakowski, F. Finocchi and C. Noguera. *Polarity of oxide surfaces and nanostructures*. Reports Prog. Phys. **71**, (2008).

[182] S. Prada, L. Giordano, G. Pacchioni, C. Noguera and J. Goniakowski. *Properties of Pt-supported iron oxide ultra-thin films: Similarity of hubbard-corrected and hybrid density functional theory description*. J. Chem. Phys. **141**, 144702, (2014).

[183] M. Schmid, M. Shishkin, G. Kresse, E. Napetschnig, P. Varga, M. Kulawik, N. Nilius, H.-P. Rust and H.-J. Freund. *Oxygen-deficient line defects in an ultrathin aluminum oxide film*. Phys. Rev. Lett. **97**, 046101, (2006).

[184] S. Surnev, M. G. Ramsey and F. P. Netzer. *Vanadium oxide surface studies*. Progress in Surface Science **73**, 117 - 165, (2003).

[185] Y. Pan, S. Benedetti, N. Nilius and H.-J. Freund. *Change of the surface electronic structure of Au(111) by a monolayer MgO(001) film*. Phys. Rev. B **84**, 075456, (2011).

[186] G. Hörmandinger. *Imaging of the Cu(111) surface state on scanning tunneling microscopy*. Physical Review B **49**, 897–906, (1994).

[187] P. L. Hansen, J. B. Wagner, S. Helveg, J. R. Rostrup-Nielsen, B. S. Clausen and H. Topsøe. *Atom-resolved imaging of dynamic shape changes in supported copper nanocrystals*. Science **295**, 2053-2055, (2002).

[188] L. V. Koplitz, O. Dulub and U. Diebold. *STM study of copper growth on ZnO(0001)-Zn and ZnO(0001)-O surfaces.* J. Phys. Chem. B **107**, 10583–10590, (2003).

[189] X. Duan, O. Warschkow, a. Soon, B. Delley and C. Stampfl. *Density functional study of oxygen on Cu(100) and Cu(110) surfaces.* Phys. Rev. B - Condens. Matter Mater. Phys. **81**, 1–15, (2010).

[190] A. K. Santra, B. K. Min and D. W. Goodman. *Oxygen-induced p(1×3)-O reconstruction on Mo(112): a precursor to the epitaxial formation of MoO_2(100).* Surf. Sci. **513**, L441–L444, (2002).

[191] T. Schroeder, J. Zegenhagen, N. Magg, B. Immaraporn and H. J. Freund. *Formation of a faceted MoO_2 epilayer on Mo(112) studied by XPS, UPS and STM.* Surf. Sci. **552**, 85–97, (2004).

[192] I. Valenti, S. Benedetti, A. Bona and S. Valeri. *ZnO nanostructure formation on the Mo(001) surface.* J. Phys. Chem. C **119**, 13743–13749, (2015).

[193] D. Lide. *CRC handbook of chemistry and physics.* CRC Press, Boca Raton, FL, (2010).

[194] J. A. Rodríguez, P. Liu, J. Hrbek, M. Pérez and J. Evans. *Water-gas shift activity of Au and Cu nanoparticles supported on molybdenum oxides.* J. Mol. Catal. A Chem. **281**, 59–65, (2008).

[195] J. M. Gottfried, K. J. Schmidt, S. L. M. Schroeder and K. Christmann. *Spontaneous and electron-induced adsorption of oxygen on Au(110)-(1×2).* Surf. Sci. **511**, 65–82, (2002).

[196] E. Bauer. *Phänomenologische Theorie der Kristallabscheidung an Oberflächen I.* Zeitschrift für Krist. **110**, 372–394, (1958).

[197] H. L. Skriver and N. M. Rosengaard. *Surface-energy and work function of elemental metals.* Phys. Rev. B **46**, 7157–7168, (1992).

[198] L. Vitos, A. V. Ruban, H. Skriver and J. Kollár. *The surface energy of metals.* Surf. Sci. **411**, 186–202, (1998).

[199] A. Papakondylis and P. Sautet. *Ab initio study of the structure of the α-/MoO_3-solid and study of the absorption of H_2O and CO molecules on its (100) surfaces.* J. Phys. Chem. **100**, 10681–10683, (1996).

[200] S. Guimond, D. Göbke, J. M. Sturm, Y. Romanyshyn, H. Kuhlenbeck, M. Cavalleri and H. J. Freund. *Well-ordered molybdenum oxide layers on Au(111): Preparation and properties.* J. Phys. Chem. C **117**, 8746–8757, (2013).

[201] S. Stankic, R. Cortes-Huerto, N. Crivat, D. Demaille, J. Goniakowski and J. Jupille. *Equilibrium shapes of supported silver clusters.* Nanoscale **5**, 2448–2453, (2013).

[202] T. Worren, K. Hojrup Hansen, E. Lægsgaard, F. Besenbacher and I. Stensgaard. *Copper clusters on Al_2O_3/NiAl(110) studied with STM.* Surf. Sci. **477**, 8–16, (2001).

[203] K. Hansen, T. Worren, S. Stempel, E. Lægsgaard, M. Bäumer, H.-J. Freund, F. Besenbacher and I. Stensgaard. *Palladium nanocrystals on Al_2O_3: Structure and adhesion energy.* Phys. Rev. Lett. **83**, 4120–4123, (1999).

[204] C. Revenant, G. Renaud, R. Lazzari and J. Jupille. *Defect-pinned nucleation, growth, and dynamic coalescence of Ag islands on MgO(001): An in situ grazing-incidence small-angle x-ray scattering study.* Phys. Rev. B - Condens. Matter Mater. Phys. **79**, 235424, (2009).

[205] R. Lazzari, G. Renaud, C. Revenant, J. Jupille and Y. Borensztein. *Adhesion of growing nanoparticles at a glance: Surface differential reflectivity spectroscopy and grazing incidence small angle x-ray scattering.* Phys. Rev. B **79**, 125428, (2009).

[206] H. Graoui, S. Giorgio and C. Henry. *Shape variations of Pd particles under oxygen adsorption.* Surf. Sci. **417**, 350–360, (1998).

Acknowledgements

I would like to thank everybody who contributed to the success of this thesis.

- An erster Stelle natürlich Prof. Dr. Niklas Nilius, der das Thema dieser Arbeit ermöglicht, sowie die nötigen Mittel in der Arbeitsgruppe Rastersondenspektroskopie zur Verfügung gestellt und mit seiner Anleitung jede Phase dieser Arbeit betreut hat.
- Prof. Dr. Achim Kittel für hilfreiche Diskussionen und seinen Einsatz als Zweitgutachter.
- Prof. Dr. Alexander Hartmann für die Bereitschaft, Mitglied der Prüfungskommission zu sein.
- To our collaborators Prof. Dr. Claudine Noguera and Prof. Dr. Jacek Goniakowski from CNRS-Sorbonne Université, Paris for their theoretical work on the structural models.
- Den Mitarbeitern der mechanischen Werkstätten der Universität Oldenburg für die Anfertigung des Probenhalters für die neue Hochdruckzelle.
- Meinen Mit-Doktoranden sowie allen ehemaligen und neuen Mitgliedern der AG Raspe: Hendrik Sträter, Boris Groß, Thomas Meyer, René Jakob, Christoph Möller, Björn Maack und Maike Luft für das gute Büro- und Laborklima.
- René Jakob, der den Stress auch am Wochenende miterleben durfte.
- Friedrich Hinrichs und Malin Ulrich für guten Rat, wenn dieser teuer ist.
- Meiner Mutter Ina und meiner Schwester Frauke für die nötige Rückendeckung in allen Lebenslagen.

Einen besonderen Dank meinem Vater Walter Fedderwitz (⋆1952 - †2014), der mein Interesse an Wissenschaft und Technik immer gefördert hat.

Curriculum Vitae

- 09/2013 - 11/2016
  PhD Thesis **Preparation and Characterization of Cuprous Oxide Thin Films using Low-Temperature Scanning Tunneling Microscopy** in the group *Scanning Probe Spectroscopy* of Prof. Dr. Niklas Nilius, University of Oldenburg

- 02/2013 - 09/2013
  PhD student at the FHI Berlin in the group of Prof. Dr. Nilius

- 07/2011 - 07/2012
  Diploma Thesis **Construction and Setup of a STM-Scanner for the use in a Low-Temperature Microscope** in the group *Experimental Physics of Complex Systems* of apl. Prof. Dr. Achim Kittel, University of Oldenburg

- 2003 - 2012
  Student at the Carl von Ossietzky University of Oldenburg

- 1996 - 2003
  Cato Bontjes van Beek Gymnasium, Achim

Erklärung gemäß Promotionsordnung

Hiermit erkläre ich, dass ich die vorliegende Dissertation selbstständig verfasst und nur die angegebenen Hilfsmittel verwendet habe.
Die Dissertation hat weder in Teilen noch in ihrer Gesamtheit einer anderen wissenschaftlichen Hochschule zur Begutachtung in einem Promotionsverfahren vorgelegen. Teile der Dissertation wurden in [160, 168, 179] veröffentlicht.
Die Leitlinien guter wissenschaftlicher Praxis an der Carl von Ossietzky Universität Oldenburg sind befolgt worden. In Zusammenhang mit dem Promotionsvorhaben wurden keine kommerziellen Vermittlungs- oder Beratungsdienste (Promotionsberatung) in Anspruch genommen.

Datum

Unterschrift